Ion transport in ionomeric polymers for ionic electroactive polymer devices

by

Wangyujue Hong

A dissertation submitted to the graduate faculty

in partial fulfillment of the requirements for the degree of

DOCTOR OF PHILOSOPHY

Major: Mechanical Engineering

Program of Study Committee:

Reza Montazami, Major Professor

Liang Dong

Nastaran Hashemi

Judy Vance

Xinwei Wang

Chenxu Yu

Iowa State University

Ames, Iowa

2016

TABLE OF CONTENTS

LIST OF TABLES vi

LIST OF FIGURES vii

ACKNOWLEDGEMENTS xiii

ABSTRACT xiv

CHAPTER 1. GENERAL INTRODUCTION 1

1.1 Introduction to IEAP Actuators and Sensors 1

1.2 Dissertation Organization 2

1.3 Literature Review 3

1.3.1 Origin and development 3

1.3.2 Ionomeric membrane 6

1.3.3 Ionic liquid 8

1.3.4 Conductive network composite 9

1.3.5 Electrode 15

CHAPTER 2. ELECTROCHEMICAL AND MORPHOLOGICAL STUDIES OF IONIC POLYMER METAL COMPOSITES AS STRESS SENSORS 16

Abstract 16

2.1 Introduction 16

2.2 Experimental Section 18

2.2.1 Materials 18

2.2.2 Methods 19

2.3 Results and Discussion . . . 21
2.3.1 Morphological characterization . . . 21
2.3.2 Electrochemical analysis . . . 23
2.3.3 Mechanoelectrical sensing performance . . . 26
2.4 Conclusions . . . 28
Acknowledgment . . . 28

CHAPTER 3. INFLUENCE OF IONIC LIQUID CONCENTRATION ON THE ELECTROMECHANICAL PERFORMANCE OF IONIC ELECTROACTIVE POLYMER ACTUATORS . . . 29

Abstract . . . 29
3.1 Introduction . . . 29
3.2 Materials and Methods . . . 31
3.2.1 Sample preparation . . . 31
3.2.2 Electrochemical characterization . . . 31
3.2.3 Electromechanical characterization . . . 32
3.3 Results and Discussions . . . 32
3.3.1 Current flow . . . 32
3.3.2 Electromechanical response . . . 32
3.3.3 Electrochemical studies . . . 34
3.3.4 Discussion . . . 39
3.4 Conclusion . . . 40
Acknowledgment . . . 40

CHAPTER 4. EVIDENCE OF COUNTERION MIGRATION IN IONIC POLYMER ACTUATORS VIA INVESTIGATION OF ELECTROMECHANICAL PERFORMANCE . . . 41

Abstract . . . 41
4.1 Introduction . . . 41

4.2 Experimental . . . 43
4.2.1 Materials . . . 43
4.2.2 Methods . . . 44
4.3 Results and Discussion . . . 47
4.3.1 Van der Waals radius of counterions . . . 47
4.3.2 Electromechanical response as a function of dopant . . . 48
4.3.3 Discussion . . . 50
4.4 Conclusion . . . 53
Acknowledgements . . . 53
CHAPTER 5. SOFT IONIC ELECTROACTIVE ACTUATORS WITH TUNABLE NON-LINAR LIMB-LIKE DEFORMATION . . . 55
Abstract . . . 55
5.1 Introduction . . . 55
5.2 Experimental . . . 58
5.2.1 Materials . . . 58
5.2.2 Sample fabrication . . . 58
5.2.3 Sample nomenclature . . . 59
5.2.4 Electrochemical characterizations . . . 59
5.2.5 Electromechanical Characterizations . . . 60
5.2.6 Morphological and mechanical characterizations . . . 60
5.2.7 Finite element modeling . . . 61
5.3 Results . . . 61
5.3.1 Equivalent circuit modeling . . . 61
5.3.2 Charging and discharging . . . 65
5.3.3 Electromechanical response . . . 66
5.4 Discussion and Simulation . . . 68
5.4.1 Discussion . . . 68
5.4.2 Finite element simulation . . . 69
5.5 Conclusion . . . 71

CHAPTER 6. NONLINEAR DYNAMIC MODELING OF IONIC POLYMER CONDUCTIVE NETWORK COMPOSITE ACTUATORS USING RIGID FINITE ELEMENT METHOD 72

Abstract 72

6.1 Introduction 72

6.2 Ionic Polymer Conductive Network Composite (IPCNC) Actuators 76

6.2.1 Synthesis of the actuator 77

6.3 Electromechanical Modeling 77

6.3.1 Electrical modeling 77

6.3.2 Electrical parameter identification 81

6.3.3 Validation of electrical model 82

6.3.4 Mechanical modeling 85

6.4 Comparison of Simulation and Experimental Results 91

6.4.1 Mechanical parameter identification 92

6.4.2 Model sensitivity analysis 94

6.4.3 Validation of the RFE model 95

6.5 Discussions 96

6.6 Conclusion 97

CHAPTER 7. GENERAL CONCLUSIONS 100

7.1 Contribution of CNC Nanocomposites on IEAP Sensor 100

7.2 Contribution of CNC Patterns on IEAP Actuator 101

7.3 Contribution of IL Concentration on IEAP Actuator 102

7.4 Contribution of Ionomeric Membrane on IEAP Actuator 102

7.5 Nonlinear Dynamic Modeling of IEAP Actuator 103

7.6 Future Studies 103

APPENDIX A. PROCEDURES OF FINITE ELEMENT MODELING 105

BIBLIOGRAPHY 110

LIST OF TABLES

Table 2.1 Solution resistance, ionic conductivity and electric double layer capacitance of IPMC sensors with various thicknesses of CNC layers. 25

Table 3.1 Solution resistance and ionic conductivity of IPMCs containing different concentrations of ionic liquid. 36

Table 4.1 Van der Waals properties of the counterions of Nafion membrane and anions and cations of ionic liquid dopants. 47

Table 5.1 The abbreviation and its definition of each sample used in this work. . 60

Table 5.2 Fitting parameters for different specimens. 64

Table 6.1 Values of physical parameters for electrical admittance model. 82

Table 6.2 Poles of the electrical admittance based on number of terms. 82

Table 6.3 Comparison of ISE for lumped and distributed electrical models. . . . 83

Table 6.4 Convergence of the RFM to linear EulerBernoulli beam model. 93

Table 6.5 Values of physical parameters for mechanical model. 94

Table A.1 The thickness of each layer in IEAP actuator and its physical properties. 106

LIST OF FIGURES

Figure 1.1 Schematic representation of an IEAP actuator/sensor (Not to scale)[1]. 6

Figure 1.2 Chemical composition of Nafion. 6

Figure 1.3 Schematic cluster-network morphology of Nafion proposed by Gierke *et al.* 7

Figure 1.4 Schematic representation of ionic polymer metal composite prepared by impregnation-reduction method proposed by Millet *et al.*[2]. 10

Figure 1.5 Schematic representation of the four steps of direct assembly process for building dry transducers developed by Akle and Bennett *et al.*[3]. . . . 11

Figure 1.6 Schematic representation of the four steps of direct assembly process for building solvated transducers developed by Akle and Bennett *et al.*[3]. 12

Figure 1.7 Schematic representation of the film deposition process using a slide and beakers. Beakers with cationic and anionic species represent the adsorption process; beakers with water represent washing step. The order of cationic and anionic species depends on the original surface charge of the slide. This schematic assumes the slide has negative surface charge at the very beginning. 13

Figure 1.8 Schematic of formation of two bilayers through adsorption[1]. 14

Figure 2.1 (a) Schematic representation of layer-by-layer direct self assembly of AuNP and PAH; (b) CNC layer formed on Nafion ionomer, the membrane is mounted on a glass frame; (c) foreground: schematic representation of IPMC and sensor structure, background: SEM micrograph of AuNP/PAH CNC nanostructure. 18

Figure 2.2 A schematic representation of the setup and operations for the mechanoelectrical characterization (dimensions are not to scale). The IPMC sensor piece was covered by electrical tape, with copper tape used as electrodes to connect to an oscilloscope to monitor the generated electric signal. A 12 kPa stress was distributed evenly by a mechanical arm whose frequency was controlled at 1 Hz by a step motor. 21

Figure 2.3 (a) UV-Vis absorbance spectra of AuNP aqueous solution (20 ppm); (b) UV-Vis absorbance spectra of 2, 4, 6, 8, and 10-bilayer AuNP/PAH and AuNP/PAH-NaCl nanostructures; (c) plot of the absorbance peaks of CNCs consisting of different number of bilayers and morphology. . . . 22

Figure 2.4 Electrochemical studies of IPMC sensors consisting of different thickness CNCs (without NaCl) (a) Nyquist plot of impedance magnitude of IPMC sensors. Solution resistance values are deduced from the intersection of plots with the axis; (b) Impedance magnitude as a function of frequency; (c) phase angle as a function of frequency; (d) plots of $1/(R_s - R)$ versus ω, and their corresponding fitting lines based on the equivalent circuit (inset). 24

Figure 2.5 Mechanoelectric sensing in repose to cyclic 12 kPa stress at 1 Hz. Insets show the zoomed in plots at the first and last 10 seconds of the experiment. 26

Figure 3.1 Charging and discharging currents for samples containing different ionic liquid concentrations recorded as a function of time under a 4 V square wave. 33

Figure 3.2 Actuation curvatures (primary y-axis) and strain (secondary y-axis) of IEAP actuators in response to a 4 V step potential is presented as a function of EMI-Tf ionic liquid concentration. 34

Figure 3.3 Nyquist plot of impedance magnitude of IEAP actuators containing various concentrations of ionic liquid. Solution resistance is deduced from the intersection of plots with the Z_{re} axis. 35

Figure 3.4 (a) Impedance magnitude versus frequency; and, (b) phase angle versus frequency of IEAP actuator containing different ionic liquid concentration. At higher frequencies, impedance and phase angle exhibit higher dependency on ionic liquid concentration. 36

Figure 3.5 Equivalent electric circuit with Warburg element. 37

Figure 3.6 The plots of $1/(R_S - R)$ versus ω with various ionic liquid contents and their corresponding fitting lines with $y = ax^{1.5} + bx + b^2/(2a)x^{0.5}$. . . . 39

Figure 4.1 Schematics of uncharged and charged doped 3-layer ionic electroactive polymer actuator. Red and blue spheres illustrate cations and anions, respectively. (Not to scale). (For interpretation of the references to color in this figure legend, the reader is referred to the web version of this article.) 43

Figure 4.2 Schematic presentation of ion-exchange process in Nafion. Proton counterions are substitute by other cations. 44

Figure 4.3 Schematic representation of ionic electroactive polymer actuator with geometrical components used in calculation of strain. (Not to scale). . 46

Figure 4.4 Magnitude (arbitrary units) of maximum cationic strain of IEAP actuators consisting of Nafion with different counterions as a function of van der Waals volume of counterions. Actuators consisting of Nafion with larger counterions exhibit enhanced cationic strain. 48

Figure 4.5 Electromechanical responses of IEAP actuators doped with EMI-Tf ionic liquid consisting of Nafion membranes with H^+ and EMI^+ counterions. Cationic strain is enhanced with larger counterion. 50

Figure 4.6 Electromechanical responses of IEAP actuators doped with TES-TFSI ionic liquid consisting of Nafion membranes with H^+ and EMI^+ counterions. The response is shifted toward cationic strain with larger counterion. 51

Figure 4.7 Electromechanical responses of IEAP actuators doped with BMP-TFSI ionic liquid consisting of Nafion membranes with H^+ and EMI^+ counterions. The electromechanical response is completely reversed from fully anionic to fully cationic with larger counterion. 52

Figure 4.8 Schematic cluster-network morphology of Nafion. It is anticipated that counterions (red dots) are mobilized when exposed to an external electric voltage. (For interpretation of the references to color in this figure legend, the reader is referred to the web version of this article.) 53

Figure 5.1 3D schematic representation of the Nafion with three different PEDOT:PSS strip patterns before gold leaf electrodes hot-pressed. From left to right are the samples with one side (1S) (a), two-side symmetric (2SS) (b), and two-side asymmetric (2SA) (c) patterns, respectively. Top line is the isotropic view, and the bottom line is the corresponding side view. The 3D sketches are not to scale. 59

Figure 5.2 SEM image of the crossection of specimen Nafion/1s-PEDOT:PSS/Au, indicating a tight layer adhesion between each layer. 61

Figure 5.3 Equivalent circuit with Warburg element. 62

Figure 5.4 Impedance magnitude of (a) BNafion, (b) Nafion/1s-PEDOT:PSS, (c) Nafion/2s-PEDOT:PSS, and phase of (d) BNafion, (e) Nafion/1s-PEDOT:PSS, (f) Nafion/2s-PEDOT:PSS fitted by equivalent circuit with Warburg element shown in Figure 5.3. 63

Figure 5.5 (a) Charging/discharging currents and (b) charge density versus time for different specimens under a 4 V square wave. Normalized charge versus time at the charging process (c) and discharging process (d) at the interface of the external electrodes for different specimens. 65

Figure 5.6 Sechematic representation and experimental actuation performance for actuator (a)1S, (b)2SS, (c)2SA2, and (d)2SA3. Left side is the cationic response and right side is the anionic response. 67

Figure 5.7 Comparison of experimental bending displacement in response to a 4 V step input voltage (left column) and the results produced by the static theoretical model via ABAQUS (right column). Figure (a) and (b) represent actuator 1S, (c) and (d) represent actuator 2SA2, (e) and (f) represent actuator 2SA3, and (g) and (h) represent actuator 2SS. The top electrode is cathode and the bottom electrode is anode. 70

Figure 6.1 (a) Structure of a goldCNCionomerCNCgold five-layer actuator. (b) Bending mechanism in the IPCNC actuator based on accumulation of ions at oppositely-charged electrodes (not to scale). 76

Figure 6.2 (a) Equivalent lumped electrical circuit model IPCNC actuators. (b) Transmission line model of IPCNC actuators. 78

Figure 6.3 The equivalent single unit circuit for ion diffusion at the electrode/electrolyte interface. 79

Figure 6.4 Convergence of the objective function based on the simulated annealing algorithm. 81

Figure 6.5 Convergence of the transmission line model in frequency domain. . . . 83

Figure 6.6 Convergence of the transmission line model in predicting the actuator current response. 84

Figure 6.7 Convergence of the transmission line model in predicting the actuator current response. 85

Figure 6.8 Comparison of the proposed electrical model with the other models. . . 86

Figure 6.9 Discretization of a three-layer IPCNC actuator into RFEs and SDEs. . 86

Figure 6.10 Distribution of induced electrochemical stress across the thickness of IPCNC actuators. 87

Figure 6.11 Frame assignment for RFEs and SDEs. 88

Figure 6.12 Frame assignment and bending deformation of IPCNC actuator. 91

Figure 6.13 Experimental set-up for measuring the current and bending displacement of IPCNC actuator. 92

Figure 6.14 Convergence of the theoretical model for Y coordinate of the actuator tip. 93

Figure 6.15 Convergence of the theoretical model for X coordinate of the actuator tip. 94

Figure 6.16 Comparison of the results produced by the theoretical model against the experimental bending displacement of the actuator in response to the step input voltage. 95

Figure 6.17 Comparison of the results produced by the theoretical model with the experimental Y coordinate of the actuator tip in response to the step input voltage. 96

Figure 6.18 Comparison of the results produced by the theoretical model with the experimental X coordinate of the actuator tip in response to the step input voltage. 97

Figure 6.19 Comparison of the linear Euler-Bernoulli beam model and the RFE model in prediction of bending displacement of the actuator in response to the step input voltage. 98

Figure 6.20 Comparison of the linear Euler-Bernoulli beam model and the RFE model in prediction of Y coordinate of the actuator tip. 99

Figure A.1 SEM images of specimen Nafion/1s-PEDOT:PSS/Au, from middle point to edge ((a) - (c)) of PEDOT:PSS layer. 105

Figure A.2 Schematic of a bilayer laminate for the characterization of the elastic modulus of individual layer[4]. 105

ACKNOWLEDGEMENTS

My deepest gratitude goes first and foremost to Dr. Reza Montazami, my major professor, for his constant help, support, encouragement and guidance. He has provided sound advice and lots of good ideas on my thesis-writing period and PhD-study period since the time I joined his group in 2011. His astounding knowledge and enthusiastic help make work interesting for me, and I have learned and improved a lot during the past years. Without his consistent and illuminating instruction, this thesis could not have reached its present form. I truly cherish the opportunity to work with him and to be his student.

Secondly, I should give my hearty thanks to Dr. Liang Dong, Dr. Nastaran Hashemi, Dr. Judy Vance, Dr. Xinwei Wang and Dr. Chenxu Yu as my thesis committee members. Their patient instructions and precious suggestions help me a lot for my study and work.

I would also like to thank my labmates, Abdallah Almomani, Yuanfen Chen, Reihaneh Jamshidi, and Kathryn White for the helpful discussions, latest literature sharing and all the fun we had in the lab.

Special thanks go to my friends, colleagues, and faculty and staff in Mechanical Engineering department. Their kindness makes my time at Iowa State University a wonderful experience.

Last my thanks would go to my beloved family. I would thank my parents for their unconditional love for me and great confidence in me all through these years. My husband Chuan Jiang is the person who is always there supporting me no matter what decision I've made. I owe my sincere gratitude to them for what they have done for me.

ABSTRACT

Recently, electroactive polymers (EAPs) have received immense attention and interest from the materials community because of their promising properties such as light weight, high elastic energy density and easy processing, which provide them the applicability in wide areas including solar cells, super capacitors, actuators and sensors. Among wide variety of electroactive polymers, ionic electroactive polymer (IEAP) has been proven more practical for both actuator and sensor applications.

This dissertation discusses the the limiting factors in IEAP actuators and sensors. Three important components, ionomeric polymer membrane, conductive network composites (CNCs) and electrolytes, all have significant determination on the performance of IEAP actuators and sensors. Thorough investigation are conducted by both experimental and theoretical methods, and the findings are presented in this dissertation.

We first investigated how the morphology of CNC thin-film influences the mechanoelectrical performance of IEAP sensors. IEAP sensor, in most cases, is also referred to as ionic polymer-metal composite (IPMC) sensor. A novel approach, layer-by-layer (LbL) ionic self-assembly technique is utilized to fabricate the porous and conductive CNC nanocomposites. The electrochemical, morphological characteristics, and the corresponding mechanoelectrical performance of this IEAP sensor were explored as a function of the CNC morphology.

Meanwhile, the influence of ionic liquids (ILs) concentration on the electromechanical response of IEAP actuators has been investigated. It was observed that an optimum concentration of ions where the electromechanical response is maximized is achieved by adjusting the uptake of IL in the ionomeric membrane; this optimum concentration, however, is not the highest ion concentration.

Functional ionomeric polymer membrane is the backbone of a wide range of ionic devices due to its permeability to ions, which is the principle of these devices. Ions are sourced by

either aqueous electrolytes or ILs. ILs are preferred as their near zero vapor pressure allows longer shelf life, operation in air, and higher operation voltages. We report that in addition to ions sourced by the dopant (e.g. electrolytes or ILs), counterions of the ionomeric membrane contained in the IEAP actuator are also mobilized and contribute to the final electromechanical response.

Many approaches to fabricate CNC thin-film structures have been proposed and enabled an intrinsic way to control the performance of IEAP actuators. We have demonstrated that manipulation of ionic mobility through means of structural design can realize intrinsic limb-like motion in IEAP actuators. By incorporating conjugated polymers in desired patterns as CNC thin-films, we have developed unique IEAP actuators which are capable of exhibiting limb-like angular deformation.

In a collaborative effort, we have also developed a nonlinear dynamic model of IEAP actuators using rigid finite element method.

CHAPTER 1. GENERAL INTRODUCTION

1.1 Introduction to IEAP Actuators and Sensors

In the last two decades, more and more attention has been paid to understand the operation mechanism and improve the performance of electromechanical actuators and mechanoelectric sensors. Interesting applications for such devices are presented and applied in different fields, such as bio-mimetic devices, biomedical devices, microrobotics and microfluidics[5, 6, 7, 8, 9, 10, 11]. In these applications, smart polymers have attracted significant attention due to their low cost, low density, ease of processing and high sensitivity to stimulus[12]. Ionic electroactive polymers, hereafter IEAPs, as a new class of smart structures which exhibit some form of response to an external electric or mechanical stimulus due to the ion penetration through the polymer network, play an important role in the application of electromechanical and mechanoelectrical devices (actuators and sensors).

IEAP actuators are electromechanical devices which exhibit a mechanical deformation when subjected to an external electric voltage. The mechanical deformation is the result of the transport of free ions with different size and their accumulation at the oppositely-charged electrodes, which, will generate a volume imbalance between the two sides of the structure across the thickness[13]. Moreover, it has been proved that the electromechanical phenomenon is reversible by generating an electric signal when the structure responses to any mechanical deformation, which makes it work as an IEAP sensor. The sensing performance relies on, supposedly, random displacement of free ions across the thickness of the structures; these free ions are either provided by aqueous electrolyte or ionic liquids (ILs). The non-zero detectable net electric voltage exists in reality because cations and anions behave differently when subjected to stress[14].

1.2 Dissertation Organization

Chapter 1 provides the background information on actuation and sensing mechanisms in IEAP electromechanical actuators and mechanoelectric sensors, respective. Moreover, a comprehensive review of the existing research and literature is provided to lay a foundation for the research presented in this dissertation.

Chapter 2 reports a fundamental study of IEAP stress sensors, which, in most cases, are also referred to as ionic polymer-metal cmposite (IPMC) sensors. In this work the electrochemical and morphological characteristics of an IPMC sensor were investigated as a function of the nanostructure of its conductive network composites(CNCs).

Chapter 3 is dedicated to our investigation on the influence of IL concentration on the electromechanical performance of IEAP actuators[15].

Chapter 4 presents evidence of couterion migration in ionic polymer actuators via the investigation of their electromechanical performance. Functional ionomeric polymer membranes (Nafion in this study) are the backbone of a wide range of ionic devices. In this chapter, the electromechanical response of IEAP actuators consisting of Nafion ionomeric membranes with different counterions was investigated to understand cationic counterions migration through Nafion membrane[16].

Chapter 5 presents our studies on soft IEAP actuators with tunable limb-like deformation. It was demonstrated that manipulation of ionic motion through means of structural design could be achieved by incorporation of patterns of conjugated polymers. Consequently, intrinsic properties of the IEAP actuators were altered.

Chapter 6 presents development of a non-linear dynamic model of IEAP actuators using rigid finite element method. In this study a proper mathematical model was estimated to effectively predict the actuators' dynamic behavior. This study was conducted in collaboration with Professor Kouzani and his research team at the Deakin University in Australia[17].

Chapter 7 presents the general conclusions and future works.

1.3 Literature Review

1.3.1 Origin and development

To out best recollection, ionic chemomechanical deformation was first reported by Kuhn *et al.*[18]. It was presented that a three-dimensional network system containing polyelectrolytes such as Polyactrylic acid (PAA), if suspended in water, can contract and dilate reversibly when the pH of the medium is changed by alternating addition of small amounts of acid and alkali. They also pointed out that the shape of ionizable polymer molecules depends on the number of charges distributed over the molecular chain. Later in 1965, another system based on Polyvinyl alcohol (PVA) and PAA copolymer was reported by Hamlen *et al.*[19]. This system also exhibited dimensional variations in response to chemical changes in the environment. Since the direction of the current would cause the solution to become either acidic or alkaline, this is the first time to obtain electrically deformation by appling voltage. The very first model of an electrically controlled mechanical deformation was reported by Grodzinsky *et al.* in 1973[20, 21]. They studied and modeled collagen and other polyelectrolyte materials in an electrochemical environment as a set of a electromechanical transduction. A model was developed relating externally measured parameters (potentials and currents, etc.) and membrane intrinsic properties (membrane deformations and fabril diameter, etc.)[21].

More recently interests in this area can be traced to Shahinpoor and his co-workers. In their earlier works (before 1996), Shahinpoor *et al.* focused more on the study of ionic polymeric gels for the robotic applications. As mentioned above, ionic polymeric gels, also known as artificial muscles, are pH sensitive three-dimensional networks of cross-linked macromolecular polymers that can change their initial volume in a liquid medium. As early as 1992, Shahinpoor *et al.* have discussed design, kinematics and swimming dynamics of autonomous swimming robotic structures based on the electrically controlled ionic polymer gels[22]. Subsequently they published a series of experimental studies focused on ionic polymer gels for robotic applications and presented the theoretical models[23, 24, 25, 26].

In 1996 Mojarrad and Shahinpoor firstly gave rise to a new composite of ion exchange membranes (IEM) and platinum as electrically controllable artificial muscles through chemi-

cally treating with platinum salt solution[27]. This work provided a platform for their further studies on IPMC for biomimetic sensors, actuators and artificial muscles. More complete and interesting work can be found in the following references[28, 29, 30]. They also did a series of four review papers focusing on fundamentals, manufacturing techniques, modeling and simulation, and industrial and medical applications of IPMCs[5, 6, 7, 8].

All the work mentioned above are about IEAP actuators doped with aqueous electrolytes. Typical cations are alkali-metal such as Na^+, Ka^+, Li^+ and Cs^+. Nemat-Nasser and Wu *et al.* conducted a comparative experimental study of IEAP actuators with different backbone ionomers (Nafion- and Flemion-based) and in various cations forms[31]. In their work besides the typical alkali-metal cations, alkyl-ammonium cations, tetramethylammonium (TMA^+) and tetrabutylammonium (TBA^+) were also adopted. As reported in their publications, IEAP actuators doped with aqueous electrolytes and alkali-metal as cations undergo electrolysis when subjected to voltages higher than that of electrolysis of water (approximately 1.3 V at room temperature). The electrolysis phenomenon, however, has not occurred for Flemion-based IEAP actuators in TBA^+ form, for up to 3 V. Besides the electrolysis problem, water evaporation in open air is another issue that limits the application of IEAP actuators containing aqueous electrolytes. One approach regarding to this issue was to apply an coating on the actuator surface, which allowed operating the actuator for months[32]. However, this approach increased the stiffness of the actuators and then reduced the strain generated.

Later in 2006, other types of solvents, ethylene glycol, glycerol, and crown ethers were used instead of water in order to overcome these problems by Nemat-Nasser and Zamani *et al.*[33]. IEAP actuators with these heavy and viscous solvents present slower actuation but can withstand relatively higher electric potentials without electrolysis. Other dry forms of IEAP actuators with composites of poly(ethylene oxide), PEO, and poly(ethylene glycol), PEG, have also been studied by Shahinpoor and Kim[34, 35]. They reported that the new constricted actuators overcome many inherent problems other actuators have, for example, wet operating environments for IEAP actuators doped with aqueous electrolytes.

ILs were also investigated as possible new electrolytes for IEAP actuators due to their near zero vapor pressure and large electrochemical stability window by Bennett and Leo[36].

Bennett *et al.* presented that the Nafion-based actuators doped with ILs operated more stably in air. Their work provides a platform for the further studies of IEAP actuators doped with ILs as electrolyte[37, 38, 39, 13, 40, 4, 41, 42]. More in-depth discussion of IL-doped IEAP actuators is presented in section 1.3.3.

Similar studies on IEAP sensors, also known as IPMC sensors, however, are reported later and are relatively rare. To our best recollection, one of the first reports on Nafion-based sensor was published by Sadeghipour *et al.* in 1992 where the concept was introduced[43]. A pressure was applied across the thickness of the sensor and a voltage response was generated. Later in 1995, Shahinpoor *et al.* investigated the response of IPMC sensor against large imposed displacements[44]. More recent experimental and theoretical studies on IPMC sensors were conducted by Bonomo *et al.*[9, 45, 46, 47, 48]. Over the same time period, studies on mathematical modeling of IPMC sensors were also conducted and published[49, 50, 51, 52]. All of the abovementioned studies considered the IPMC sensors doped with aqueous electrolytes; studies on the IL-doped IPMC sensors, however, are rare.

IEAP actuators and sensors studied in this dissertation consist of a thin ionomeric membrane of Nafion as the backbone structure, which is permeable to both cations and anions provided by the dopant. Ionic liquid, typically 1-ethyl-3-methylimidazolium trifluoromethanesulfonate (EMI-Tf), is used to provide the mobilized ions (or ionic complexes). To improve the performance of IEAP actuators and sensors, increasing the capability of the device to store large nunmber of ions and facilitating the ions mobility through the thickness of the device would be a logically effective approach, since the functionality of the device is highly depended on the mobility of ions. Typically, IEAP actuators and sensors also consist of a CNC thin-film on both surfaces of the ionomeric membrane. We have fully explored morphological and structural properties of the CNC nanocomposites and have identified that they both have instrinsic impact on both the sensing (Chapter 2) and actuation (chapter 5) performance of IEAP devices. The last but not the least, a layer of gold leaf is hot pressed on both surfaces of the device to further improve the electrical conductivity and enable uniform charge distribution across the device[1]. Schematic representation of an IEAP actuator/sensor is presented in Figure 1.1.

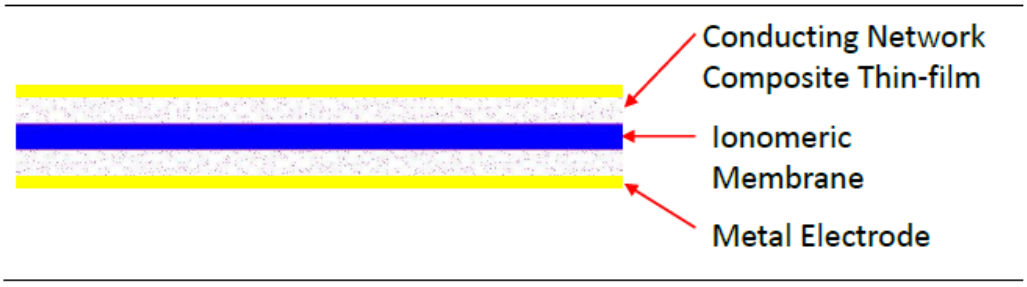

Figure 1.1: Schematic representation of an IEAP actuator/sensor (Not to scale)[1].

1.3.2 Ionomeric membrane

As the backbone of IEAP devices, ionomeric membranes are the core part to promote the ion permeability through the thickness of the system. Nafion, developed at DuPont, is the most common used ion-exchange membrane. The chemical structure of Nafion is shown in Figure 1.2. It mainly consists of a Teflon backbone and ether groups as side chains with sulfonate end group exchange sites. The value of x represents the degree of sulfonation of the polymer, and it determines the equivalent weight (EW) of the membrane, which is defined as the weight of dry polymer per mole of exchange sites. Figure 1.2 shows the form of Nafion after hydrolyzed and the sulfonate exchange sites at the ends of side chains can be linked with proton and some other cations such as Na^+, K^+, Li^+, and alkyl-ammonium cations such as tetramethylammonium (TMA^+) and tetrabutylammonium (TBA^+).

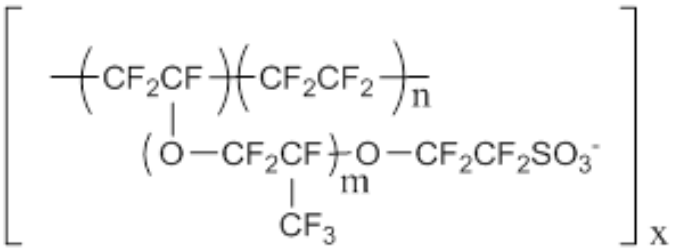

Figure 1.2: Chemical composition of Nafion.

Considering the unique chemical structure of Nafion, some different models have been proposed for the interpretation of its morphology, including (*i*) two-phase model proposed by Cooper *et al.*, and (*ii*) Core-shell model proposed by Macknight *et al.* More details can be

found in the references[53, 54]. Later a so-called cluster network model was first proposed by Gierke *et al.* in 1982, which became the most generally accepted model to describe the specific morphology of Nafion[55]. In this model, the hydrophilic sulfonate exchange sites ($-SO_3^-H^+$) and the attached counter-ions are all reside on the inner surface of ionic cluster phase, while the hydrophobic backbone portion ($-CF_2-CF_2-$) forms the fluorocarbon matrix outside of the cluster phase. The hydrophilic clusters are approximately spherical which are interconnected by short, narrow channels to ensure the mobility of charged ions. The hydrophilic phase separates into approximately spherical domains, and the ionic exchange sites are found inside the spheres near the interface between two phases. A schematic representation of the cluster network model for Nafion perfluorinated membrane is shown in Figure 1.3, where the ionic cluster phase is the pathway to permit water sorption and ion conductivity.

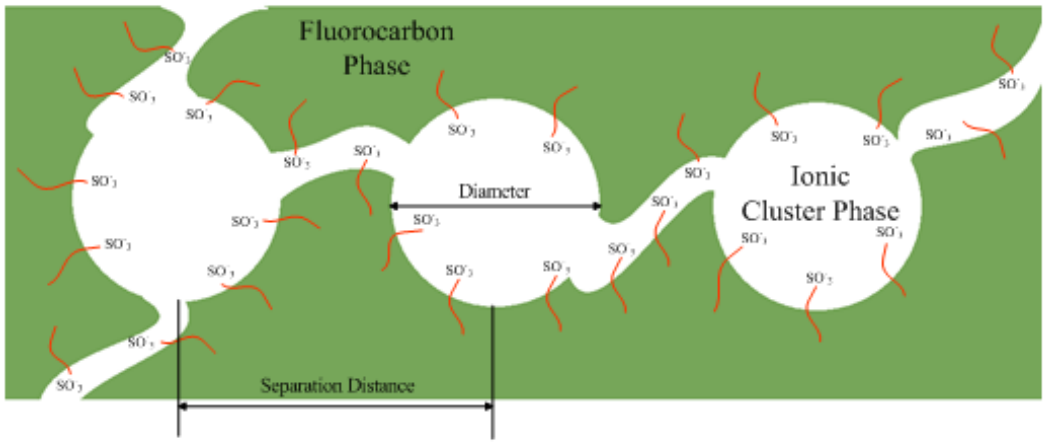

Figure 1.3: Schematic cluster-network morphology of Nafion proposed by Gierke *et al.*

The functionality of IEAP actuators and sensors relies on the mobility of ions through the ionomeric membrane. In fact, ion diffusion/or drift through Nafion is the most essential requirement for operating these ionic devices. Continuous studies have been conducted in the past several years on the ion tranport dynamics of Nafion membranes. For instance, as early as 1993 Morris *et al.* measured the density, dimensional changes and electrical conductivity of Nafion 117 H as a function of water content[56]. Later in 1998, Okada *et al.* reported a large dependence of the Nafion conductivity on the interaction of ions with water and with

microscopic membrane channel structures[57, 58]. Meanwhile, some progress was made on synthesizing new hybrid polymeric membranes by modifying Nafion[59, 60, 61]. The transport properties of the synthesized hybrid membranes were also studied[62].

In one of studies reported in this dissertation, the functionality of Nafion ionomeric membrane was altered by exchanging the proton counterion with larger cations, and the mobility of these exchanged cations has been studied by utilizing the electromechanical response of the IEAP actuators, consisting of Nafion with the corresponding cations. More details of this work are presented in Chapter 4.

1.3.3 Ionic liquid

Technically the sensing and actuation performance of IEAP devices is mainly dependent on the density and mobility of ions, which are provided by the dopant. For IEAP actuators and sensors, electrolyte can be divided into two main categories: aqueous and ILs.

Aqueous electrolytes are acid, base, or salt solutions. IEAP actuators and sensors doped with aqueous electrolytes, however, have inherent limitations including electrolyte evaporation and electrolysis at relatively low voltage.

Therefore, dry solid-state IEAP actuators and sensors doped with ILs have been the subject of extensive and continuous studies. ILs are salts that are in their liquid state at or below room temperature. Common salts tend to be solid at room temperature, since the ionic bound existing in salts is usually stronger than van der Waals force, which is between the molecules of ordinary liquids. Room temperature ILs, on the other hand, usually consist of bulky and asymmetric organic cations and a wide range of anions from organic to inorganic. They tend to be liquid state at or below room temperature due to the inhibition of a crystalline solid formation from their inherent cumbersome structure. ILs are more suited candidates for IEAP devices due to their near-zero vapor pressure and high electrochemical stability.

As early as 2002, Lu *et al.* using ILs for electrochemical devices based on π-conjugated polymers, and reported that ILs have not only enhanced lifetime up to 1 million cycles, but also generated fast cycle switching speeds[63]. ILs as stable electrolytes for IEAP actuators and sensors came from Bennett and Leo firstly in 2004[36]. 1-ethyl-3-methylimidazolium triflu-

oromethanesulfonate (EMI-Tf) was first introduced as a viable electrolyte for Nafion polymer actuators and sensors to eliminate the hydration dependence. Further studies about this subject were conducted in 2006 by the same group[64]. Two ILs, 1-ethyl-3-methylimidazolium trifluoromethanesulfonate (EMI-Tf) which is water miscible, and 1-ethyl-3-methylimidazolium bis(trifluoromethanesulfonyl)imide (EMI-Im), which is hydrophobic, were chosen due to their low viscosity and high conductivity. It was revealed that ILs interact with Nafion membrane in the same way aqueous electrolytes do. The influence of imidazolium-based ILs on the electromechanical performance of IEAP actuators was investigated by Liu *et al.* in 2010[65]. Four imidazolium ILs with two cations and anions of different sizes were used and the corresponding doped actuators were operated under a step voltage.

In one of studies reported in this dissertation, the electromechanical performance of IEAP actuators as a function of IL concentration is reported. More details of this work are presented in Chapter 3.

1.3.4 Conductive network composite

Charge migration across the thickness of the actuator and their accumulation at the ionomer-electrode interface is the actuation mechanism in IEAP actuators[50, 66, 67, 68, 69, 70]. It is becoming clear that the performance of IEAP actuators is strongly dependent on the capacitance of the ionomeric membrane, which is due to the formation of the electric double layer on the ionomer-electrode interface[71]. An enhanced capacitance of the ionomeric membrane enables accumulation of a larger number of ions at the ionomer-electrode interface, which consequently results in larger strain. Bennett and Leo presented some marked advantages over traditional IEAP actuators by adding a layer of conducting polymer film (polypyrrole) on the surface of Nafion[72]. As a result, CNC layers are designed and optimized to act as reservoirs for electrolytes and offer large interfacial area. The mobility of the ions through the CNC layers depends on many attributions of the layers such as the dimensions, conformation, morphology, conductivity, porosity, and of course the interaction of ions with the nano/micro-channels. These physical properties can be tuned by choosing different fabrication techniques in order to ultimately define the characteristics of IEAP devices.

1.3.4.1 Impregnation-reduction process

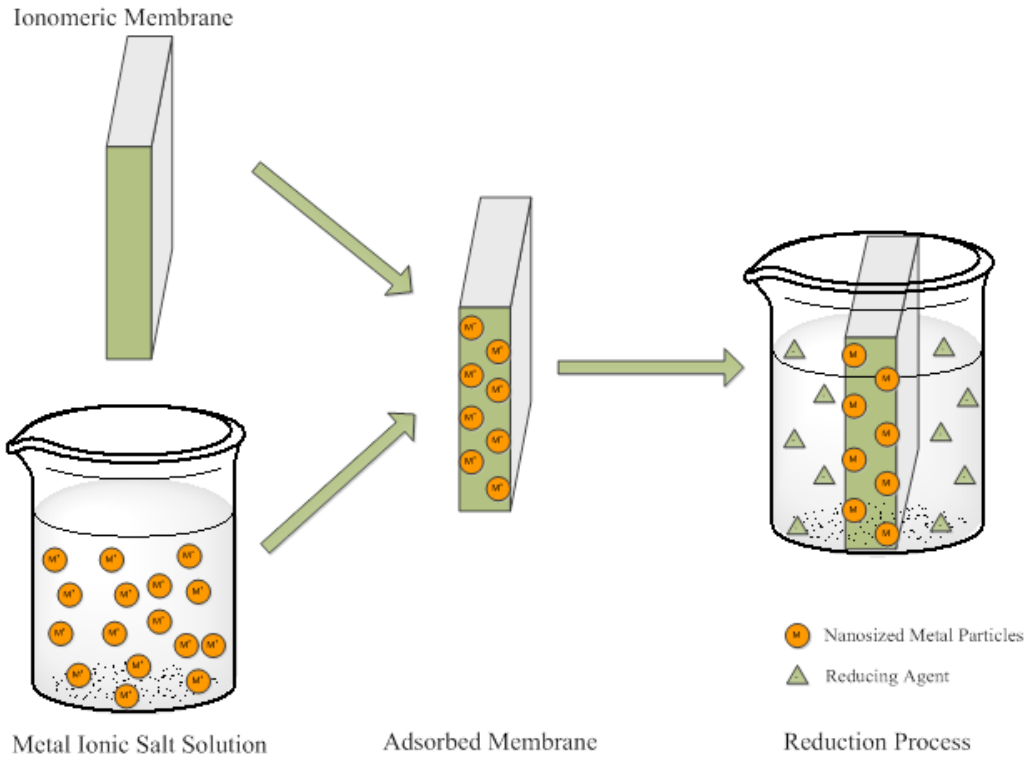

Figure 1.4: Schematic representation of ionic polymer metal composite prepared by impregnation-reduction method proposed by Millet *et al.*[2].

A widely used method at earlier studies is the so-called impregnating-reduction process which was first proposed by Millet *et al.*[2]. In this technique metal cation complex was plated onto Nafion membrane first, then nanosized metal particles were obtained to penetrate into the ionomeric membrane by chemical reduction method. As a result, Nafion membrane was plated with interpenetrating platinum electrodes. Schematic representation of this impregnation-reduction process is represented in Figure 1.4. Millet *et al.* proposed a model for the chemical reduction of platinum tetramine and Nafion film and utilized this model to study the rate of ion-exchange[73] and investigate the precipitation process[74]. Rashid and Shahinpoor also utilized a similar reduction process for the study of ionic polymer platinum composite artificial muscles[75].

The penetrating depth of the platinum electrode into the membrane in this process is up to 20 μm, which effectively enhances the interfacial area between the polymer and the metal.

The enhanced interfacial area is the main reason for the very large capacitance thus a large accumulation of charges at the ionomer-electrode interface.

1.3.4.2 Direct assembly process

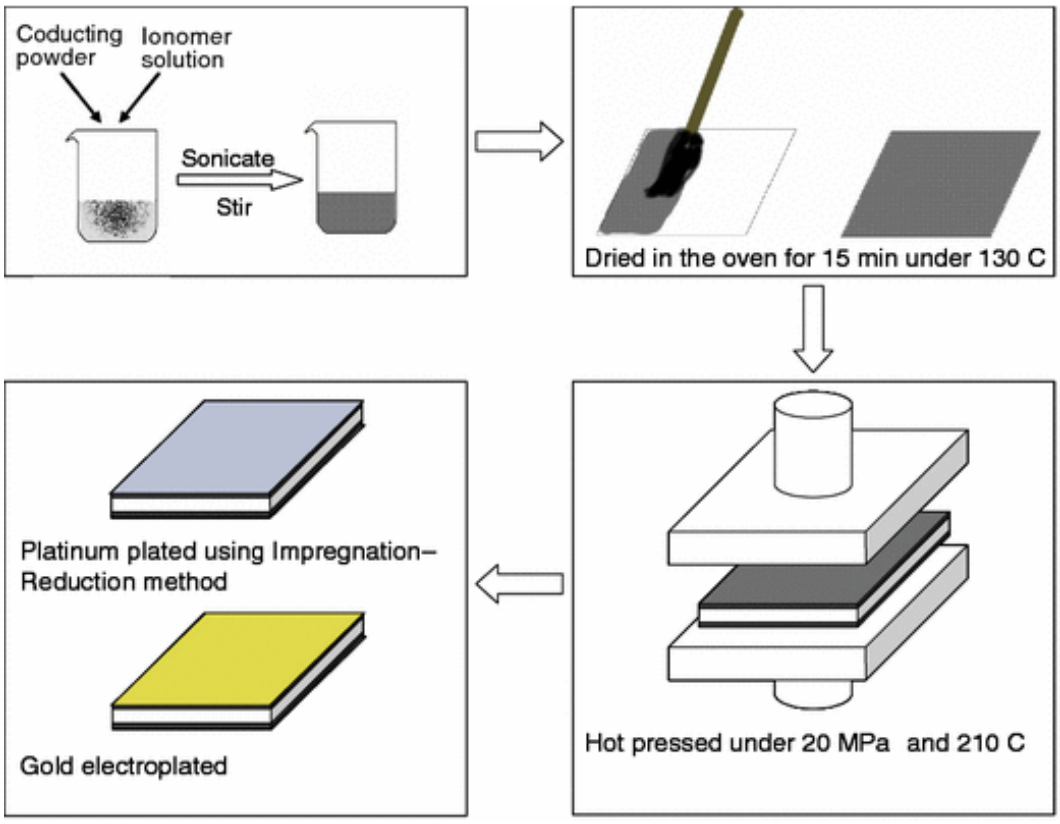

Figure 1.5: Schematic representation of the four steps of direct assembly process for building dry transducers developed by Akle and Bennett *et al.*[3].

Despite advantages of impregnation-reduction technique for fabrication of CNC layers, there are some limiting factors such as lack of control over morphology of the CNCs and limited compatible materials that hinder applicability of this technique. Moreover, it is hard to combine the reduction process with dry-state IEAP actuators and sensors which are doped with non-aqueous electrolytes such as ILs. To eliminate these drawbacks, another direct assembly process was developed by Akle and Bennett *et al.* in 2006-2007[12, 3]. They mixed ionic polymer solution with electrically conductive powder and applied the mixture on both surfaces of the ionomer by either using a brush or painting on Furon and then hot-pressing these decals on

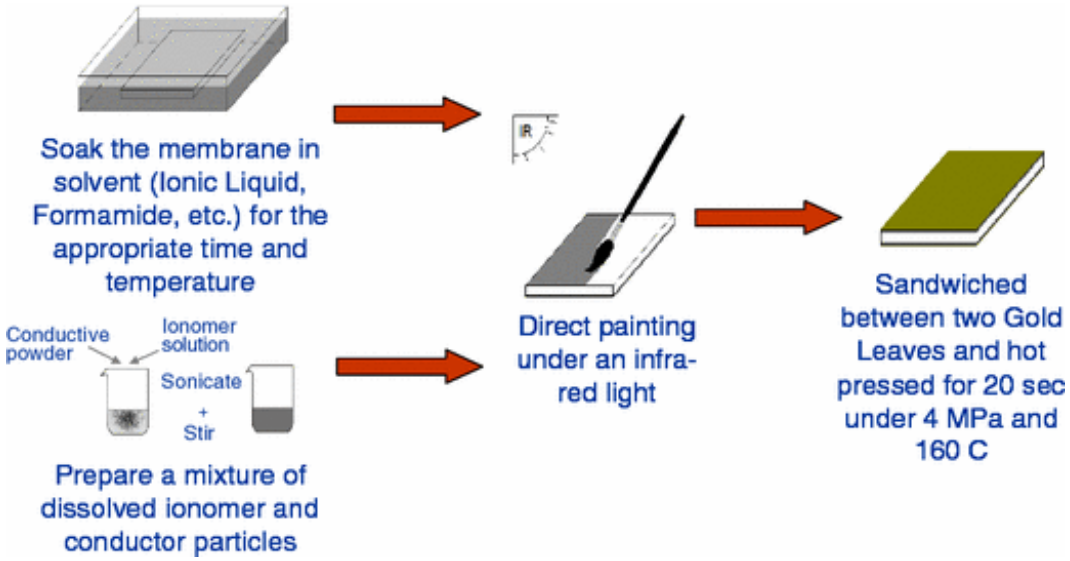

Figure 1.6: Schematic representation of the four steps of direct assembly process for building solvated transducers developed by Akle and Bennett *et al.*[3].

the ionomer. Both dry membranes and solvated membranes can be applied in this process. Figures 1.5 and 1.6 schematically represent the direct assembly process steps for building dry and wet transducers, respectively.

This direct assembly process increases the effective interfacial area between the electrode and ionomer by a factor of 5−10 compared with a conventional impregnation-reduction process. The corresponding performance of an IEAP actuator fabricated with the direct assebly process exceeds the performance of an IEAP actuator fabricated with conventional impregnation-reduction process by a factor of 2−5[71]. Another attractive property of direct assembly process is that this technique makes it possible to adopt some other materials including carbon nanotubes and non-metallic nanoparticles in CNCs[76].

1.3.4.3 Layer-by-layer self-assembly process

Layer-by-Layer (LbL) self-assembly technique is a process to build up an ultra-thin multilayer film upon the use of oppositely charged polyelectrolytes, DNA, conducting polymers, proteins, and nanoparticles. This technique yields an easy controlled structure on the nano- or microscale, which combines two or more desirable properties of its componenets and avoids their weakness at the same time. This LbL self-assembly adsorption from aqueous solution was

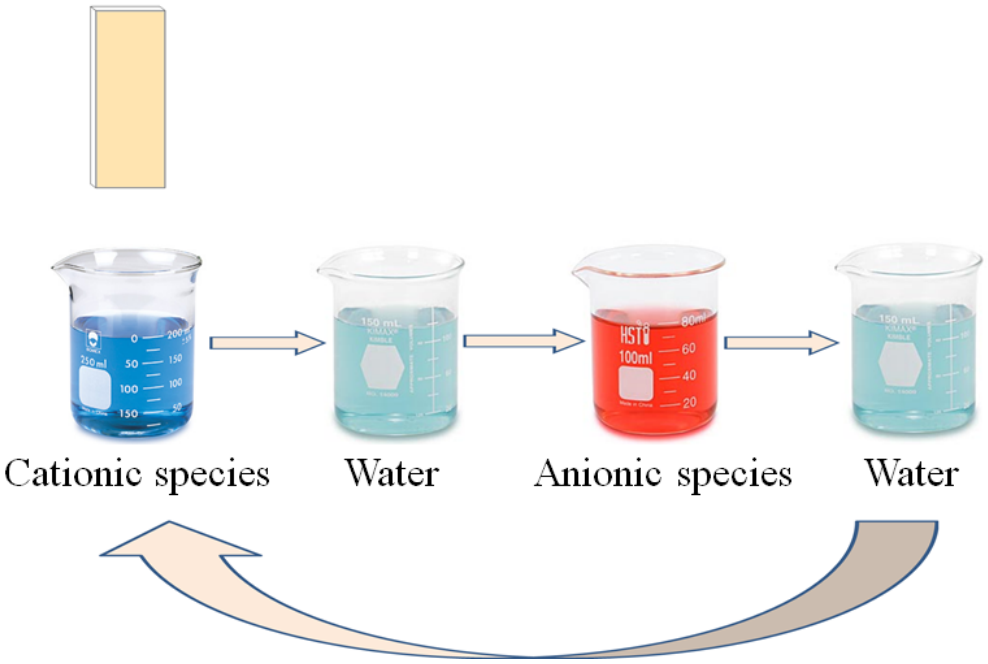

Figure 1.7: Schematic representation of the film deposition process using a slide and beakers. Beakers with cationic and anionic species represent the adsorption process; beakers with water represent washing step. The order of cationic and anionic species depends on the original surface charge of the slide. This schematic assumes the slide has negative surface charge at the very beginning.

presented and discussed detailedly by Decher and Hong *et al.* since 1991[77, 78, 79]. In this technique, a functionalized substrate is alternatively immersed in cationic and anionic species (or in a reversed order, depending on the original surface charge of the substrate). Each exposure forms one layer and the original surface charge is restored to provide the foundation to the next layer. Each set of two consecutive exposures to oppositely charged species results in formation of a bilayer. Rinsing by water is also necessary after each exposure to remove loosely bonded species. Figure 1.7 is a schematic representation of a LbL self-assembly deposition cycle using a slide and beakers, and Figure 1.8 shows formation of two bilayers.

With many advantages, LbL self-assembly technique has become one of the most preferred techniques to fabricate thin-films since it was reintroduced in 1991. First it offers freedom in materials selection, virtually any specie with non-zero net charge can be used. It allows different kinds of active elements incorporated into the thin-film without losing their intrinsic properties including electric and chemical properties. It also allows different kinds of substrates

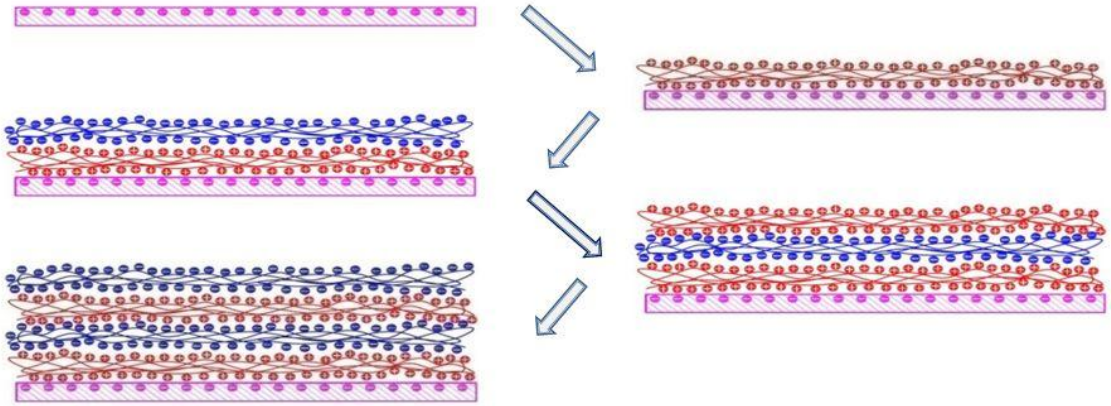

Figure 1.8: Schematic of formation of two bilayers through adsorption[1].

for the thin-film deposition, from ITO coated glass slide, to flexible surfaces such as Nafion or Teflon. Second, LbL self-assembly technique makes it possible to build a multi-material complex structure at the nanometer scale, and various components can be tuned on a molecular level. The control over the thickness of the thin-film can be accurate to tens of nanometers, which is $1-2$ orders of magnitude higher in comparison to the films made by other methods such as spin-coating and screen casting. In addition, the thin-film deposited by this technique is uniform, which makes it applicable in many sophisticated products such as permselective thin-films[80, 81, 82, 83, 84, 85], electrochromic thin-films[86, 87, 88, 89] and nanomechanical thin-films[90, 91]. Polymeric materials formed by LbL self-assembly technique, both in the forms of capsules and thin-films, also have promising applications in biomedical implant devices such as drug delivery vehicles[92, 93].

Due to its unique properties and easy operation, LbL self-assembly technique has been adopted for developing CNC nanocomposites in IEAP actuators by Liu *et al.* and by us in recent years[40, 4, 39, 13, 37, 38, 41, 94]. It has been reported that higher strain and bending curvature can be achieved by employing the LbL technique to form CNC layers consisting of gold nanoparticles (AuNPs) and polycation poly(allylamine hydrochloride) (PAH). Moreover, the thickness and morphology of the CNC layers can be directly controlled by adjusting the number of the deposited bilayers and composition of the deposited species. The achieved ultra-thin, uniform and highly conductive CNC layer acts as a reservoir for mobilized ions and

improves the capacitance at the interface between the electrode and polymer. As a result, a higher strain was achieved.

1.3.4.4 Our studies

Influence of CNC layers on the performance of IEAP devices is studied in this dissertation.

In one of studies reported in this dissertation, LbL self-assembly technique was adopted to fabricate the CNC nanostructures in IEAP stress sensors. The electrochemical and morphological studies of CNCs were conducted and its influence on the sensing performance was explored. More details of this work are presented in Chapter 2.

Another study is to achieve soft IEAP actuators with tunable limb-like deformation by incorporation of patterns of conjugated polymers. Details of this work are discussed in Chapter 5.

1.3.5 Electrode

Usually a layer of precious metal is attached on each surface of ionomeric membrane as an electrode for two main reasons. First it distributes the electric charge uniformly across the surface of the device. Second, it limits evaporation of the electrolyte. Precious metals such as silver, gold and platinum are good candidates for the electrode deposition and usually the deposited layer is ultra-thin to minimize the blockage force.

In the studies reported in this dissertation, a layer of gold leaf is hot-pressed on each side of IEAP devices as an electrode.

CHAPTER 2. ELECTROCHEMICAL AND MORPHOLOGICAL STUDIES OF IONIC POLYMER METAL COMPOSITES AS STRESS SENSORS

A paper accepted by the journal of Measurement

Wangyujue Hong, Abdallah Almomani, Reza Montazami

Abstract

Ionic polymer metal composites (IPMCs) are the backbone of a wide range of ionic devices. IPMC mechanoelectric sensors are advanced nanostructured transducers capable of converting mechanical strain into easily detectable electric signal. Such attribute is realized by ion mobilization in and through IPMC nanostructure. In this study we have investigated electrochemical and morphological characteristics of IPMCs by varying the morphology of their metal composite component (conductive network composite (CNC)). We have demonstrated the dependence of electrochemical properties on CNC nanostructure as well as mechanoelectrical performance of IPMC sensors as a function of CNC morphology. It is shown that the morphology of CNC can be used as a means to improve sensitivity of IPMC sensors by 3−4 folds.

2.1 Introduction

Ionomers, especially Nafion, have been subject of numerous investigations for their ionic properties and applications in ionic-electric devices such as fuel cells[95, 96, 97, 98], actuators[39, 17, 99, 100, 101], batteries[102, 103, 104, 105], super capacitors[106] and sensors[107, 108, 14, 109]. Among all such applications, ionic polymer sensors have received less attention mainly due to apparently inconsistent experimental results[110, 111, 112, 113]. Similar to ionic polymer actuators, ionic polymer sensors are consisted of an ionomer membrane coated by conductive

network composites (CNCs) on both sides, where the whole structure (also known as ionic polymer-metal composite (IPMC)) is doped by either aqueous or ionic liquid electrolyte. The functionality of ionomeric sensors relies on, supposedly, random displacement of ions (and charged ionic clusters if ionic liquids are used) throughout the CNC layers when an external mechanical stress is applied. Electric voltage generated due to the motion of charged species is collected by the CNC and is detectable by conventional electronics. Due to the presence and displacement of both cations and anions in IPMC, theoretically there should be a zero net charge as opposite fields generated by displacement of cations and anions are expected to be statistically very close to each other in magnitude and cancel one another. In reality, however, there is a non-zero detectable net electric voltage. This electric voltage (mechanoelectric signal) exists because, due to their volume, charge and interactions with the ionomer, motions of cations and anions are different when subjected to stress[14, 47].

Influence of CNC structure[40, 13], ion density[15], electrode properties[41] and chemical and ionic structure of ionomer membrane[16] on performance of IPMC actuators have been thoroughly investigated by others and us; similar studies on IPMC sensors, however, are not widely reported. To our best recollection, one of the first reports on Nafion-based sensors was published by Sadeghipour *et al.* in 1992[43] where the concept was introduced. Later in 1995, Shahinpoor *et al.* investigated the response of IPMC sensor against large imposed displacements[44]. They published the first review paper of IPMC as biomimetic sensors and actuators in 1998, presenting an introduction to IPMC, its applications and the corresponding mathematical modeling[113]. In 1999 Ferrara *et al.* proposed the possibility of applying IPMC sensor as a pressure transducer in the human spine[109]. Over the same time period, studies on mathematical modeling of IPMC sensors were also conducted and published[70, 48, 49, 50]. All of the abovementioned studies considered the IPMC sensors doped with aqueous electrolytes; studies on the ionic liquid-doped IPMC sensors, however, are rare.

In this work, we have investigated the correlations between the mechanoelectric sensing performance of IPMC sensors and structural and morphological properties of ionic liquid-doped CNC layers. IPMC sensors were fabricated by layer-by-layer (LbL) (Figure 2.1a) deposition of CNC layers consisting of gold nanoparticles (AuNPs) and poly(allylamine hydrochloride)

(PAH) on Nafion membranes. LbL fabrication technique was utilized to manipulate structural properties of CNC layers. IPMCs provide environments for storage and mobility of ions. Ion mobility through IPMC, due to the porous structure of CNC layers, is higher compared to dense ionomer membrane; thus, porosity and structural properties of IPMC is an influential factor in performance and attributes of the sensors. This work specifically contributes to the knowledge of ionic and electrical properties of ionic liquid-doped nanostructured IPMCs, as well as the potential applications of such structures as mechanoelectric sensors.

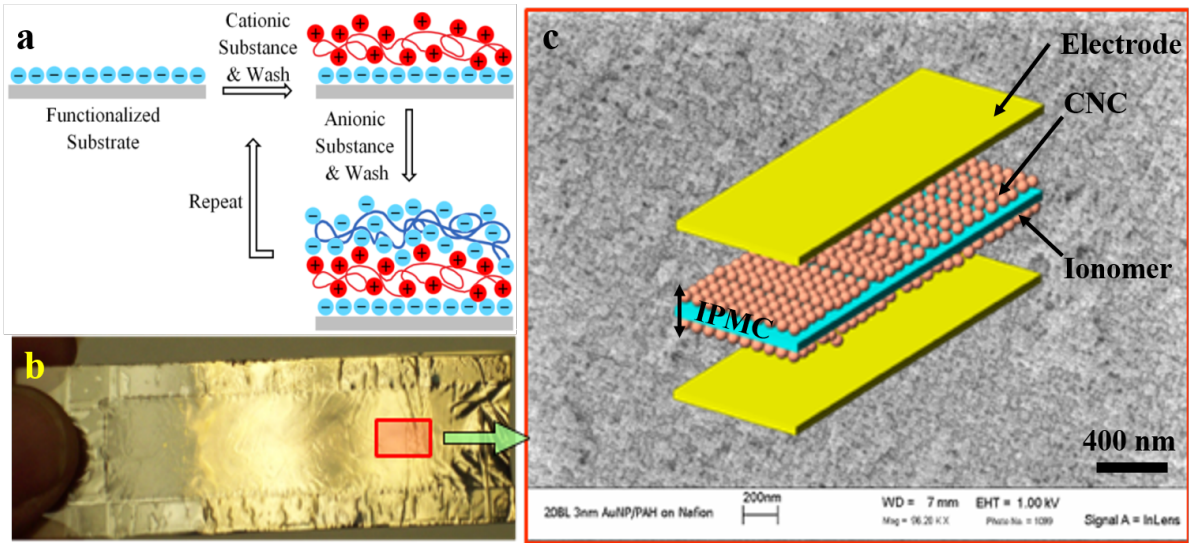

Figure 2.1: (a) Schematic representation of layer-by-layer direct self assembly of AuNP and PAH; (b) CNC layer formed on Nafion ionomer, the membrane is mounted on a glass frame; (c) foreground: schematic representation of IPMC and sensor structure, background: SEM micrograph of AuNP/PAH CNC nanostructure.

2.2 Experimental Section

2.2.1 Materials

Nafion membrane of 25 μm thickness (NR 211) was purchased form Ion Power, Inc. and was cut into pieces of 2.5 cm $\times$ 5 cm. Poly(allylamine hydrochloride) (PAH) was purchased from Sigma Aldrich and used to make 10 mM polycationic aqueous solution of pH 4; 1-ethyl-3-methylimidazolium trifluoromethanesulfonate (EMI-Tf) and sodium chloride (NaCl) were pur-

chased from Sigma Aldrich and used as received. 20-ppm aqueous dispersion of 3 nm (diameter) negatively charged gold nanoparticles (AuNPs) of pH 9 were purchased from Purest Colloids, Inc. and used without further modification. 3 M conductive copper tape was purchased from VWR International LLC and used as current collector.

2.2.2 Methods

2.2.2.1 IPMC fabrication

An automated thin-film fabrication robot (StratoSequence 6, NanoStrata, Inc.) was used to grow AuNP/PAH CNCs of desired number of bilayers via LbL deposition technique. Nafion membrane was mounted on a glass frame and was alternately exposed to cationic (10 mM PAH aqueous solution) and anionic (20-ppm aqueous dispersion of AuNPs) species for 5 minutes each, with three steps of 1 minute each DI water rinsing after each deposition step. CNCs consisting of 2, 4, 6, 8 and 10 bilayers were obtained to investigate thin-film growth on ionomer membrane; CNCs consisting of 10, 20, 30 and 40 bilayers were obtained for electrochemical studies. Thin-film thicknesses (h, see Table 2.1) were measured using a contact profilometer as described in our earlier work[40].

Moreover, to further study the effect of ionic strength of polyelectrolyte on CNC morphology, 200 mM NaCl was added to PAH solution to manipulate its ionic strength and consequently its polymer chains configuration. 20 bilayer CNCs with and without NaCl were fabricated to investigate the influence of morphology on the sensing performance. The samples were labeled $(\text{AuNP/PAH-NaCl})_{20}$ and $(\text{AuNP/PAH})_{20}$, respectively, where the subscript 20 identifies the number of deposited bilayers constituting the CNCs. Presented in Figure 2.1b is an $(\text{AuNP/PAH})_{20}$ IPMC on a glass frame. Figure 2.1c, background, shows a SEM micrograph of the CNC coating and a schematic of the device is presented in the foreground. CNC coated ionomer membranes were then soaked in EMI-Tf ionic liquid at 80 °C to intake ∼30 wt% ionic liquid. Considering the high sensitivity of Nafion and EMI-Tf ionic liquid to humidity[114, 115], samples were then placed under vacuum (gauge pressure of ~ -100 kPa) at 115 °C for three days to dehydrate, and kept in desiccator until used.

2.2.2.2 Optical characterization

Optical spectrum was acquired on CNCs to characterize the LbL self-assembled thin-films, using a PerkinElmer Lambda−25 UV/VIS Spectrometer.

2.2.2.3 Electrochemical characterization

Samples doped with ionic liquid were characterized for their electrochemical properties using a VersaSTAT−4 (Princeton Applied Research) potentiostat on 2−electrode mode. Impedance spectroscopy studies were carried at frequencies between $1.0E5$ Hz and $1.0E-1$ Hz, and a potential difference (ΔV) of 10 mV. Electrical conductivity (σ) of the doped membranes was calculated from Equation 2.1,

$$\sigma = \frac{h}{RA} \tag{2.1}$$

where h and A are representing thickness and area of the membrane, respectively; and R is the resistance deduced from impedance spectroscopy measurements.

2.2.2.4 Mechanoelectrical characterization

Stress induced dynamic electric response was measured and recorded to study mechano-electrical properties of the samples. Samples were cut into pieces of approximately 14 mm × 17 mm. Copper tape was used as electrodes and the whole system was covered by electrical tape to form an isolated sample. The samples were placed flat and tested on an in-house made setup at frequency of 1 Hz. A 12 kPa stress was generated and distributed uniformly across the sensor by reciprocating motion of a mass manipulated by a computer controlled stepper motor. A schematic representation of the setup is presented in Figure 2.2. Two ends of the sample were clamped and connected to an oscilloscope to monitor the generated electric signal, which was recorded via a LabVIEW interface over an extended period of time.

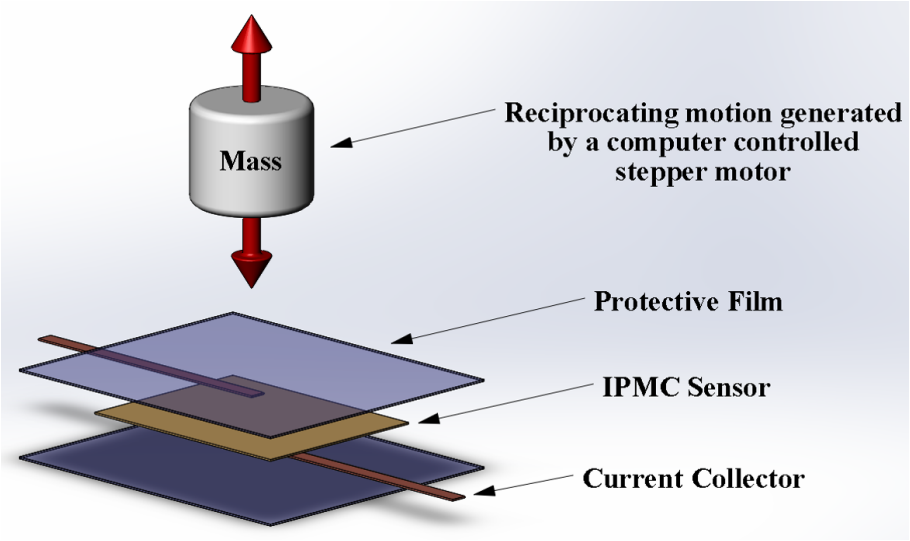

Figure 2.2: A schematic representation of the setup and operations for the mechanoelectrical characterization (dimensions are not to scale). The IPMC sensor piece was covered by electrical tape, with copper tape used as electrodes to connect to an oscilloscope to monitor the generated electric signal. A 12 kPa stress was distributed evenly by a mechanical arm whose frequency was controlled at 1 Hz by a step motor.

2.3 Results and Discussion

2.3.1 Morphological characterization

Growth kinetics of CNC nanostructures, consisting of AuNP/PAH with and without addition of NaCl to the PAH solution, was investigated. Presented in Figure 2.3a is the plasmonic absorption band of 3 nm diameter AuNPs, centered at 514 nm. When paired with PAH to form LbL nanostructures, the absorbance peak shifted toward longer wavelengths (Figure 2.3b); which is an indication of the enhanced electromagnetic coupling between neighboring nanoparticles[116], and it is more evident in nanostructures of larger thicknesses because a more closely packed structure is formed. Increase in the absorbance intensity implies an increase in the thickness of the CNC film. The correlations of ionic strength of polyelectrolyte and film thickness in LbL self-assembly are discussed by several researchers including[117, 118, 119, 120].

Intensity of the absorbance peaks of the AuNP/PAH bilayers showed a direct and linear dependence on the thickness of the nanostructures (Figure 2.3c). The linear correlation between thickness and peak absorbance amplitude is an indication of consecutive surface-charge buildup

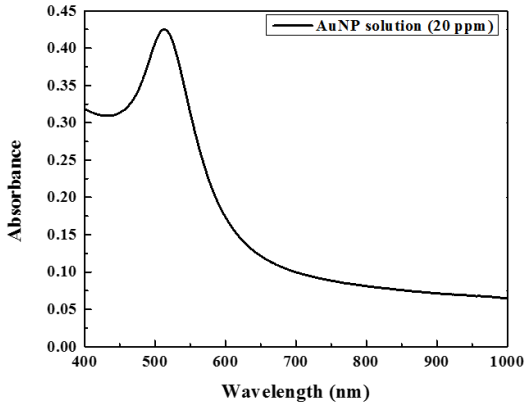

(a)

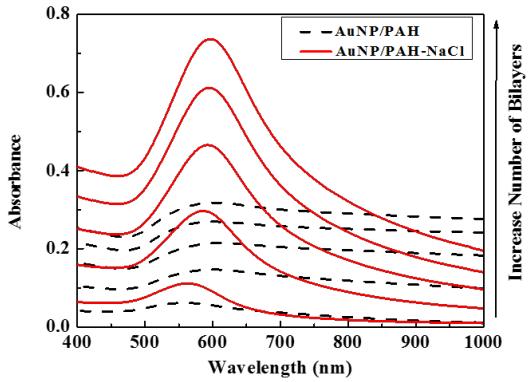

(b)

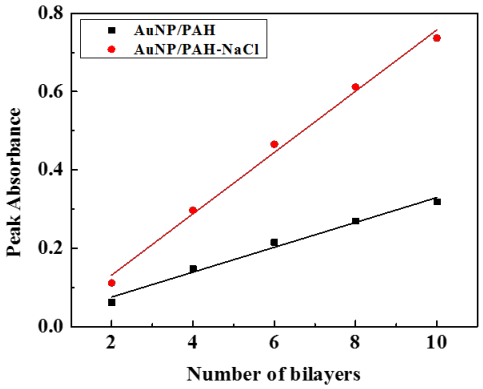

(c)

Figure 2.3: (a) UV-Vis absorbance spectra of AuNP aqueous solution (20 ppm); (b) UV-Vis absorbance spectra of 2, 4, 6, 8, and 10-bilayer AuNP/PAH and AuNP/PAH-NaCl nanostructures; (c) plot of the absorbance peaks of CNCs consisting of different number of bilayers and morphology.

of AuNPs in the nanostructure[121]. Addition of NaCl to PAH resulted in formation of thicker and denser nanostructures; thus, the increase in absorbance intensity for CNCs consisting of larger number of bilayers is significantly more evident compared to that of samples without NaCl (Figure 2.3c); this is mainly due to an increase in ionic strength of the polycation which results in accumulation of more negatively charged AuNPs and formation of thicker and denser bilayers.

2.3.2 Electrochemical analysis

To study thickness dependence of the frequency response in IPMC sensors and the corresponding electrical efficiency, the electrical impedances of sensors with CNC layers consisting of different number (0, 10, 20, 30 and 40) of bilayers were investigated as a function of frequency. Applied potential of 10 mV was selected so that the electric impedance can be characterized over a broad frequency range with required accuracy. Typically, the electrochemical responses of such ionic devices are nonlinear functions of the CNC morphology and applied voltage, thus different CNC structures (e.g. with or without NaCl) and changes in the applied voltage will affect the numerical values of the electrical impedance results; for example, the capacitance will increase with increase of applied voltage. However, these nonlinear effects will not change the trends and conclusions drawn from the experimental results[4].

Presented in Figure 2.4a are the curves of Nyquist plot for the IPMC sensors at higher frequencies, where the electrochemical systems exhibited near-pure resistance behavior. Solution resistance (R) is deduced by reading the Z_{re} value at the intersection of extended curves and the x-axis. As discussed in our previous works[102, 15], solution resistance depends on the ionic conductivity of the entire system including the transportation of ions between anode and cathode. Thicker CNC layers result in smaller solution resistances, indicating the presence of an ion-rich environment in thicker CNC nanostructures. Ionic conductivity of the IPMC sensors is calculated from Equation 2.1 and reported in Table 2.1 along with solution resistance and other characteristics of the IPMC sensors.

Magnitude of electrical impedance $|Z|$ and phase angle (ϕ) for IPMC sensors consisting of different thickness CNCs as a function of frequency (f) are presented in Figures 2.4b and 2.4c.

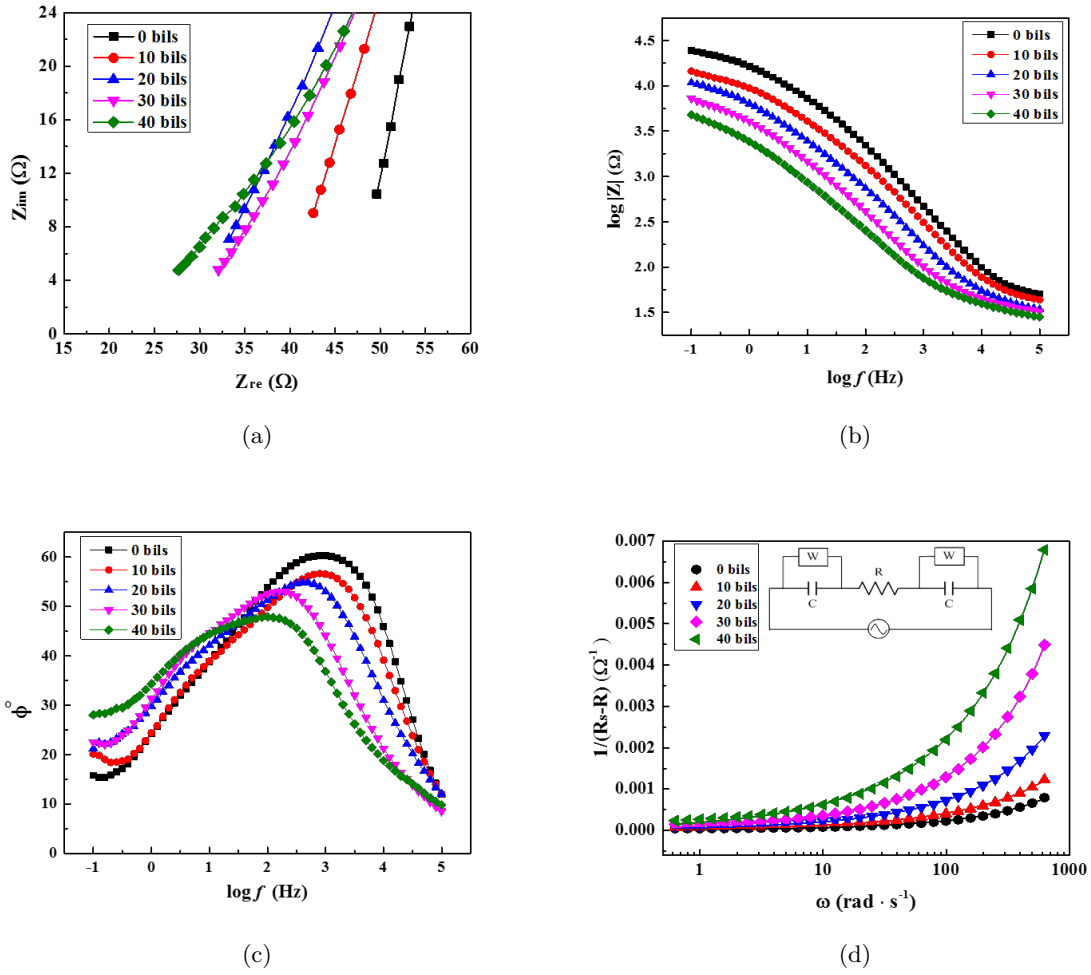

Figure 2.4: Electrochemical studies of IPMC sensors consisting of different thickness CNCs (without NaCl) (a) Nyquist plot of impedance magnitude of IPMC sensors. Solution resistance values are deduced from the intersection of plots with the axis; (b) Impedance magnitude as a function of frequency; (c) phase angle as a function of frequency; (d) plots of $1/(R_s - R)$ versus ω, and their corresponding fitting lines based on the equivalent circuit (inset).

Table 2.1: Solution resistance, ionic conductivity and electric double layer capacitance of IPMC sensors with various thicknesses of CNC layers.

Bilayers	**0**	**10**	**20**	**30**	**40**
h (μm)	25.000	25.046	25.084	25.128	25.162
A (cm^2)	1	1	1	1	1
R (Ω)	45.0	38.4	29.4	27.7	23.8
σ (S·cm^{-1})	$5.56E-5$	$6.52E-5$	$8.53E-5$	$9.07E-5$	$10.58E-5$
C (F·cm^{-1})	$3.64E-7$	$3.62E-7$	$9.37E-7$	$2.32E-6$	$2.67E-6$

As evident from Figure 2.4a, impedance $|Z|$ is inversely proportional to the thickness of CNC layer. This behavior is especially more evident at lower frequencies (0.1-100 Hz). In general, for an IPMC sensor to response to an external mechanical stimulus and deliver an electric signal, a large capacitance is preferred. At the same low frequency range, phase angle, which is a function of frequency, exhibited a direct correlation to the thickness of the CNC nanostructure (Figure 2.4c), suggesting a stronger capacitance-like behavior for samples with thicker CNC layer; this characteristic is hindered at higher frequencies. To achieve high electrical efficiency in IPMC sensors, larger phase angles are preferred; which, can be realized by increasing the thickness of the CNC layers in sensors for low frequency (<100 Hz) applications.

An equivalent circuit, as shown in Figure 2.4d-inset, was introduced to study the electrochemical behavior of IPMC sensors at lower frequency boundaries, between 0.1 and 100 Hz, as a function of thickness of the CNC layer. Briefly, an electric double layer (EDL) capacitor (C) is formed at the interface between the outer electrodes and electrolyte, with a Warburg impedance element (W) connected in parallel to represent diffusion controlled charge transfer process in pseudo-capacitors. Both elements are then connected with a solution resistor (R) in series to represent the bulk resistance between two electrodes. The net real resistance of the system (R_s) can be expressed as the sum of the solution resistance (R) and real part of the impedance (Z_{re}) as

$$R_s = R + \frac{2Y_0\omega^n cos(n\pi/2)}{Y_0^2\omega^{2n} + \omega^2C^2 + 2\omega^{n+1}CY_0 sin(n\pi/2)}$$

which can be reorganized to

$$\frac{1}{R_s - R} = \frac{Y_0\omega^n}{2cos(n\pi/2)} + \frac{C^2\omega^{2-n}}{2Y_0cos(n\pi/2)} + \omega Ctan(\frac{n\pi}{2})$$

Take $n = 0.5$ for a Warburg element and rewrite the equation to

$$\frac{1}{R_s - R} = \frac{\sqrt{2}}{2}\frac{C^2\omega^{1.5}}{Y_0} + C\omega + \frac{\sqrt{2}}{2}Y_0\omega^{0.5}$$

More details of this model is presented in our previous study[15]. Experimental data (symbol) fitted with computational data (solid line) are shown in Figure 2.4d, confirming viability of the presented equivalent circuit. The computational data of the EDL capacitor (represented as C in the circuit) at each sample was deduced and is listed in Table 2.1. A general upward trend was observed with increasing thickness of CNC layer, confirming the hypothesis that a thicker CNC layer has a larger ion storage volume and can withhold more mobile ions at the electrodes[40].

2.3.3 Mechanoelectrical sensing performance

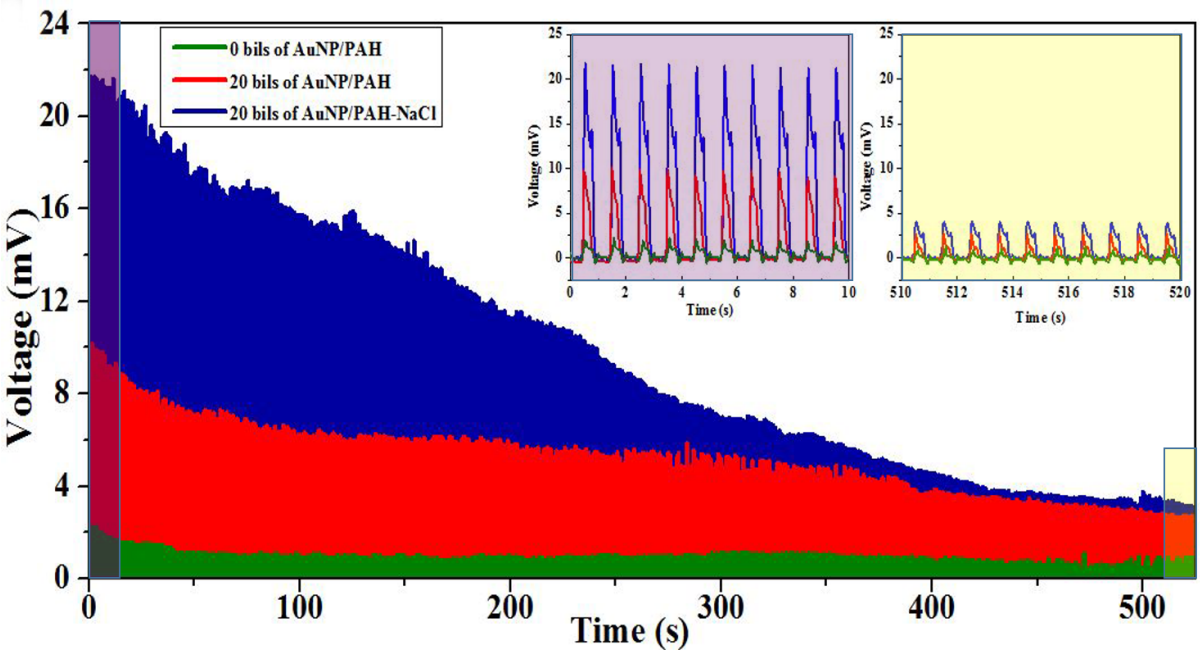

Figure 2.5: Mechanoelectric sensing in repose to cyclic 12 kPa stress at 1 Hz. Insets show the zoomed in plots at the first and last 10 seconds of the experiment.

When mechanically deformed, IPMC sensors generate a weak yet detectable electric potential, which is the core of the "sensing" concept of such systems. Mechanism and theory of

such mechanoelectrical behavior of systems doped with aqueous electrolytes have been studied thoroughly and reported[108, 14, 113, 70]. It is hypothesized that prior to application of mechanical stress, and the consequent deformation, the cations and anions are distributed uniformly over the inner surface of ionic cluster phase of Nafion. This steady state of zero net charge, however, is disturbed and distorted by the imposed deformation. Consequently, ions (either both types, or anions only depending on the system properties) are displaced producing an effective dipole in each cluster[39, 13, 70, 4]. Moreover, the existence of homogenous and porous CNCs outside the Nafion in this work promotes the motion of ions in varying degrees. This generated electric voltage is treated as the dynamic sensing response and analyzed in this work. Three sets of samples (bare Nafion $(\text{AuNP/PAH})_0$, $(\text{AuNP/PAH})_{20}$ and $(\text{AuNP/PAH-NaCl})_{20}$), were studied for the mechanoelectrical characterization. Sample selection was in such way that the role of CNC and its morphology can be examined. Samples were subjected to cyclic mechanical stress of 12 kPa at 1 Hz for over 500 cycles, until sensing signals were stable in amplitude. Presented in Figure 2.5 is the mechanoelectrical response of the three sets of samples; insets shown zoomed in signals in the beginning and the end of the testing period. Initially, signals generated by the samples with CNC coating were 5 to 11 folds stronger than that of the uncoated samples. Amplitude of all signals declined overtime and reached a stable state where the signals from coated samples were approximately 4 folds stronger than the uncoated sample. Samples with and without NaCl in the CNC structure reached approximately the same stable plateau. The dynamic response was observed to be highly repeatable with a bandwidth of 1 Hz for all three samples. Each peak rises almost instantaneously when the pressure is applied, and recovers when the pressure is withdrawn. To confirm reproducibility and statistical significance of the collected data, three runs were conducted on each of the three sets of samples, and the standard deviation of each data set was calculated. For the three sets of samples ($(\text{AuNP/PAH})_0$, $(\text{AuNP/PAH})_{20}$ and $(\text{AuNP/PAH-NaCl})_{20}$), the standard deviation range (minimum/maximum) was found to be $(6.7E-6/1.7E-3)$, $(0/4.7E-3)$ and $(0/7.5E-3)$, respectively.

Experimental data suggests that there is a strong correlation between the morphology of CNC layers and mechanoelectrical response in IPMC sensors. A higher concentration of AuNPs

in CNC results in higher porosity that facilitates higher ion mobility under mechanical impact. This enhanced ion mobility, however, is declined to a common and stable plateau for IPMC sensors regardless of the nanostructure of the CNC. This observation may be due to loss of elasticity, or creep of the IPMC at microscale. For samples without CNC the signal amplitude is considerably weaker. Overall, the CNC layer results in at least $3-4$ folds increase in the strength of the sensing response; no dependence was observed between the structure of IPMC and the response time of the sensors.

2.4 Conclusions

We reported the study of correlations between structural properties of IPMC sensors and their electrochemical and mechanoelectrical properties and performance. It was demonstrated that changes in nanostructure and morphology of CNC layers could be utilized as a means to control and enhance the sensitivity of mechanoelectric IPMC sensors by at least 3 to 4 folds. Initially optimized samples exhibited 11 folds increase in their sensitivity to mechanical strain; the overall amplitude of the electrical signal, however, declined over hundreds of cycles, most probably due to creep formation and mechanical failure of the IPMC. Better casing and more robust IPMCs are expected to overcome this issue. It is foreseen that future work would involve exploration of effective techniques to reduce the stabilization time of such sensor systems.

Acknowledgment

The presented work is supported in part by grants from Health Research Initiative (HRI), Presidential Initiative for Interdisciplinary Research (PIIR), and the Department of Mechanical Engineering at Iowa State University.

CHAPTER 3. INFLUENCE OF IONIC LIQUID CONCENTRATION ON THE ELECTROMECHANICAL PERFORMANCE OF IONIC ELECTROACTIVE POLYMER ACTUATORS

A paper published in Organic Electronics 15 (2014): 2982−2987

Wangyujue Hong, Abdallah Almomani, Reza Montazami

Abstract

We have investigated influence of ionic liquid concentration on the electromechanical response of ionic electroactive polymer actuators. Actuators were fabricated from ionomeric membrane and doped with different concentrations of 1-ethyl-3-methylimidazolium trifluoromethanesulfonate ionic liquid. Samples were investigated for their electromechanical and electrochemical characteristics; and it was observed that the maximum electromechanical strain of approximately 1.4% is achieved at 22 wt% ionic liquid content. Increasing ionic liquid concentration results in saturation of the electrodeionomer interface and formation of ionic double/multi layers, which in turn result an inward accumulation of ions; hence, generate strain in an undesired direction that deteriorates the electromechanical response of the actuator.

3.1 Introduction

Recently, electroactive polymers have received immense attention and interest from the materials community because of their applicability to actuators, sensors and haptics [122, 12, 123]. Electroactive polymers are soft and lightweight; hence, enable realization of biomimetic and microrobotic devices. Among wide variety of electroactive polymers, ionic electroactive polymers (IEAP) have proven more practical for actuator applications due to their substantially low operation voltage (typically < 5 V), light weight, relatively large strain, and bending

(instead of linear) deformation [124, 43]. IEAP actuators comprise of an ionomer membrane that is doped with an ion-rich electrolyte and coated with electrodes on each surface [41, 39]. The electromechanical response is upon attraction/repulsion of ions and their accumulation at the oppositely charged electrode when subjected to an external electric voltage. Due to the volume difference between cations and anions, cathode and anode swell to different extents, thus a volume imbalance is generated in the actuator, which in turn causes a mechanical deformation. Change in the polarity of the electric voltage reverse the process and direction of bending [38, 4, 40, 13, 37, 125, 126].

Ions are sourced by either an aqueous electrolyte or ionic liquid (IL). Ionic liquids are preferred as their near zero vapor pressure allows longer shelf life, operation in air, and higher operation voltages without concerns about ionomer hydration or electrolysis of water in aqueous electrolytes [12, 69, 42]. Also, substantially higher ion concentration in ionic liquids, compare to that of aqueous electrolytes, and larger van der Waals volume difference between molecular cations and anions (compare to atomic cations and anions in aqueous electrolytes) result in an enhanced performance of IEAP actuators doped with ionic liquids, compare to those doped with aqueous electrolytes. These characteristics along with scalable manufacturing and flexibility in design allow integration of IEAP actuators in flexible organic electronics, microrobotics, biomimetic devices and bioelectronics [127].

In the present study, we have demonstrated that the electromechanical performance of IEAP actuators is influenced by the concentration of ionic liquid, and that the concentration of ionic liquids can be tuned to achieve maximum actuation performance. Ionic liquids concentration in IEAP actuators was varied while electromechanical and electrochemical properties were characterized. It is shown that the ionic liquid concentration can be used as a means to control, improve and optimize actuation performance; and that at high concentrations of ionic liquid an ionic double/multi-layer forms at the ionomerelectrode interface which deteriorate the actuation strain.

3.2 Materials and Methods

3.2.1 Sample preparation

Commercially available Nafion membrane of 25 μm thickness (Ion Power, Inc.) was used as the ionomeric membrane. To fabricate IPMCs, nanocomposites of the polycation poly(allylamine hydrochloride) (PAH) (Sigma Aldrich) and anionic functionalized gold nanoparticle (AuNP) ($\sim$ 3 nm diameter, Purest Colloids, Inc.) were grown on both sides of the Nafion membrane via LbL deposition of the ionic species, using a StratoSequence 6 (NanoStrata, Inc.) automated thin-film fabrication robot. The substrates were alternately immersed for 5 min each in aqueous solutions of PAH at a concentration of 10 mM at pH 4.0 and AuNP at a concentration of 20 ppm at pH 9.0 with three rinsing steps for 1 min each in de-ionized water after each deposition step. IPMCs were then soaked with 1-ethyl-3-methylimidazolium trifluoromethanesulfonate (EMI-Tf molecular formula: $C_7H_{11}F_3N_2O_3S$) (Sigma Aldrich) ionic liquid at 80 °C for various durations of time to intake desired concentrations of ionic liquid. Ionic liquid content was measured as the weigh percentage (wt%) of dry weight of the membrane, and calculated from Equation 3.1.

$$W_e(\%) = \frac{W_f - W_d}{W_d} \times 100 \tag{3.1}$$

where $W_e(\%)$ is the weight-percent of the electrolyte; and, W_d and W_f are the weights of dry and doped samples, respectively. Gold leaf electrodes of 50 nm thickness were then hot-pressed at 95 °C under 1000 lb_f for 25 s on both sides of the membrane to form IEAP actuators.

3.2.2 Electrochemical characterization

Impedance spectroscopy and current flow were measured and recorded using a VersaSTAT-4 potentiostat (Princeton Applied Research). The impedance spectroscopy studies were carried at frequencies between $1.0E5$ Hz and 0.1 Hz, and a potential difference (ΔV) of 10 mV. Current flow was monitored in response to a $\pm$4 V step potential over 60 s intervals. Electrical conductivity (σ) of the doped membranes was calculated from Equation 3.2,

$$\sigma = \frac{h}{RA} \tag{3.2}$$

based on the geometry of the membranes where h and A represent thickness and area of the membrane, respectively; and R is the resistance deduced from impedance spectroscopy measurements.

3.2.3 Electromechanical characterization

Actuators were cut into approximately 1.5×15 mm^2 pieces and tested under application of a 4 V step potential. Electromechanical response of the actuators was monitored and recorded using a charge-coupled device (CCD) video camera, mounted to an in-house fabricated micro-probe station, at 30 fps. Individual frames were then analyzed to measure the radius of curvature as a function of time (r(t)) and to calculate (Q(t)) and strain ($\varepsilon\%(t)$) values from Equation 3.3 and 3.4, respectively; where Q, ε and h are curvature, strain and thickness of the actuator, respectively.

$$Q(t) = \frac{1}{r(t)} \tag{3.3}$$

$$\varepsilon\%(t) = \frac{h}{2r(t)} \times 100 \tag{3.4}$$

3.3 Results and Discussions

3.3.1 Current flow

Current flow corresponding to a 4 V potential difference between the outer electrodes was measured and recorded as a function of time. As presented in Figure 3.1, magnitude of displaced charge (area under the curve) increases with the increasing concentration of ionic liquid in the samples; suggesting that first, current flow is due to mobilized ions; and second, more ions are displaced in samples containing higher concentration of ionic liquid. After approximately 55 s (see $55 < t < 60$ and $115 < t < 120$ on Figure 3.1) all curves have asymptotically reach the x-axis (approximately zero current) indicating that the system is fully charged.

3.3.2 Electromechanical response

The electromechanical responses of IEAP actuators to an external 4 V DC step voltage were monitored and recorded at a rate of 30 frames/s. Sequential digital images were used to

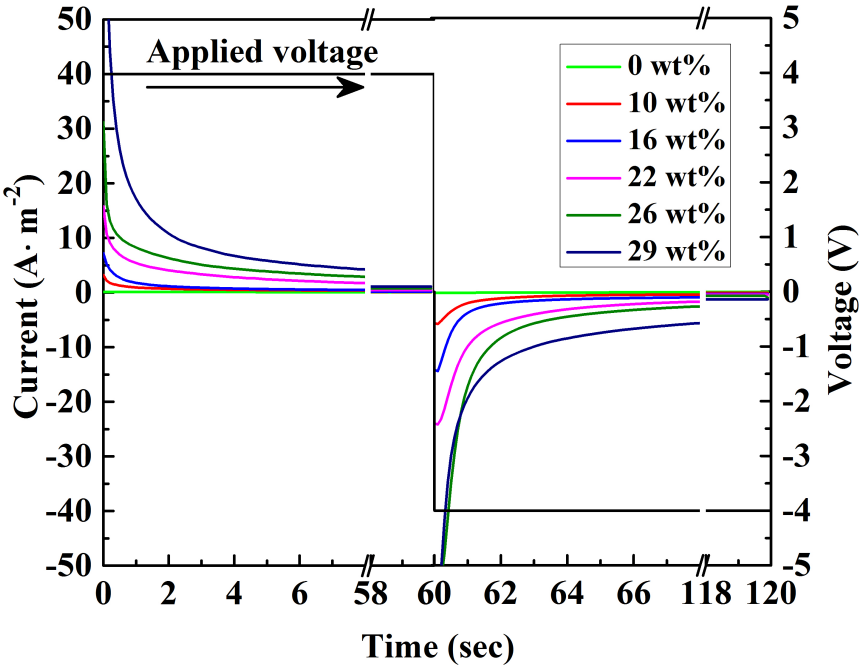

Figure 3.1: Charging and discharging currents for samples containing different ionic liquid concentrations recorded as a function of time under a 4 V square wave.

deduce $r(t)$ and to calculate $Q(t)$ and $\varepsilon\%(t)$ of each IEAP actuator. Presented in Figure 3.2 is the maximum actuation curvature and strain as a function of ionic liquid concentration. The electromechanical response showed enhancement as the concentration of ionic liquid was increased from 0 to 22 wt%, and was followed by a sharp decline at higher concentrations. The initial incline between 0 and 22 wt% of ionic liquid is devoted to increased concentration of ions at the interface of the outer electrodes. As ion concentration is increased, so does the extent of the swelling at each electrode, resulting a larger volume imbalance between the two electrodes, which in turn results a larger mechanical actuation. Data suggest that above 22 wt% of ionic liquid content, a secondary layer of charge is formed at the inner side of the initial ion layer, which not only does not contribute toward actuation, it cancels some of the strain generated by the first ion layer which is at the electrode interface. Once this secondary ion layer is formed, addition of more ionic liquid worsens the electromechanical response.

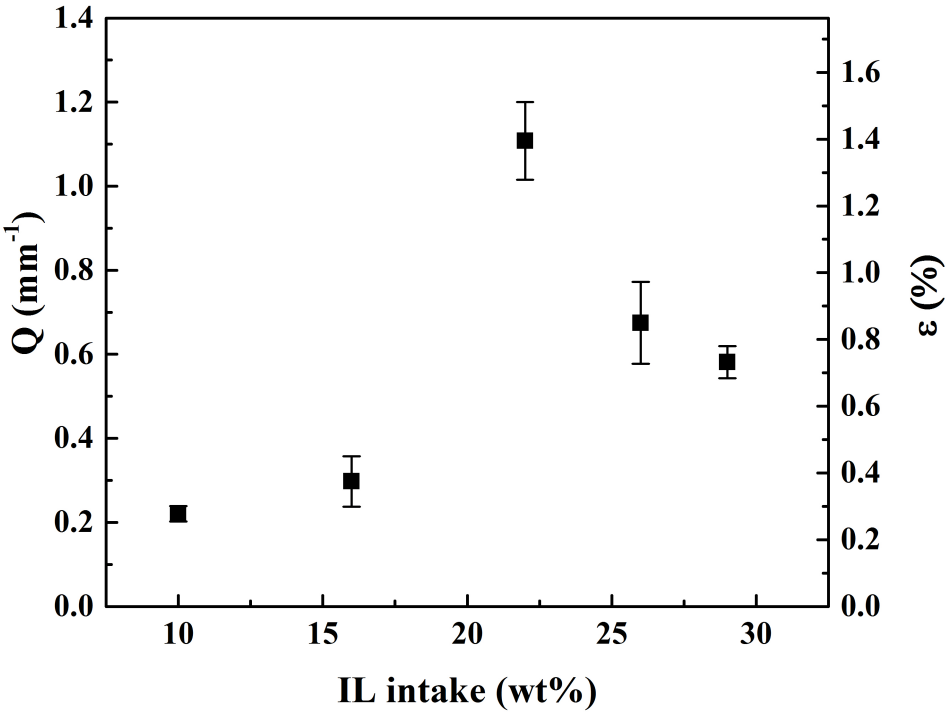

Figure 3.2: Actuation curvatures (primary y-axis) and strain (secondary y-axis) of IEAP actuators in response to a 4 V step potential is presented as a function of EMI-Tf ionic liquid concentration.

3.3.3 Electrochemical studies

To investigate how does the concentration of ionic liquid affect the frequency response of the IEAP actuators, electrical impedance of the IEAP actuators was measured as a function of frequency. Instead of a 4 V DC step voltage applied for electromechanical response studies, electrochemical studies were conducted at lower voltage of 10 mV and at a varying frequency to allow characterization over a broader frequency range, with required accuracy. It must be noted that using a higher, or different, applied potential results in different numerical values; however, trends and conclusions drawn from the experimental results would not be changed.

Presented in Figure 3.3 are the curves of Nyquist plot for the IEAP actuators. At higher frequencies (close to the origin of the x-axis) the electrochemical systems exhibited near-pure resistance behavior. Intersection of the semicircular plots with the x-axis, at high frequency

regions manifests the solution resistance (R), as presented in the equivalent electrical circuit (Figure 3.5). Solution resistance depended on the ionic conductivity of the entire system including the transportation of ions between anode and cathode. Solution resistance of samples, presented in Figure 3.3, suggests that the addition of ionic liquids results in the reduction of solution resistance, an observation that is in agreement with expected effect of any ion-rich electrolyte, such as ionic liquids. Solution resistance and ionic conductivity of IPMCs are listed in Table 3.1.

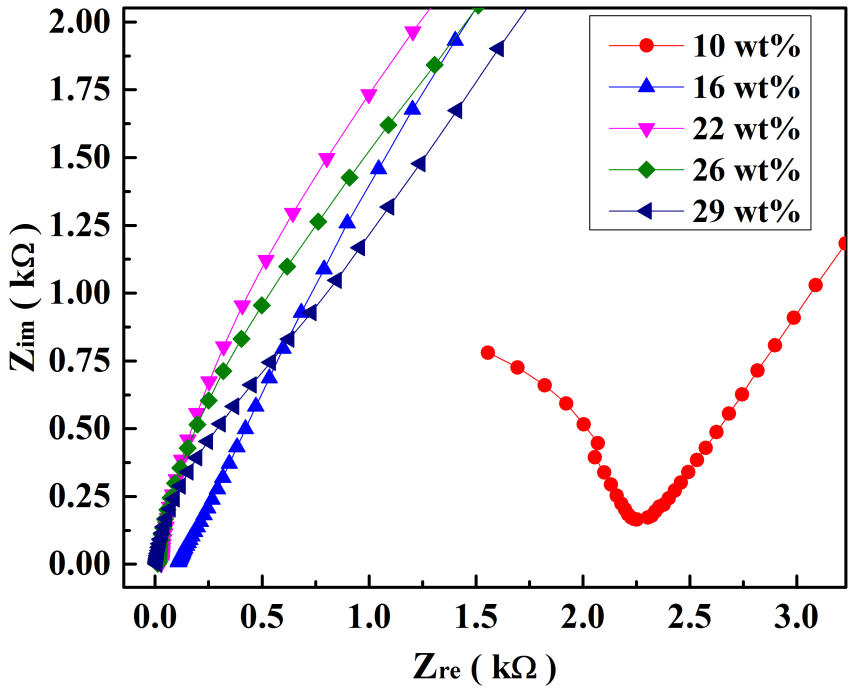

Figure 3.3: Nyquist plot of impedance magnitude of IEAP actuators containing various concentrations of ionic liquid. Solution resistance is deduced from the intersection of plots with the Z_{re} axis.

Figure 3.4 presents electrical impedance magnitude $|Z|$ and phase angle (ϕ) of IEAP actuators as a function of ionic liquid concentration. At frequencies smaller than 100 Hz the magnitude of electrical impedance is relatively independent of ionic liquid concentration; however, at faster frequencies for samples containing more than 10 $wt\%$ ionic liquid a sharp decrease in $|Z|$ is observed. It is only at very high frequencies that the magnitude of electrical impedance

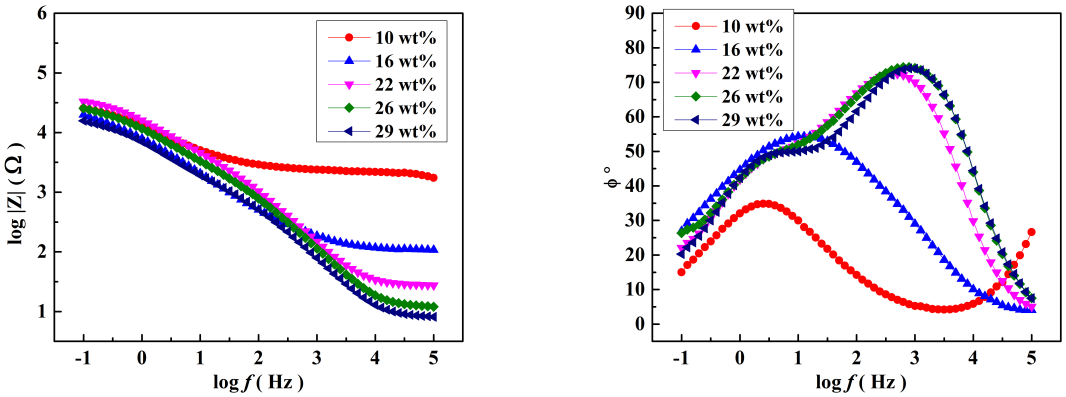

(a) (b)

Figure 3.4: (a) Impedance magnitude versus frequency; and, (b) phase angle versus frequency of IEAP actuator containing different ionic liquid concentration. At higher frequencies, impedance and phase angle exhibit higher dependency on ionic liquid concentration.

Table 3.1: Solution resistance and ionic conductivity of IPMCs containing different concentrations of ionic liquid.

IL(wt%)	$h(\mu m)$	$A(cm^2)$	$R(\Omega)$	$\sigma(S{\cdot}cm^{-1})$
10	25	1	2081.5	$1.2E-6$
16	25	1	99.5	$2.5E-5$
22	25	1	26.7	$9.4E-5$
26	25	1	11.5	$2.2E-4$
29	25	1	7.8	$3.2E-4$

exhibits full dependence on ionic liquid concentration. In general, for an IEAP actuator to deliver a large strain and force output, a large capacitance is preferred. The electrical impedance ($Z = |Z|exp(j\phi)$) is a function of the phase angle ϕ, which itself depends on frequency, and can be deduced from $tan\phi = 1/\omega R_S C_S$, where R_S and C_S are the systems net resistance and capacitance, respectively. Phase angles of $\phi = 90°$ corresponds to a pure capacitor and $\phi = 0°$ to a pure resistor (which would indicate the electrical impedance of the resistor is much larger than that of the capacitor). Since the resistive component represents the electrical loss, a ϕ approaching 90° is preferred in order to achieve a high electrical efficiency of the actuator. A larger ϕ was observed for IEAP actuators containing higher concentrations of ionic liquid. At higher frequencies, the difference in phase angles as a function of ionic liquid concentration

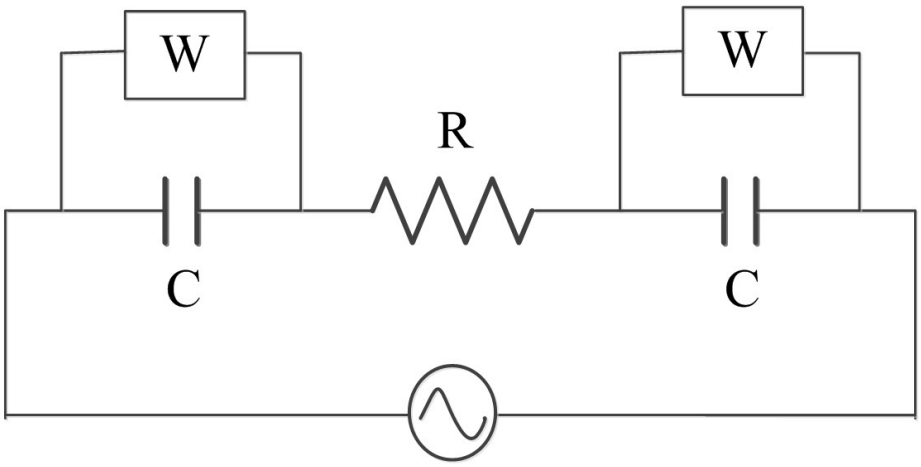

Figure 3.5: Equivalent electric circuit with Warburg element.

became more distinct, suggesting stronger capacitance-like behavior for samples with higher ionic liquid concentration.

As a result of ion accumulation at the outer electrodes an electric double layer (EDL) capacitor is formed at the interface between the ionomeric polymer membranes (Nafion in this study) and the outer electrodes. This EDL capacitor and the solution (leakage) resistance of IEAP actuators can be used to model electrochemical behavior of such systems by an equivalent electrical circuit. Previously we have shown that due to a continuous contribution to the charging and discharging current of a diffuse layer, an ideal RC circuit does not fit the experimental results well at the low frequencies [128]. Therefore, a constant phase element, Warburg element (W), is introduced by the assumption of a semi-infinite linear diffusion process at the planar electrode [37, 129, 130, 131]. Presented in Figure 3.5 is the equivalent electrical circuit where the two CW components present outer electrodeionomeric membrane interfaces and R is the solution resistance. Data from the real part of impedance was used to test the model at low frequency range. Electrochemical behavior of this system at high frequency can be fitted with a simple RC circuit; however, at lower frequencies ($f < 100$ kHz) the Warburg element is required to provide an accurate model.

As a constant phase element, the Warburg element has am explicit expression of $Z_w = (1/Y_0)(j\omega)^{-n}$, where Y_0 is a coefficient with unit of $\Omega^{-1} \cdot s^n$, ω is angular frequency ($rad \cdot s^{-1}$), and n is a unitless coefficient and equal to 0.5.

Impedance of the equivalent circuit can be expressed as:

$$Z = R + \frac{2}{j\omega C + Y_0(j\omega)^n} \tag{3.5}$$

which can be expanded by Euler's equation to:

$$Z = R + \frac{2Y_0\omega^n cos(\frac{n\pi}{2})}{Y_0^2\omega^{2n} + \omega^2C^2 + 2\omega^{n+1}CY_0 sin(\frac{n\pi}{2})} - j\frac{2[\omega C + Y_0\omega^n sin(\frac{n\pi}{2})]}{Y_0^2\omega^{2n} + \omega^2C^2 + 2\omega^{n+1}CY_0 sin(\frac{n\pi}{2})} \tag{3.6}$$

where the net real resistance of the system (R_S) can be expressed as the sum of the leakage resistance (R) and real part of the impedance (Z_{re}):

$$R_S = R + \frac{2Y_0\omega^n cos(\frac{n\pi}{2})}{Y_0^2\omega^{2n} + \omega^2C^2 + 2\omega^{n+1}CY_0 sin(\frac{n\pi}{2})} \tag{3.7}$$

which can be reorganized to:

$$\frac{1}{R_S - R} = \frac{Y_0\omega^n}{2cos(\frac{n\pi}{2})} + \frac{C^2\omega^{2-n}}{2Y_0 cos(\frac{n\pi}{2})} + \omega C tan(\frac{n\pi}{2}) \tag{3.8}$$

and for $n = 0.5$ can be rewritten as:

$$\frac{1}{R_S - R} = \frac{\sqrt{2}}{2}\frac{C^2\omega^{1.5}}{Y_0} + C\omega + \frac{\sqrt{2}}{2}Y_0\omega^{0.5} \tag{3.9}$$

and simplified to:

$$y = ax^{1.5} + bx + \frac{b^2}{2a}x^{0.5} \tag{3.10}$$

where

$$a = \frac{\sqrt{2}}{2}\frac{C^2}{Y_0}, \qquad b = C \tag{3.11}$$

Experimental data fitted with computational data are shown in Figure 3.6, confirming viability of the presented electrical equivalent circuit; and, that the net real resistance of the system decreases as concentration of ionic liquid increases.

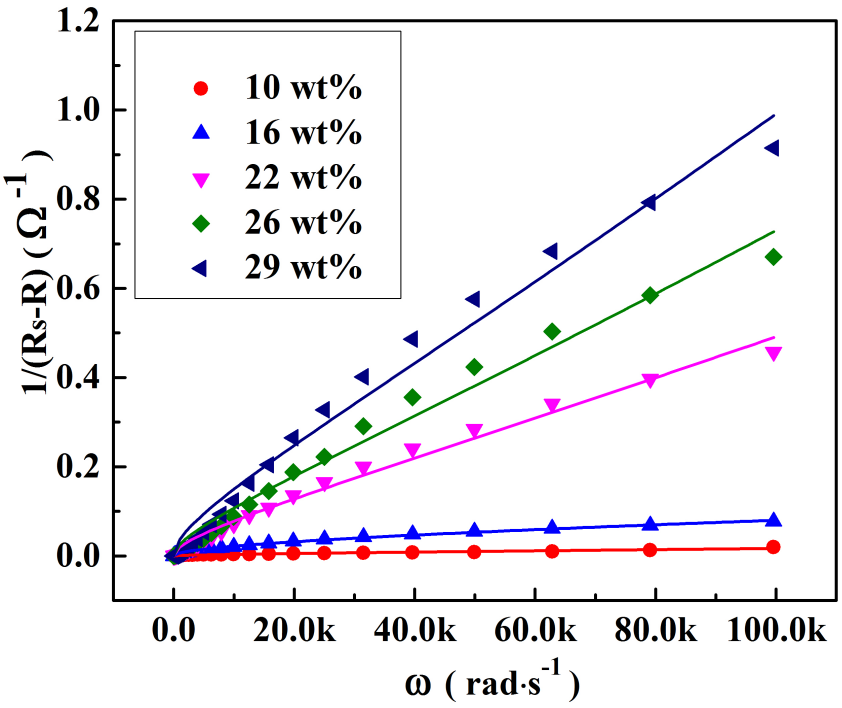

Figure 3.6: The plots of $1/(R_S - R)$ versus ω with various ionic liquid contents and their corresponding fitting lines with $y = ax^{1.5} + bx + b^2/(2a)x^{0.5}$.

3.3.4 Discussion

It was observed in this study that the internal resistance of IEAP actuators is inversely proportional to the ionic liquid concentration. Samples containing higher concentrations of ionic liquid also exhibit more capacitor-like behavior, which in turn should result in larger electromechanical response. However, electromechanical studies indicated that there exists an optimum concentration of ions at which the electromechanical response is maximized, and that optimum concentration is not the highest ion concentration. The observed drop in electromechanical response beyond optimum concentration of ions is dedicated to formation of a saturated ion layer at outer electrodes interfaces. As a result, swelling due to accumulation of ions is shifted from the edge (which is most effective in generation of electromechanical response) toward the center of the system (where its effect is no desired). Similar behavior is reported by Kwon and Ng [132] where the concentration of ionic liquid in gel electrolyte was varied. Our investigation

suggests that for applications where high charge displacement is desired (e.g. supper capacitors, sensors, etc.) increasing concentration of ionic liquids (or more generally electrolytes) may prove advantageous; however, for IEAP actuators where high electromechanical response if of interest, it is recommended to optimize the system by not passing ion concentration saturation threshold.

3.4 Conclusion

We fabricated and characterized IEAP actuators consisting of Nafion ionomeric membrane and EMI-Tf ionic liquid. We found that increasing concentration of ionic liquids in IEAP actuators results in enhanced electromechanical response, until the electrodeionomer interface is saturated with the accumulated ions. Beyond the saturation point, ion accumulation is inward, forming a secondary layer of ions, and generates undesired strain that partially cancels the strain generated by the ion layer at the interface, which is desired for actuation. In short, optimum (not maximum) concentration of ionic liquids should be incorporated in IEAP actuators to achieve maximum electromechanical response.

Acknowledgment

This material is based upon work supported in part by a funding from Health Research Initiative and Presidential Initiative for Interdisciplinary Research at Iowa State University.

CHAPTER 4. EVIDENCE OF COUNTERION MIGRATION IN IONIC POLYMER ACTUATORS VIA INVESTIGATION OF ELECTROMECHANICAL PERFORMANCE

A paper published in Sensors and Actuators B: Chemical 205 (2014): 371−376

Wangyujue Hong, Catherine Meis, James R. Heflin, Reza Montazami

Abstract

Functional ionomeric polymer membranes are the backbone of a wide range of ionic devices; the mobility of ions through the ionomeric membrane is the principle of operation of these devices. Drift and diffusion of ions through ionomeric membranes strongly depend on the ionic properties of host membrane, as well as the physical and chemical properties of the ions. It is well-established that cations and anions provided via a dopant (e.g. electrolyte or ionic liquid) are mobilized under stimulation. However, in this study, we report that in addition to ions sourced by the dopant, counterions of the ionomeric membrane are also mobilized when stimulated. In particular, we have investigated the electromechanical response of ionic electroactive polymer actuators consisting of Nafion ionomeric membranes with different counterions and have demonstrated that those with cation counterions of larger van der Waals volume exhibit stronger actuation due to motion of the larger cation counterions compared to actuators consisting of Nafion with counterion of smaller van der Waals volumes.

4.1 Introduction

Ionic properties and ion permeability of ionomeric membranes, especially those of Nafion, have been the subject of extensive and continuous studies in the past several years [56, 57, 58, 62]. The significance of such studies is mainly due to the increasing importance and ap-

plication of ionomeric membranes in ionic/electronic devices for energy generation and storage applications. The functionality of ionic devices relies on mobility of ions through the ionomeric membrane. Ion diffusion and/or drift through ion permeable polymer membranes is the most essential requirement for operation of ionic devices; such as lithium-ion polymer batteries, fuel cells, super capacitors and ionic electroactive polymer sensors and actuators, to name a few examples [133, 134, 135, 136, 12, 137, 35, 123]. For instance, diffusion of protonsthrough a proton-exchange membrane is the principle of operation of hydrogen fuel cells [138], and charging of secondary cell metal-ion polymer batteries (used in most smart phones and tablets) is solely based on the ion drift through a polymer electrolyte membrane when an external electric voltage is applied [139]. Better understanding of ion mobility through ionomeric membranes will provide means for development of electric/ionic devices with higher performance and efficiency.

Although ion mobility, both diffusion and drift, is well utilized in commercial devices, we still lack a complete understanding of this phenomenon. It is not yet clear to the scientific community the detailed process of how ions move through the ionomeric membranes and how this process can be manipulated. The general understanding is that Nafion is a proton-exchange membrane; thus, H^+ can easily diffuse through it. Diffusion of H^+ through Nafion is well studied and applied in many conceptual applications such as fuel cells [140]. There is no doubt about H^+ permeability of Nafion; however, when subjected to an electric voltage Nafion is also permeable to drift of other ions [69, 3, 141, 37, 38, 39]. Our prior work on ionic electroactive polymer (IEAP) actuators confirmed that, when doped with ionic liquid, Nafion is permeable to both cations and anions of the ionic liquid; and, the electromechanical response of IEAP actuators is directly proportional to concentration of the ions from dopant [13, 40]. The functionality of IEAP actuators is solely the result of motion of ions through the ionomeric membrane. The common understanding is that cations and anions provided by the doping of the ionomeric membrane with electrolyte are responsible for the electromechanical response of IEAP actuators. Upon application of an electric voltage, cations and anions are mobilized and move toward electrodes of opposite charge. Since cations and anions have different van der Waals volumes, their accumulation at the cathode and anode results in a volume imbalance in

the system; and thus, a mechanical deformation [4]; this phenomena is schematically presented in Figure 4.1.

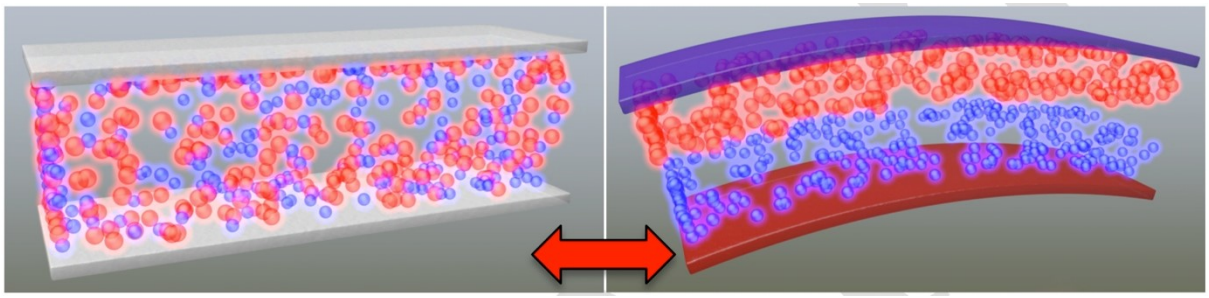

Figure 4.1: Schematics of uncharged and charged doped 3-layer ionic electroactive polymer actuator. Red and blue spheres illustrate cations and anions, respectively. (Not to scale). (For interpretation of the references to color in this figure legend, the reader is referred to the web version of this article.)

In this study we have altered the functionality of ionomeric membranes by exchanging the proton counterion of Nafion with larger cations; and have utilized the electromechanical response of IEAP actuators, consisting of Nafion with different counterions and dopants, as a means to study the mobility of ions through Nafion ionomeric membranes and, more specifically, investigate mobility of counterions of Nafion. Ion-exchange process is schematically demonstrated in Figure 4.2. This work contributes to the knowledge of electric and ionic properties of ionic functional materials and their applications in electric and ionic devices such as sensors, actuators, fuel cells and metal-ion polymer batteries.

4.2 Experimental

4.2.1 Materials

Commercially-available Nafion membrane of 90 μm thickness (Ion Power, Inc.) was used as the base ionomeric membrane. 1-Ethyl-3-methylimidazolium trifluoromethanesulfonate (EMI-Tf, molecular formula: $C_7H_{11}F_3N_2O_3S$), triethylsulfonium bis(trifluoromethylsulfonyl)imide (TES-TFSI, molecular formula: $C_8H_{15}F_6NO_4S_3$) and 1-butyl-1-methylpyrrolidinium bis (trifluoromethylsulfonyl)imide (BMP-TFSI, molecular formula: $C_{11}H_{20}F_6N_2O_4S_2$) ionic liquids,

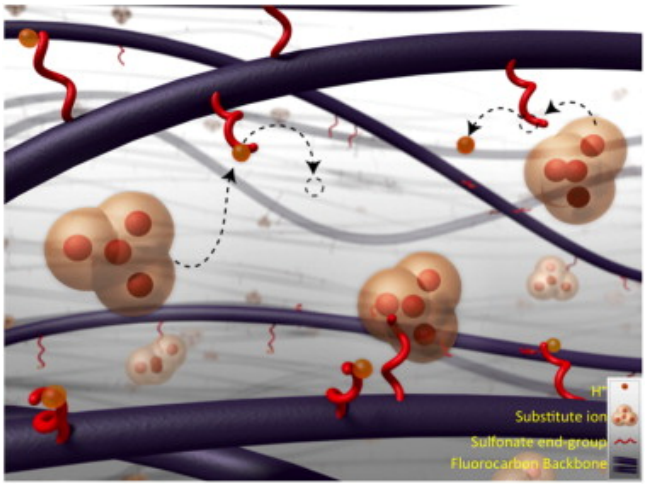

Figure 4.2: Schematic presentation of ion-exchange process in Nafion. Proton counterions are substitute by other cations.

and 1-ethyl-3-methylimidazolium chloride (EMI-Cl), zinc chloride and sodium chloride salts were purchased from Sigma Aldrich and used without further modification. Transferable 24 K gold leafs of 50 nm thickness were purchased from L.A. Gold Leaf and cut to desired size before using.

4.2.2 Methods

4.2.2.1 Ion-exchange

Salt solutions were prepared at 0.5 M concentration by dissolving the proper amount of the desired salt in deionized water. The solution was then stirred overnight. Ionic membranes of the desired size (2.5 $\times$ 12 cm^2) were cut out of a sheet of 90 μm thick Nafion and boiled in diluted (1 M) sulfuric acid solution at 100 °C for 120 min. Water was added frequently to keep the volume of the mixture constant and to compensate for the evaporated water. The samples were then boiled in deionized water at 100 °C for 120 min, then dried using a wipe and cut into smaller pieces (2.5 $\times$ 6 cm^2). Cut samples were then placed in ample amount of saturated salt solution in container with tightened caps, and heated to 80 °C for two days. The temperature was then reduced to 60 °C for another eight days to assure ion-exchange between the Nafion and salt solution. Considering high sensitivity of Nafion-ionic liquid systems to humidity [115, 114],

samples were then placed under vacuum (~ -100 kPa) and heated to 115 °C for three days to dehydrate and were kept in desiccator or used immediately.

4.2.2.2 Doping and assembly

Samples were then cut into smaller pieces (2.5×2.5 cm^2), weighed and soaked in the desired ionic liquid to uptake ~40 wt% of their dry weight. Equation 4.1 was used to calculate the electrolyte uptake, where $W_e(\%)$ is the weight-percent of the electrolyte; and, W_d and W_f are the weights of dry and doped samples, respectively.

$$W_e(\%) = \frac{W_f - W_d}{W_f} \times 100 \tag{4.1}$$

Gold leaves were hot-pressed at 95 °C, under 4500 N for 25 s on both sides of the ionic liquid-doped samples to fabricate ionic electroactive actuators.

4.2.2.3 Electromechanical characterization

Actuators were cut into approximately 1.5×15 mm^2 pieces and tested under application of a 4 V applied potential. Electromechanical response of the actuators was monitored and recorded using a charge-coupled device (CCD) video camera, mounted to an in-house fabricated micro-probe station, at 30 frames per second. Individual frames were then analyzed to measure the radius of curvature (r) as a function of time and to calculate curvature (Q) from Equation 4.2.

$$Q(t) = \frac{1}{r(t)} \tag{4.2}$$

For actuators with small tip displacement, strain can be calculated from free length, thickness and tip displacement of the actuator [142]; however, for actuators with more extensive bending, the radius of curvature must be taken into account. Strain (%) was then calculated based on the thickness (h) and radius of curvature of each actuator, using Equation 4.7, which is derived from the ratio of the change in the free length of actuator between center and surface of the actuator, to the initial free length. Schematic presented in Figure 4.3 and following calculations demonstrate deriving of Equation 4.7; where L_c is actuator's length at the center (which is equal to actuator's free length), L_o is actuator's length at the expanded surface, r_c

and r_o are radius to the center and expanded surface of actuator, respectively; and, α is the angle between the mounted and free end of the actuator.

$$L_c = \alpha r_c \tag{4.3}$$

$$L_o = \alpha r_o = \alpha(r_c + h/2) \tag{4.4}$$

$$\varepsilon\% = \frac{L_o - L_c}{L_c} \times 100 \tag{4.5}$$

substituting Equation 4.3 and 4.4 in Equation 4.5, we will get:

$$\varepsilon\% = \frac{\alpha(r_c + h/2) - \alpha r_c}{\alpha r_c} \times 100 \tag{4.6}$$

simplifying Equation 4.6 and including time dependency, we will have:

$$\varepsilon\%(t) = \frac{h}{2r_c(t)} \times 100 \tag{4.7}$$

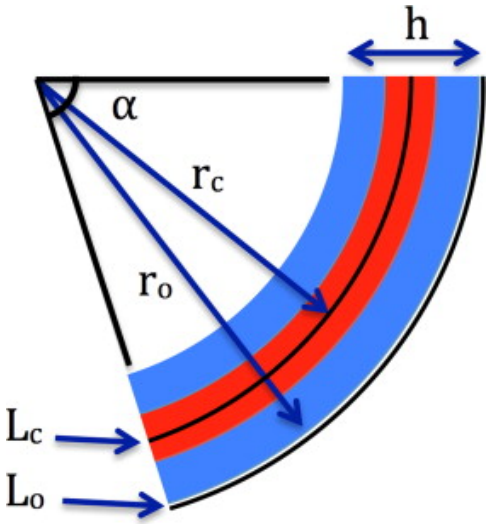

Figure 4.3: Schematic representation of ionic electroactive polymer actuator with geometrical components used in calculation of strain. (Not to scale).

To obtain strain data, each set of experiments was repeated at least three times to confirm reproducibility. Where appropriate, data were averaged; otherwise the most common behavior was used.

4.3 Results and Discussion

4.3.1 Van der Waals radius of counterions

Four sets of samples were fabricated consisting of Nafion films with different counterions, doped with EMI-Tf ionic liquid. Nafion in its proton form (H^+ counterion), and Nafion ion-exchanged with Zn^+, Na^+ and EMI^+ were studied for the cationic portion of their electromechanical response. Table 4.1 summarizes van der Waals properties of the investigated counterions.

Table 4.1: Van der Waals properties of the counterions of Nafion membrane and anions and cations of ionic liquid dopants.

Counter-ion	**Van der Waals radius (pm)**	**Van der Waals volume ($\AA$)**
H^+	120.0	7.2
Zn^+	139.0	11.2
Na^+	227.0	48.9
EMI^+	294.6	107.1
TES^+	316.0	132.2
BMP^+	339.7	164.2
Tf^-	275.5	87.6
$TFSI^-$	337.8	161.4

The van der Waals volumes of the atomic ions were calculated directly from the van der Waals radius of each atomic ion; the van der Waals volume of the EMI molecular ion was calculated based on the number of bonds, aromatic and nonaromatic rings, as described by Zhao et al. [143].

4.3.1.1 Influence of counterions on cationic electromechanical response

Presented in Figure 4.4 is the magnitude of the electromechanical response of the actuators as a function of the van der Waals volume of the counterions. The actuator consisting of Nafion with H^+ counterion exhibits significantly smaller cationic strain compare to the actuators consisting of Nafion with larger counterions. The increase in the magnitude of cationic strain is more significant between atomic counterions and the molecular counterion. This is most probably due to the complex 3-dimensional structure of EMI^+ multi-atom ion compare to

the simpler spherical structure of single-atom ions. Interestingly, actuators containing different counterions reached the steady state at approximately the same time (93 ± 2 s), implying that the ions move at approximately the same speed and that the ion mobility is drift dominated rather than diffusion dominated. Back relaxation was not observed in any one of the systems.

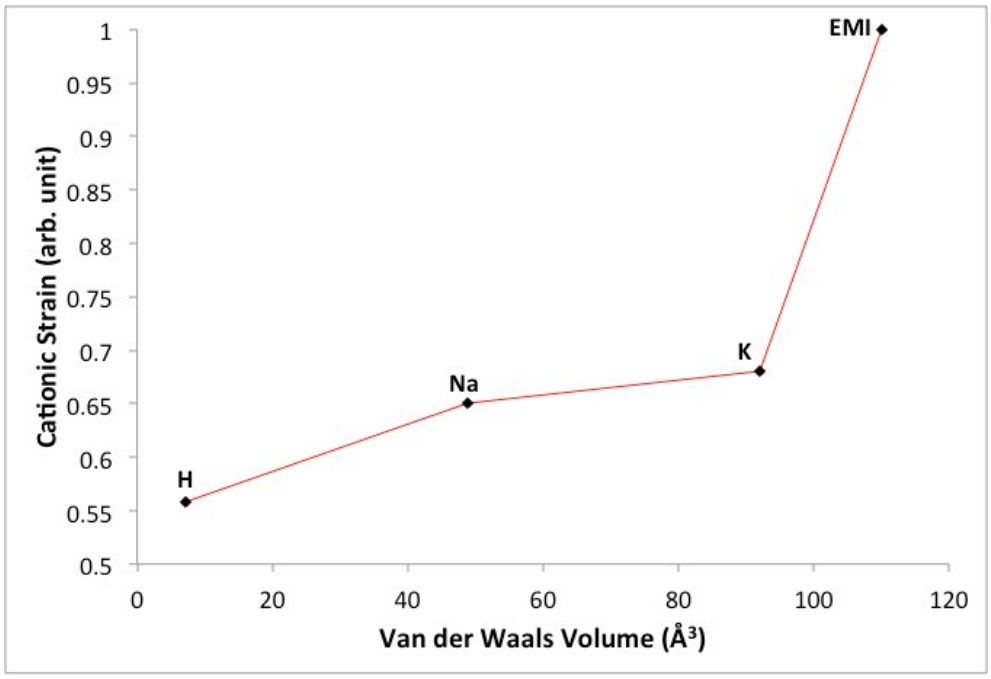

Figure 4.4: Magnitude (arbitrary units) of maximum cationic strain of IEAP actuators consisting of Nafion with different counterions as a function of van der Waals volume of counterions. Actuators consisting of Nafion with larger counterions exhibit enhanced cationic strain.

4.3.2 Electromechanical response as a function of dopant

We further investigated the influence of the counterions on electromechanical response by comparing the full (cationic and anionic) electromechanical response of IEAP actuators consisting of Nafion with H^+ and EMI^+ counter-ions (the two extreme cases in this study), doped with three different types of ionic liquids. The samples investigated in this section are named by the following format: $(Counterion \backslash Cation - Anion)$ where cation and anion are those from the ionic liquid.

As we described previously [13], the cationic and anionic strains are the result of the out-of-phase motion of cations and anions in Nafion. For instance, in the case of IEAP actuators

doped with EMI-Tf ionic liquid, the drift velocity of EMI^+ cations is faster than that of Tf^- anions. As a result, when the voltage is applied, a bending toward the anode is observed first, that is due to the fast accumulation of cations at the cathode, followed by a dominating anionic motion that is due to accumulation of anions at the anode. In the case of EMI-Tf ionic liquid, both cationic and anionic strains are significant and distinguishable, especially over long path-lengths (i.e. thick Nafion); and, anionic motion is dominant due to the higher effectiveness of anions (or anionic clusters)[125] in generating strain compare to cations. This behavior may be different or even reversed, depending on the physical and electrochemical properties of the electrolyte used in doping of the Nafion.

As presented in Figure 4.5, IEAP actuators consisting of Nafion with H^+ and EMI^+ counterions, doped with EMI-Tf ionic liquid exhibit both cationic (in the plots showed as positive strain (%)) and anionic (in the plots showed as negative strain (%)) strain, with the anionic strain ultimately dominating the response. An interesting observation is that when the H^+ counterions are exchanged with EMI^+, the entire response curve of the IEAP actuator is almost uniformly shifted toward cationic strain, suggesting contribution of the EMI^+ counterions toward cationic strain.

Similar behavior was observed when other ionic liquids were used as dopants. As shown in Figure 4.6 and 4.7, IEAP actuators consisting of TES-TFSI and BMP-TFSI in Nafion with H^+ counterion have dominating anionic strain, which prevents observation of any cationic strain even at the beginning of actuation, suggesting that unlike Tf^- anions in EMI-Tf, $TFSI^-$ anions in TES-TFSI and BMP-TFSI are quickly mobilized upon application of the potential difference. Hence, TES^+ and BMP^+ cations are not allowed the time required to generate a temporary dominating cationic strain, or both types of ions are mobilized simultaneously yet the effectiveness of the $TFSI^-$ is dominant.

In both cases, when H^+ are exchanged with EMI^+ ions, the overall response is shifted toward cationic strain. In the case of the EMI\TES-TFSI IEAP actuator, a small cationic motion is observed in the first tens of seconds, yet quickly canceled by the anionic strain. However, the overall electromechanical response exhibits a shift toward cationic strain, again suggesting the contribution of the EMI^+ counterions to the net strain. In the case of the EMI\BMP-TFSI

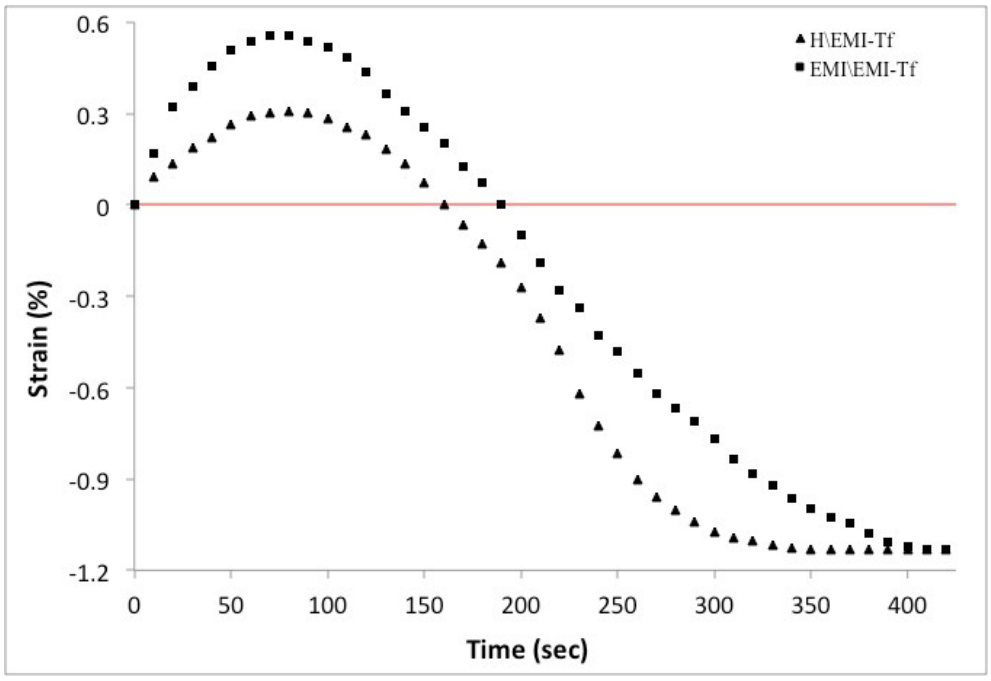

Figure 4.5: Electromechanical responses of IEAP actuators doped with EMI-Tf ionic liquid consisting of Nafion membranes with H^+ and EMI^+ counterions. Cationic strain is enhanced with larger counterion.

IEAP actuator the contribution of EMI^+ is more significant. The electromechanical response is fully reversed from an anionic-only to a cationic-only strain, suggesting significant influence and contribution of EMI^+ toward the electromechanical response of the IEAP actuators or, in more general terms, influence on the ionic properties of Nafion ionomeric membranes.

4.3.3 Discussion

Our experiments and observations suggest that the counterions of the ionomeric membrane, Nafion in this case, are mobilized upon exposure to an external electric voltage and thus have significant influence on the ionic response of the membrane and do contribute to the electromechanical response of the IEAP actuators. Considering the standard cluster-network model to explain the morphology of Nafion (see Figure 4.8), two possible hypotheses may be developed to explain the contribution of counterions to ion permeability of Nafion:

A) Counterions with larger van der Waals volume expand the narrow channels between the interconnected clusters. These narrow channels in Nafion with H^+ counterions have an

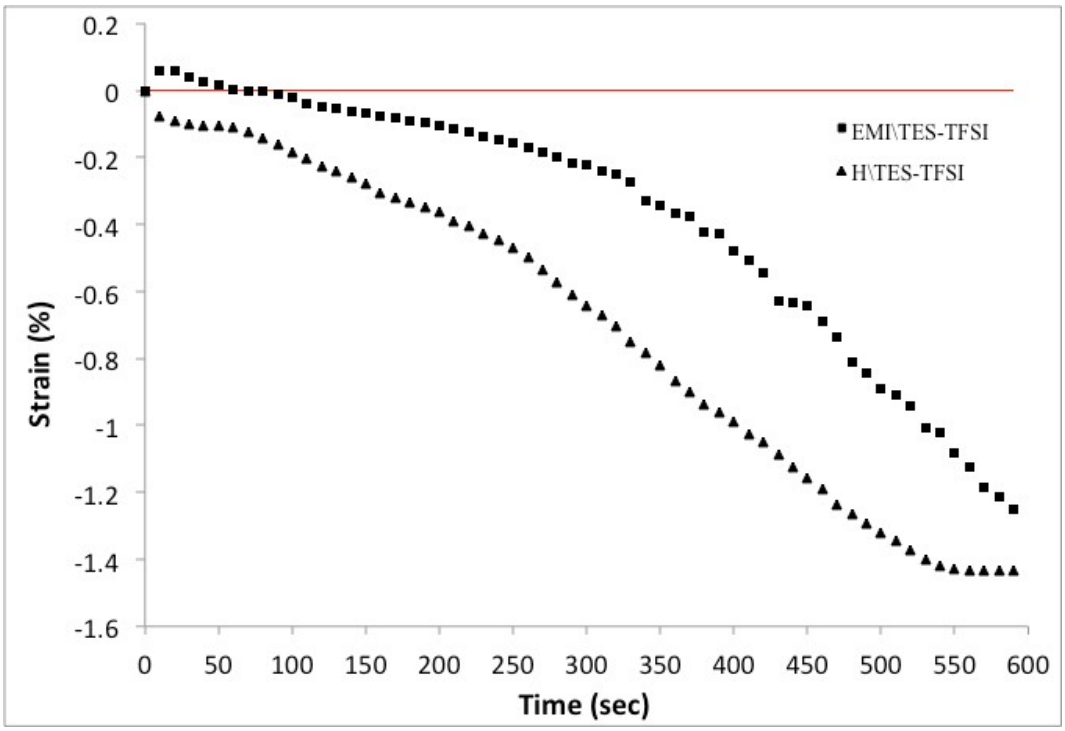

Figure 4.6: Electromechanical responses of IEAP actuators doped with TES-TFSI ionic liquid consisting of Nafion membranes with H^+ and EMI^+ counterions. The response is shifted toward cationic strain with larger counterion.

approximate diameter of 10 Å, which is considerably larger than the van der Waals diameter of H^+ (2.4 Å, see Table 4.1). When larger cations (e.g. EMI^+) are introduced to the network, ionic interactions between the cations and sulfonate end-groups force the cations into the channels, and to compensate for repulsion between neighboring cations the channels expand; in presence of an electric voltage, the expanded channels allow motion of cations (EMI^+ in this case) through the network. These expanded channels provide means for higher mobility of the ions throughout the Nafion membrane.

B) Counterions in Nafion are always mobile and contribute toward cationic strain; yet, due to the small van der Waals volume of H^+, this contribution is less significant. When a larger cation is introduced, the contribution toward cationic strain is more significant and thus observable.

Although it is very difficult to explain and construct an accurate model for mobility of ions through Nafion, our experimental results and observations suggest that while both hypotheses

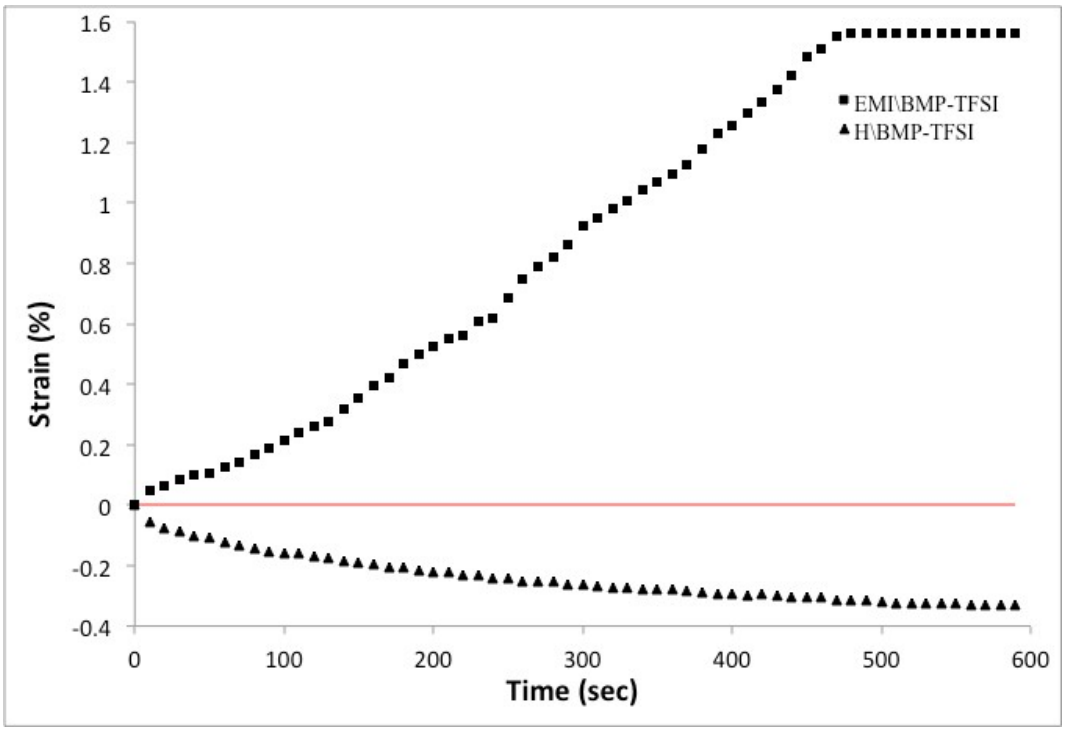

Figure 4.7: Electromechanical responses of IEAP actuators doped with BMP-TFSI ionic liquid consisting of Nafion membranes with H^+ and EMI^+ counterions. The electromechanical response is completely reversed from fully anionic to fully cationic with larger counterion.

above may be, to some extent, correct, hypothesis B explains the behavior of IEAP actuators more consistently and is responsible for the observation of an enhanced cationic strain in the presence of larger counterions.

When an electric voltage is applied, it breaks the electrostatic bonds between the counterions and sulfonate end-groups, mobilizing the counterions. Along with the cations from the doping electrolyte, the mobilized counterions (red dots in Figure 4.8) are attracted to the cathode while the anions are attracted to the anode. Depending on the van der Waals volume of the counterions, their contribution toward cationic strain varies. In the case of H^+ counterions, the contribution is minimal due to the small van der Waals volume, while it is more significant in case of larger counterions such as EMI^+.

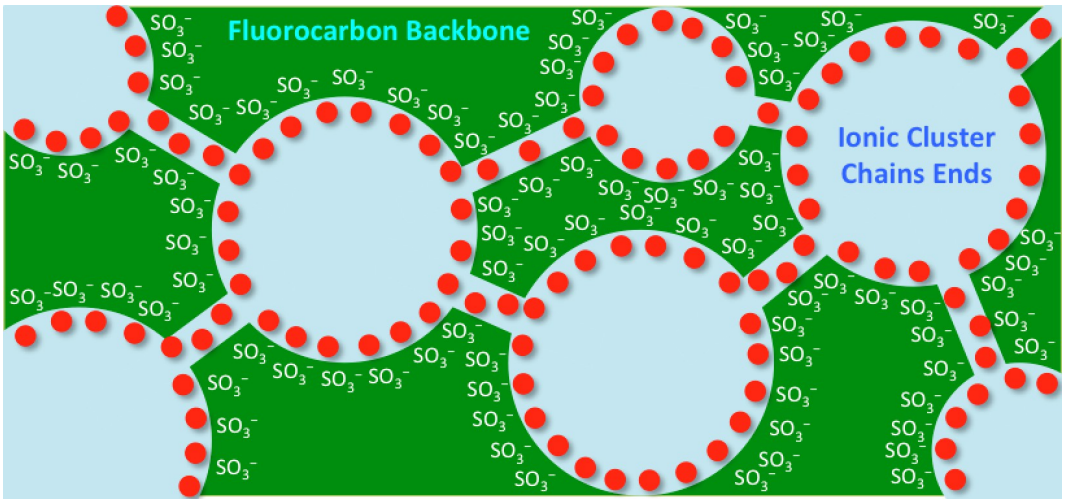

Figure 4.8: Schematic cluster-network morphology of Nafion. It is anticipated that counterions (red dots) are mobilized when exposed to an external electric voltage. (For interpretation of the references to color in this figure legend, the reader is referred to the web version of this article.)

4.4 Conclusion

We investigated ion mobility through Nafion ionomeric membrane via the electromechanical response of IEAP actuators fabricated using Nafion with a variety of counterions and ionic liquid dopants. It was observed that exchange of the H^+ counterion of Nafion with a cation of larger van der Waals volume results in the generation of enhanced cationic strain. Experiments were performed with four types of counterions and three different types of ionic liquids as dopants, and in all cases the enhancement was observed. The results of this study suggest that in the presence of an electric voltage, in addition to cations and anions from the dopant that drift through the Nafion, the counterions of Nafion are also mobilized and drift through the interconnected channels of the polymeric backbone structure and accumulate at the cathode to contribute toward cationic strain. Further investigations are expected to contribute toward more efficient actuators, sensors, metal-ion polymer batteries, and other ionic devices.

Acknowledgements

This material is based upon work supported in part by a funding from Health Research Initiative and Presidential Initiative for Interdisciplinary Research at Iowa State University;

and the US Army Research Office under Grant No. W911NF-07-1-0452 Ionic Liquids in Electro-Active Devices (ILEAD) MURI.

CHAPTER 5. SOFT IONIC ELECTROACTIVE ACTUATORS WITH TUNABLE NON-LINAR LIMB-LIKE DEFORMATION

A paper to be submitted to the journal of Applied Materials and Interfaces

Wangyujue Hong, Abdallah Almomani, Yufen Chen, Reza Montazami

Abstract

Although soft materials are well studied for their electromechanical behavior in soft actuators and soft-robotic applications, practical development of such applications has been hindered by the attributes of the soft materials. Electromechanical soft actuators, based on design, can exhibit linear or circular deformation. For biomimetic soft-robotic applications linear deformation is minuscule and circular motion is unnatural. Here we demonstrate that manipulation of ionic motion through means of structural design can realize intrinsic limb-like motion in soft actuators. The incorporation of conjugated polymer, PEDOT:PSS patterns in the structure of soft actuators allows control over ion permeability of the soft actuator as a whole while alleviating compromise of electric conductivity. We experimentally and theoretically demonstrated soft actuators that are capable to bend in sharp angles (90° and beyond) and exhibit limb-like deformation.

5.1 Introduction

The field of robotics is currently dominated by "hard robots" consisting of hard materials, mainly metallic or composite structures, paired with either (or both) ceramic actuators or electric motors as drive trains. Although hard robots sometimes have biomimetic design and limb-like structures similar to those in animals (e.g. "Big Dog" constructed by Boston Robotics[144]), very often, hard robots utilize wheels and rotary motors for motion which dis-

tance them from biomimetic design. Biomimetic robotics and microrobotics is an important and emerging technology with potentials in military, intelligence healthcare and biomedical applications. Hard robotics technology fails to provide practical means for construction of biomimetic microrobotics.

Although MEMS have undergone an enormous technological leap in the past decade, it is still not feasible from a practical point-of-view to manufacture biomimetic microrobotics through hard robotic approach. Fabrication and integration of motors, actuators, moving parts and the power sources required to autonomously run these systems is an immense challenge.

Soft actuators have enabled emergence of soft robotics capable of locomotion and manipulation, while exhibiting biomimetic physical and mechanical attributes similar to those of Mollusca[145]. According to the robotic community "soft robots" are defined as: a) robots made of soft materials, or b) robots made of multiple rigid components that operated to demonstrate soft-robot-like behavior.

The ultimate advantages of soft actuators made of soft materials are that 1) they can easily conform to curvilinear structures, similar to biological muscles; and 2) actuation is an intrinsic property of the actuator; thus, design and fabrication of micro scale systems is practical.

Electroactive polymer actuators, and in particular ionic electroactive polymer (IEAP) actuators, have attracted enormous interest and attention from the soft-robotic community and have been subject to extensive studies in the past several years. Depending on design, IEAP actuators can exhibit either linear or circular actuation. Electromechanical response of linear IEAP actuators is minuscule and not adequate to be utilized for locomotion; circular deformation, however, is substantial. IEAP actuators are comprised of an ionomeric membrane at the core, covered with conductive network composite (CNC) layers and metal electrodes on each side to enhance ionic mobility and electric conductivity. IEAP actuators are doped with electrolytes, typically ionic liquids, to provide an ion-rich environment that is required for enhanced actuation. Performance and attribution of IEAP actuators depend on many factors including thickness and chemical structure of the ionomeric membrane[16]; thickness, density, porosity and electric conductivity of CNC layers[13, 40, 38, 4, 39]; thickness and electric conductivity of metal electrodes[41]; and type, mobility and prevalence of mobile ions[16, 38, 17, 37, 15].

The main disadvantage of bending IEAP actuators, considering soft robotic applications, is the circular actuation that is distinctly different from most of biological systems. Although many muscles in vertebrates and invertebrates have circular or sinusoidal motions (e.g. tongue, abdominal muscles, etc.), they are not utilized in locomotion of animals or insects. Muscles involved in locomotion of these classes of species are very often integrated with skeleton or exoskeleton structures to form limbs capable of motions required for locomotion of the species. Mimicking a Venus flytrap[146], flapping wings[147, 148], artificial muscles[149, 123], and soft actuator propelled fish robot[150, 151] are some great examples that utilize circular bending soft actuators. On the other hand; some other applications like microgrippers[152, 153], and miniaturized five fingered robotic[154], would have been more utilized with a limb-like motion rather than a circular motion. To achieve the limb-like motion, some studies used segments of IEAP actuators to be controlled individually in different direction[155, 156]. A snake-like swimming robot is an example of a soft robot that used three individually controlled segments of soft actuators[157].

In this study, IEAP actuators capable of demonstrating angular deformation are presented, mimicking the limb-like motion in biological systems. The limb-like motion is achieved without utilization of skeleton-like structures and it is purely intrinsic. This achievement is realized by varying ion permeability of the CNC layers via patterns that can be manipulated by means of design. Poly(3,4-ethylenedioxythiophene)-poly(styrenesulfonate) (PEDOT:PSS) were employed to fabricate the CNC layers with patterns due to its higher conductivity, low cost and simple deposition techniques required in the manufacture process of IEAP actuators[158, 159]. It was used widely used as outer electrodes to develop some all-organic transducers[160, 161, 162, 163, 164, 165, 166]. As fully explored in our previous work, actuator with similar constitution initially bends toward the anode and as the time progresses, it reverses the actuation direction and bends toward the cathode[13, 40, 38, 4, 39]. The first motion towards anode, which is named as cationic response, is resulted by the quicker response of cations, while the second motion during which the actuator starts to bend towards the cathode, is named as anionic response. The slower anionic response is generated by motion of anions or ion clusters with net negative charge[125]. The angular bending reported in this study is dependent on

the patterns of CNC layers. Moreover, due to its morphological asymmetry in some sets of specimens, the bending performance revealed in cationic and anionic response were also different, even for the same actuator. Electrochemical analysis was performed on the specimens with/without casted PEDOT:PSS layer, in order to explore its contribution to the ion transport and storage of ionic liquids in the system. Additionally, finite element modeling (FEM) was used to simulate the inhomogeneous mechanical deformation of actuators containing different patterns.

5.2 Experimental

5.2.1 Materials

Commercially available Nafion membrane of 25 μm thickness (Ion Power, Inc., DE, USA) was used as the ionomeric membrane; 1-ethyl-3- methylimidazolium trifluoromethanesulfonate (EMI-Tf, molecular formula: $C_7H_{11}F_3N_2O_3S$) ionic liquid (Sigma Aldrich, MO, USA) was used as received; poly(3,4-ethylenedioxythiophene)-poly(styrenesulfonate) (PEDOT:PSS) (3.0 - 4.0% in H_2O, high-conductivity grade) (Sigma Aldrich, MO, USA) was diluted by mixing with DI water at 1:1 ratio and was used for fabrication of conductive polymer patterns. Gold leaf of 50 nm thickness (24K, transfer, LA Gold Leaf, CA, USA) was used as the outer electrodes.

5.2.2 Sample fabrication

Nafion, in its acidic form, was first cut and soaked in EMI-Tf at 80 °C for 30 minutes to intake 23 wt% of ionic liquid. Ionic liquid content was measured as the weight percentage (wt%) of the dry weight of the membrane, and calculated from Equation 5.1.

$$W_e(\%) = \frac{W_f - W_d}{W_f} \times 100 \tag{5.1}$$

where $W_e(\%)$ is the weight percent of the electrolyte; and W_d and W_f are the weights of dry and doped samples, respectively[15]. Excess IL was wiped off using weighted paper and the doped Nafion membrane was then placed between two sheets of paper overnight to flatten. Diluted PEDOT:PSS aqueous solution was drop-casted on the Nafion membrane over a vinyl mask of three desired patterns at 0.56μL/mm^2. Schematic representation of each pattern is

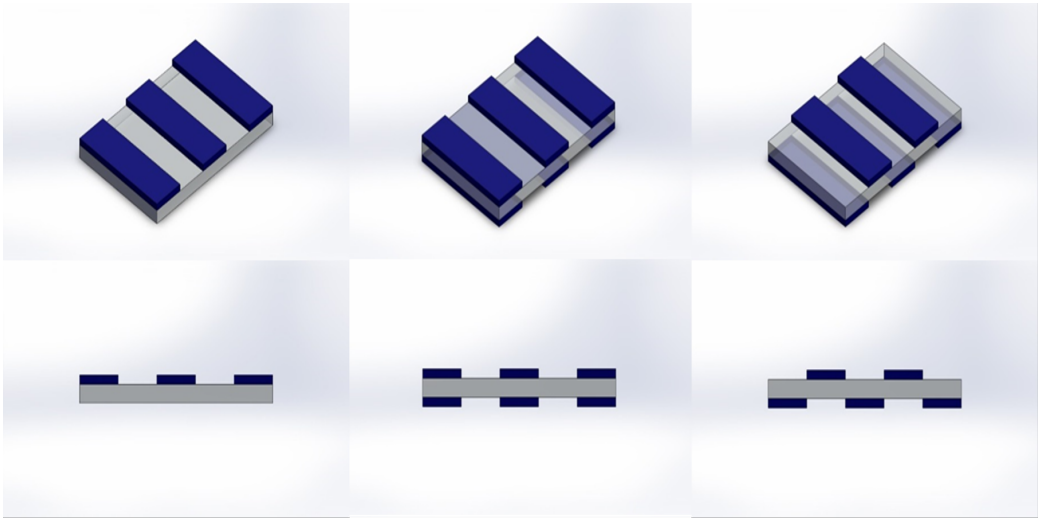

(a) (b) (c)

Figure 5.1: 3D schematic representation of the Nafion with three different PEDOT:PSS strip patterns before gold leaf electrodes hot-pressed. From left to right are the samples with one side (1S) (a), two-side symmetric (2SS) (b), and two-side asymmetric (2SA) (c) patterns, respectively. Top line is the isotropic view, and the bottom line is the corresponding side view. The 3D sketches are not to scale.

shown in Figure 5.1. The space between two strips and the width of each strip are both 3 mm. Drop casted patterns were dried on a hot plate at 40 °C for 48 hours to allow for complete solvent (DI water) evaporation. The coated samples were then dried in vacuum at -60 mmHg at room temperature for 24 hours to further dehydrate the samples. Gold leaf electrodes were then hot-pressed at 95 °C under 1000 lb_f for 40 seconds on both sides of the membrane to form an IEAP actuator.

5.2.3 Sample nomenclature

Sample nomenclature is concluded and shown in Table 5.1.

5.2.4 Electrochemical characterizations

Impedance spectroscopy and current flow were measured and recorded using a VersaSTAT-4 potentiostat (Princeton Applied Research, TN, USA) in two-electrode mode. The impedance spectroscopy studies were carried out at frequencies between $1.0E5$ Hz and $1.0E-1$ Hz, and a

Table 5.1: The abbreviation and its definition of each sample used in this work.

Name	Definition
1S[a]	Pattern deposited on one side, Figure 5.1(a)
2SS[a]	Symmetric patterns on both sides, Figure 5.1(b)
2SA[a]	Asymmetric patterns on both sides, Figure 5.1(c)
2SA2[a]	2SA sample with 2 strip-patterned side attached to anode
2SA3[a]	2SA sample with 3 strip-patterned side attached to anode
BNafion[b, c]	Bare Nafion doped with IL
Nafion/2s-PEDOT:PSS[b, c]	PEDOT:PSS drop-casted on both sides regardless of any patterns
Nafion/1s-PEDOT:PSS[b,c]	PEDOT:PSS drop-casted on one side regardless of any patterns, and connected to counter electrode
1s-PEDOT:PSS/Nafion[c]	PEDOT:PSS drop-casted on one side regardless of any patterns, and connected to working electrode
Nafion/1s-PEDOT:PSS/Au[d]	PEDOT:PSS drop-casted on one side regardless of any patterns, with gold leaf hot-pressed on both sides

[a] In electromechanical characterizations; [b] in impedance spectroscopy measurements; [c] in charging and discharging currents collection; [d] in morphological characterizations.

potential difference (ΔV) of 10 mV. Current flow was studied as a function of $+/-4$ V step functions, each over a 600 second interval.

5.2.5 Electromechanical Characterizations

Actuators of 1×15 mm^2 dimension were cut perpendicularly to the longitudinal direction of the PEDOT:PSS strips. A 4 V step function was applied across the actuator and the electromechanical response was monitored and recorded using a charge-coupled device (CCD) video camera, mounted to an in-house constructed microprobe station, at the rate of 30 frames per second.

5.2.6 Morphological and mechanical characterizations

Surface analysis was conducted by scanning electron microscopy (SEM) (Joel. JCM-6000 NeoScope, IL, USA) for the characterizations of morphology such as the film thickness and the layer adhesion. The SEM image of the crossection of specimen Nafion/1s-PEDOT:PSS/Au is shown in Figure 5.2, indicating a tight layer adhesion between Nafion and PEDOT:PSS layer after the hot-press, with no obvious separation in between.

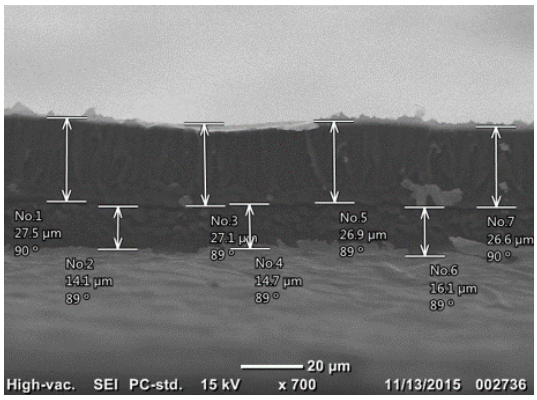

Figure 5.2: SEM image of the crossection of specimen Nafion/1s-PEDOT:PSS/Au, indicating a tight layer adhesion between each layer.

The elastic modulus of each component in IEAP actuator was performed on a Dynamic Mechanical Analyzer (DMA-1, Mettler Toledo, OH, USA), loaded with tension clamp at static modes. More information is included in Appendix A.

5.2.7 Finite element modeling

The electromechanical response of IEAP actuators with different patterns was modeled by ABAQUES finite element code. The purpose of the simulation was to study the effect of various patterns on the actuation performance, and compare the experimental and numerical results. It was assumed that the accumulation/depletion of excess charges at the electrode is equivalent to a thermal bimorph in mechanism. Detailed simulation procedures are included in Appendix A.

5.3 Results

5.3.1 Equivalent circuit modeling

To investigate how the presence of PEDOT:PSS layers affect the frequency response of the IEAP actuators, electrical impedance was studied as a function of frequency. Instead of a 4 V DC step voltage applied for electromechanical response studies, electrochemical studies were conducted at lower voltage of 10 mV and at a varying frequency to allow characterization over a broader frequency range, with required accuracy.

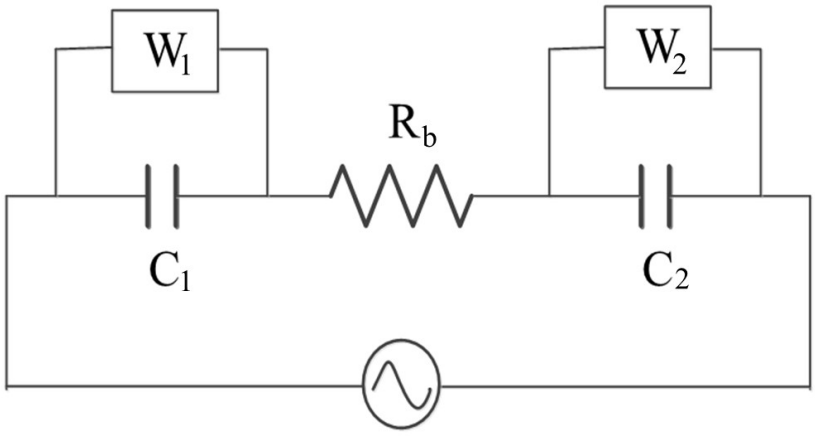

Figure 5.3: Equivalent circuit with Warburg element.

The electrochemical behavior of the system can be anaylized by fitting the electrical impedance with an equivalent electric circuit[37, 167, 102]. An equivalent circuit of the Nafion-based actuator with CNC layers was built and verified in our previous studies[37, 15]. As a result of ion accumulation at the surface of electrodes, electric double layer (EDL) capacitors are formed at the interfaces of the outer electrodes and electrolyte. The EDL capacitors in series with the resistance of bulk Nafion layer R_b can be used to model the electrochemical behavior of such systems. Previously we have shown that due to a continuous contribution of a diffuse layer to the charging and discharging current, general finite Warburg elements (GFWs) were introduced in parallel with the EDL capacitors, as shown in Figure 5.3. The impedance of the Warburg element GFW, W, is defined as

$$W = R\frac{tanh[(j\omega\tau)^P]}{(j\omega\tau)^P} \tag{5.2}$$

where R represents a diffusion impedance component independent of the frequency, P is an exponent taking values between 0 and 1, τ is a time constant associated with the diffusion process, and ω is angular frequency. In the diffusion process interpretation, the time constant τ equals to L^2/D where L is the effective diffusion thickness and D is the effective diffusion coefficient of the ionic species[168].

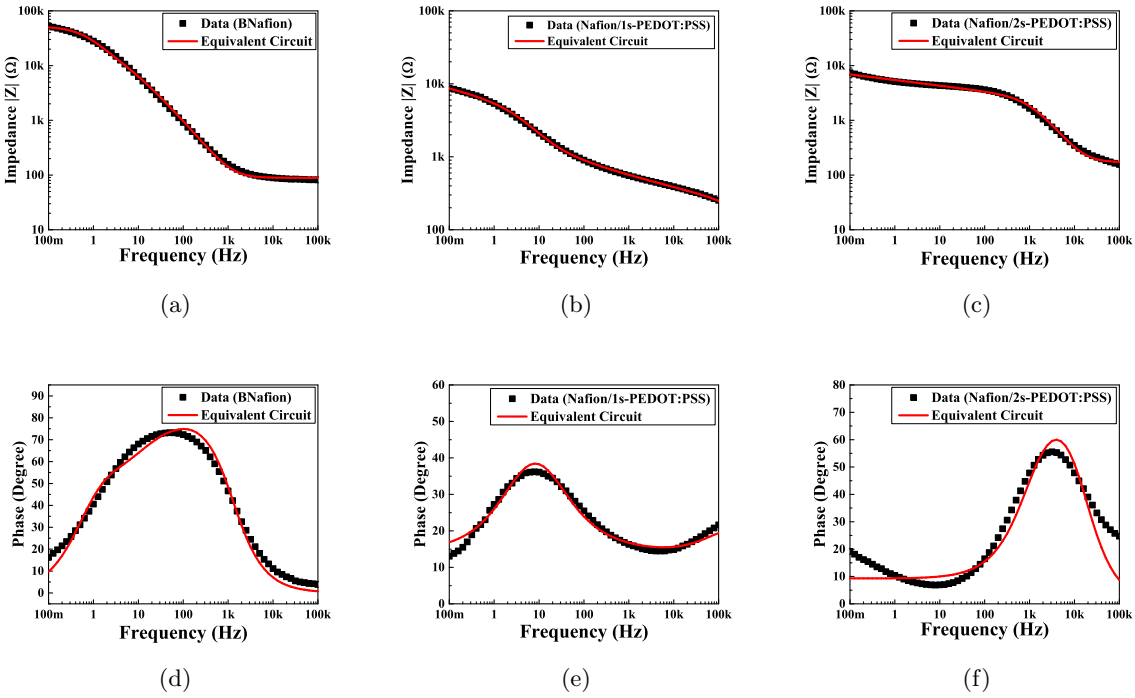

Figure 5.4: Impedance magnitude of (a) BNafion, (b) Nafion/1s-PEDOT:PSS, (c) Nafion/2s-PEDOT:PSS, and phase of (d) BNafion, (e) Nafion/1s-PEDO-T:PSS, (f) Nafion/2s-PEDOT:PSS fitted by equivalent circuit with Warburg element shown in Figure 5.3.

Considering the symmetric structure of sample BNafion and Nafion/2s-PEDOT:PSS, the two EDL capacitors and GFWs were set equally, that is, $C_1 = C_2$, and $W_1 = W_2$. Presented in Figure 5.4a–5.4f are the experimental data and the fittings (solid curves) of the electric impedance magnitude and phase of specimens BNafion, Nafion/1s-PEDOT:PSS, and Nafion/2s-PEDOT:PSS, respectively. A well match is observed between the model and the impedance spectrum in the entire frequency range. The fitting parameters for three actuators are summarized in Table 5.2. The bulk membrane resistance R_b is found to increase from 88.8 Ω (BNafion) to 171.7 Ω (Nafion/2s-PEDOT:PSS), due to the indirect contact between the ionomer and the external electrode[37]. As mentioned above, a CNC layer is commonly coated on the Nafion membrane to increase the electrodes' surface area and free volume to allow storage of free ions. When comparing BNafion and Nafion/2s-PEDOT:PSS, the existence of the PEDOT:PSS layers on both sides of Nafion leads to a significant drop in the capacitance (from 2.86 μF to 0.12 μF) of the EDL capacitor C_{dl}; consequently, the ion diffusion time from BNafion

to Nafion/2s-PEDOT:PSS significantly increases, which is consistent with the previously reported results[4]. Liu *et al.* have reported that an IEAP actuator with thicker CNC layers will have a longer ion transport time and slower charging rate. They also concluded that the charging time of IEAP actuator increased markedly as the CNC layer thickness increased[4]. Considering the thickness of PEDOT:PSS layer (∼15 μm at the center point) studied in this work, the increased diffusion time of Nafion/2s-PEDOT:PSS specimen is due to the casted polymer layers on both sides. It is also in consistent with our observation that, when compared with other IEAP actuators with thinner CNC layers, the actuators with PEDOT:PSS patterns present a much slower actuation speed, which is discussed in section 5.4. Since the total amount of charge is fixed in the system, the presence of the PEDOT:PSS layer on both sides of the Nafion membrane is more likely to hinder and limit the motion of ions.

Table 5.2: Fitting parameters for different specimens.

Circuit Element		BNafion	Nafion/1s-PEDOT:PSS	Nafion/2s-PEDOT:PSS
$R_b(\Omega)$		88.8	136.7	171.7
W_1	$R(\Omega)$	26101	51221	28098
	$\tau(s)$	0.55	46718	8.04E8
	P	0.43	0.2	0.11
W_2	$R(\Omega)$	26101	2786	28098
	$\tau(s)$	0.55	0.76	8.04E8
	P	0.43	0.22	0.11
$C_1(\mu F)$		2.86	12.7	0.12
$C_2(\mu F)$		2.86	4.52E-3	0.12

When PEDOT:PSS layer is casted on only one side of the Nafion membrane, an asymmetric charging and diffusion behavior is induced by its morphological asymmetry. As presented in Table 5.2, the capacitance C_{dl} improved on one side while dropped on the other side. The largest (12.7 μF) and smallest ($4.52E-3$ μF) capacitances of C_{dl} both occurred in the same specimen Nafion/1s-PEDOT:PSS but at different electrodes. Meanwhile, the increased ion diffused time occurs at the same side where more charge is stored in EDL capacitor, indicating a highly imbalanced storage of ions at the external electrodes. Considering the difference between BNafion and Nafion/2s-PEDOT:PSS specimens, the significantly large ion storage is expected to occur at the PEDOT:PSS coated side.

5.3.2 Charging and discharging

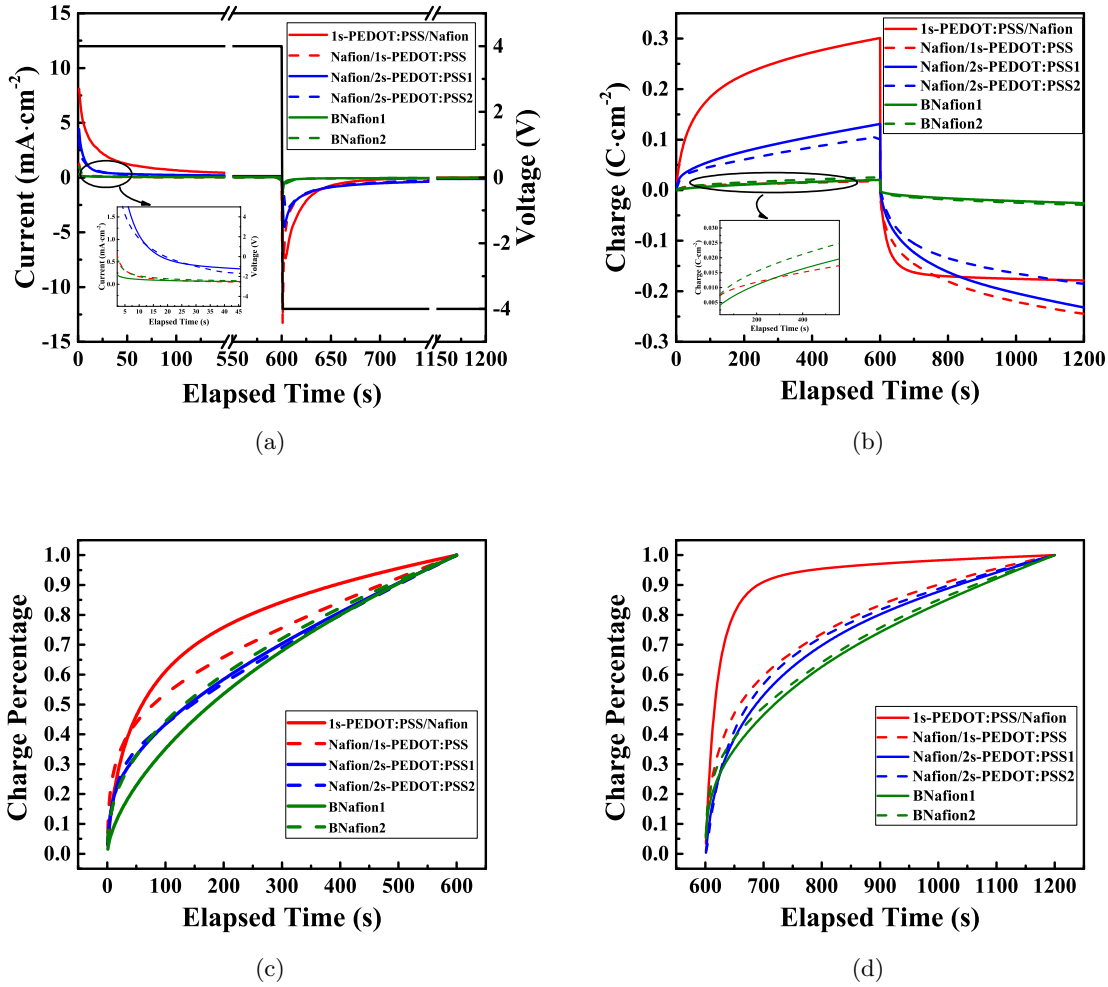

Figure 5.5: (a) Charging/discharging currents and (b) charge density versus time for different specimens under a 4 V square wave. Normalized charge versus time at the charging process (c) and discharging process (d) at the interface of the external electrodes for different specimens.

To further investigate how the morphological asymmetry affects the charging/discharging behavior under a step voltage, current flow corresponding to a 4 V potential difference between the external electrodes was measured and recorded as a function of time. Each step function was set to 600 seconds, a much larger time range for the strain generated in these actuators that has already reached saturation[65]. 1s-PEDOT:PSS/Nafion and Nafion/1s-PEDOT:PSS represent the same specimen, with PEDOT:PSS layer casted on one side of Nafion membrane,

but connected to different electrodes. Similarly, polarity was also switched in other two specimens, BNafion, and Nafion/2s-PEDOT:PSS, with the name referred to as BNafion1, 2, and Nafion/2s-PEDOT:PSS1, 2, for comparison. In Figure 5.5a, when under $+/-4$ V step functions, an unbalanced charging behavior is observed in specimen Nafion/1s-PEDOT:PSS due to its asymmetric structure, while the other two specimens, BNafion, and Nafion/2s-PEDOT:PSS, generate almost identical behaviors under altered polarity. Moreover, a significantly larger magnitude of displaced charge (area under the curve) was observed in 1s-PEDOT:PSS/Nafion. Figure 5.5b presents the corresponding charge density stored in the specimen as a function of time. Both BNafion and Nafion/2s-PEDOT:PSS showed a similar response regardless of the polarity change. However, significant difference was observed in Nafion/1s-PEDOT:PSS due to its asymmetric structure. When the PEDOT:PSS layer was connected to the higher potential at the charging process (0 – 600 seconds), the highest charge density was revealed, then a remarkable charge density at the discharging process (600 – 1200 seconds) was led. When the PEDOT:PSS layer was connected to the lower potential at the beginning (0 – 600 seconds), a pretty small charge density (closed to BNafion) was observed, followed by a much higher charge density in the discharging stage (600 – 1200 seconds). Overall specimen Nafion/1s-PEDOT:PSS (or 1s-PEDOT:PSS/Nafion) reveals the highest charge storage capacity, which is consistent with the equivalent circuit modeling results in section 5.3.1.

The normalized charge as a function of time at charging and discharging process is plotted in Figure 5.5c and 5.5d, respectively. These results reveal the charging rate at the external electrodes' surfaces. Specimen with PEDOT:PSS casted on one side (both Nafion/1s-PEDOT:PSS and 1s-PEDOT:PSS/Nafion) exhibits the fastest charging time (high ion transport rate). The asymmetry in strucutue results in an asymmetrical charging and diffusion process[169].

5.3.3 Electromechanical response

Electromechanical response of IEAP actuators with different PEDOT:PSS patterns was studied. Actuator 1S was first tested under a 4 V step function with the PEDOT:PSS patterns attached to the cathode. The cationic response was homogenous, circular toward the uncoated side, which is closed to the actuator with a similar structure but consisting of uniform CNC

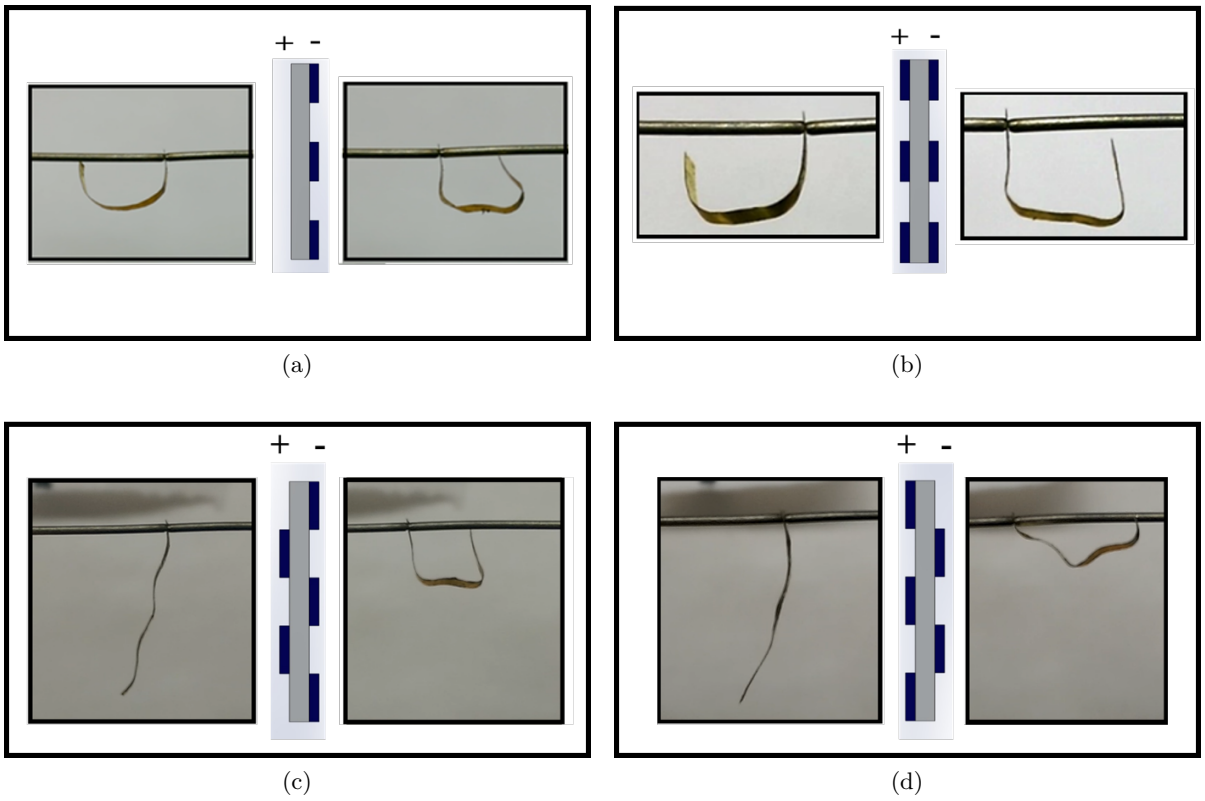

Figure 5.6: Sechematic representation and experimental actuation performance for actuator (a)1S, (b)2SS, (c)2SA2, and (d)2SA3. Left side is the cationic response and right side is the anionic response.

layers in previous works[38, 4, 39, 37, 65]. However, as the time progresses, this uniform actuation was canceled by the dominating anionic strain that consists of a sharp, angular bending, exhibiting a limb-like motion. The schematic representation of the pattern and the images of the experimental results are shown in Figure 5.6a.

To further explore how different patterns affect the actuation performance, 4 V step function was applied to the other two actuators, 2SS and 2SA; experimental results are presented in Figures 5.6b−5.6d. Electromechanical response of asymmetric 2SA actuator was studied under different polarities, named as 2SA2 and 2SA3, and the results were recorded in Figure 5.6c and 5.6d, respectively. The results shown in Figure 5.6b reveal a rectangular, limb-like motion in both cationic and anionic deformations, while actuator 2SA in Figure 5.6c and 5.6d reveals a more complex behavior, indicating a dependency on the electrode polarity. In anionic

motion, 2SA2 deformed into rectangle-like shape when actuator 2SA3 deformed into a triangle-like shape. Meanwhile, both cases have noticeable anionic deformation (strain) but negligible cationic deformation.

5.4 Discussion and Simulation

5.4.1 Discussion

Our experimental results suggest that the existence of the PEDOT:PSS layers as CNC leads to a considerable effect on the actuation performance.

First the impedance data and the corresponding equivalent circuit modeling indicate that in Nafion/1s-PEDOT:PSS specimen, ions are more likely to accumulate and act at one electrode's interface, while depleted on the other electrode's interface. The increased ion concentration is expected to occur at the PEDOT:PSS coated side. However, when the PEDOT:PSS layer is casted on both sides of Nafion, a completely different phenomenon occurs − fewer ions move to charge the EDL capacitors at the electrodes interfaces. Consequently, fewer ions will accumulated at the outer electrodes; which in turn hinders mechanical deformation of the actuator.

Secondly, 1s-PEDOT:PSS/Nafion specimen exhibits the highest charge density and shortest charging time (high ion transport rate) under a 4 V square function. Since the main cause of the actuation is exactly the accumulation and depletion of charged ions at the interfaces of different electrodes, the existence of PEDOT:PSS layer casted on only one side of Nafion would, most likely, enhance the actuation; however, when it is casted on both sides, its functionality will be reduced, or even reversed.

In addition, electromechanical responses suggest that the actuation performance varies significantly with the existence of PEDOT:PSS layer. Experimental results for actuators 1S, 2SA2 and 2SA3 all reveal an enhancement in the strain generation when PEDOT:PSS layer only exists on the convex side, and an inhibition when it only exists on the concave side. Before application of an electric voltage, EMI-Tf ions are only distributed in Nafion membrane, and none in PEDOT:PSS layer. Therefore, this enhancement-on-convex and inhibition-on-concave

phenomenon may be caused by the expansion of the PEDOT:PSS layer due to the ion penetration and accumulation at the electrodes. The experimental results for actuator 2SS, however, exhibit a completely reversed trend that, no matter in convex or concave side, PEDOT:PSS layer always hinders the actuation. That is, the existence of PEDOT:PSS layer does not contribute considerably to any expansion.

Considering the structures of the actuators investigated in this study, segments of the actuators can be categorized under three possible structures: 1) uncoated membrane (BNafion); 2) single-side coated membrane (Nafion/1s-PEDOT:PSS); and 3) double-side coated membrane (Nafion/2s-PEDOT:PSS). Scrutinizing the electromechanical response of actuators at segment scale, following conclusions are drawn: 1) for asymmetric segments, ion penetration into CNC coated side results in an irreversible expansion; 2) the CNC does not exhibit contraction, and 3) for symmetric segments, the capacitance of the double-side coated segment is significantly lower than that of the uncoated segment, thus deformation mainly occurs on the uncoated segment.

5.4.2 Finite element simulation

In order to verify the conclusions draw from experimental observations (section 5.4.1), static analyses were performed. Electromechanical response of IEAP actuators with different CNC patterns was modeled on ABAQUS/CAE using FEM (details presented in the Appendix A). Presented in Figure 5.7 are overlay images of experimental (5.7a, 5.7c, 5.7e, 5.7g) and simulated (5.7b, 5.7d, 5.7f, 5.7h) results. Experimental results are collected under a 4 V step function and figures are extracted from video recordings. Simulations are the corresponding increments from static steps where blue and red gradation represents cationic and anionic strains, respectively. Experimental and simulated data are in very good agreement, verifying the conclusive remarks made in section 5.4.1.

Hou *et al.* suggested a simple aggregation model when EMI-Tf ionic liquid was absorbed into an ionic polymer membrane (Nafion), indicating an excess of negatively charged triple ions, [Tf^-–EMI^+–Tf^-][125]. Without loss of generality, let EMI-Tf in Nafion membrane is in the format of [EMI^+] and [Tf^-–EMI^+–Tf^-]. In an IEAP actuator with dimension as 15 mm $\times$ 1

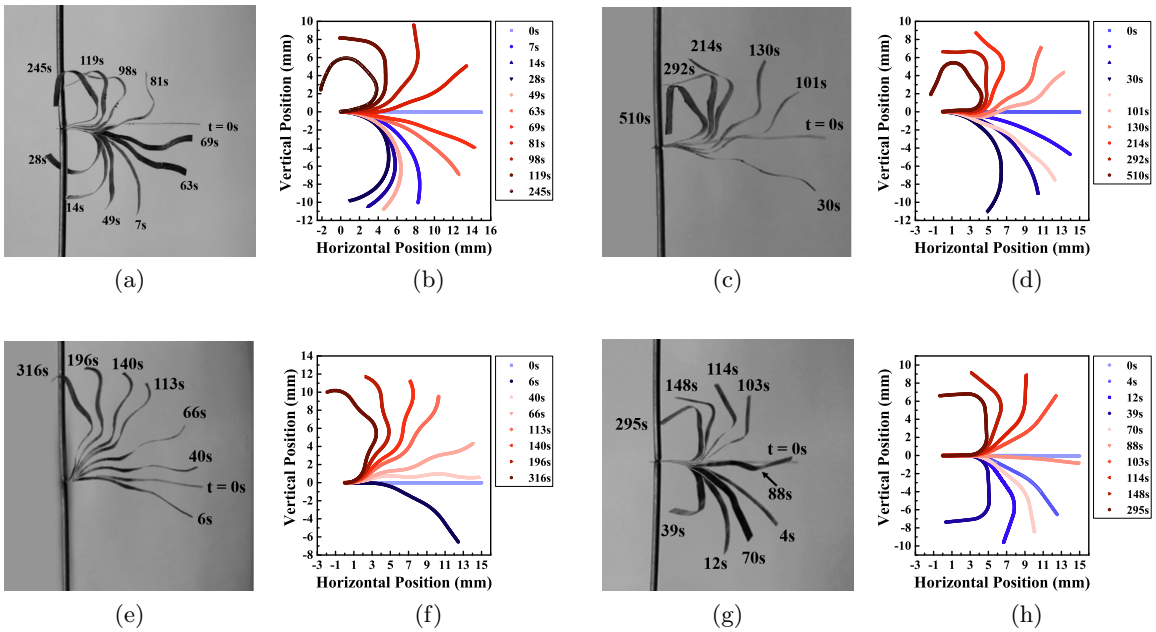

Figure 5.7: Comparison of experimental bending displacement in response to a 4 V step input voltage (left column) and the results produced by the static theoretical model via ABAQUS (right column). Figure (a) and (b) represent actuator 1S, (c) and (d) represent actuator 2SA2, (e) and (f) represent actuator 2SA3, and (g) and (h) represent actuator 2SS. The top electrode is cathode and the bottom electrode is anode.

mm ($l \times w$) and EMI-Tf uptake as $\sim$ 24 wt%, the increased weight is around $1.91E-4$ g. With the molecular weight of 260.23 g/mol in EMI-Tf, the molecular from EMI-Tf is $7.35E-7$ mol $= 4.42E17$. Therefore, the total movable cations [EMI^+] and anionic cluster [Tf^-–EMI^+–Tf^-] should be half of the total molecular inside, which equals to $2.21E17$. Meanwhile, when $\Delta T \times \alpha$ is pretty small, the change in volume by thermal expansion ΔV can be simplified into $3\alpha \cdot \Delta T \cdot V_0$, by excluding the higher orders, where V_0 is the volume before any expansion/contraction. Simulations shown Figure 5.7 confirm a change in volume $\Delta V = 1.83E-11$ m^3 in cations response. Taken the molecular volume of cations [EMI^+] as 182 $Å^3$ [65], $1.0E17$ [EMI^+] is supposed to contribute to the cationic response, which, is almost half of the mobile cations inside Nafion membrane. That is, based on the experiments and simulations indicated in Figure 5.7, approximately half of the ions from EMI-Tf contribute to the actuation.

Simulations shown in Figure 5.7 set the volume ratio of cations and anions/anionic clusters based on the results reported by Hou *et al.*, who characterized the diffusion ratio D_{cation}/D_{anion}

of EMI-Tf ionic liquid inside Nafion membranes as a function of water content χ_{water}[125]. They discovered that when 15-30 wt% EMI-Tf was absorbed in Nafion at very low water contents, the diffusion ratio falls in the range of $1.5 - 2.5$. The diffusion coefficient D is inversely proportional to the size of diffusing particles as described by the the Stokes-Einstein relation, $D = kT/(c\eta r_H)$, where k is the Boltzmann constant, T is absolute temperature, c is a constant factor depending on the shape and relative size of the diffusion particle to its surrounding fluid, η is viscosity of the fluid, and r_H is the hydrodynamic radius of the diffusing particle[125, 170]. Since the cations and anions/anionic clusters exist in the same thermodynamic phase, D_{cation}/D_{anion} equals the reciprocal of their hydrodynamic radii ratio, which is proportional to the cubic root of the ions' volume distributed in the Nafion membrane. That is, $D_{cation}/D_{anion} = r_{Hanion}/r_{Hcation} \sim (V_{anion}/V_{cation})^{1/3}$. The volume ratio of cations and anions/anionic clusters set in the simulation falls in the range of $1.5^3 - 1.7^3$, which is consistent with the results reported by Hou *et al.*

5.5 Conclusion

In this work an intrinsic limb-like motion was achieved by incorporation of conjugated polymer, PEDOT:PSS patterns in the structure of soft actuators. Instead of a homogeneous linear or circular deformation revealed by conventional IEAP actuators, the fabricated soft actuators can exhibit sharp angles of 90° and beyond. The intrinsic deformation enables a wide application of this manipulated actuator in biomimetic soft-robotics due to the natural motion indicated. Electromechanical responses indicated that the actuation performances varies significantly by the pattern design of the polymer in structure. The casted number of PEDOT:PSS layer highly determines the ionic motion through the thickness of the actuators and consequently their final performance, which has been verified both experimentally and theoretically in this study. Meanwhile, through a static model built by FEM, around half amount of the ions from EMI-Tf would contribute to the final actuation performance. With different patterns of the incorporated PEDOT:PSS, we are able to get a new kind of actuators whose behaviors are more complex but intrinsically controllable at the same time.

CHAPTER 6. NONLINEAR DYNAMIC MODELING OF IONIC POLYMER CONDUCTIVE NETWORK COMPOSITE ACTUATORS USING RIGID FINITE ELEMENT METHOD

A paper published in Sensors and Actuators A: Physical 217 (2014): 168−182

Amir Ali Amiri Moghadam, Wangyujue Hong, Abbas Kouzani, Akif Kaynak, Reza Zamani, Reza Montazami

Abstract

Ionic polymer conductive network composite (IPCNC) actuators are a class of electroactive polymer composites that exhibit some interesting electromechanical characteristics such as low voltage actuation, large displacements, and benefit from low density and elastic modulus. Thus, these emerging materials have potential applications in biomimetic and biomedical devices. Whereas significant efforts have been directed toward the development of IPMC actuators, the establishment of a proper mathematical model that could effectively predict the actuators dynamic behavior is still a key challenge. This paper presents development of an effective modeling strategy for dynamic analysis of IPCNC actuators undergoing large bending deformations. The proposed model is composed of two parts, namely electrical and mechanical dynamic models. The electrical model describes the actuator as a resistive-capacitive (RC) transmission line, whereas the mechanical model describes the actuator as a system of rigid links connected by spring-damping elements. The proposed modeling approach is validated by experimental data, and the results are discussed.

6.1 Introduction

Electroactive polymers (EAPs) are a relatively new class of functional materials with a wide variety of applications including solar cells, super capacitors, sensors and actuators [171,

172, 173]. Ionic polymer conductive network composites (IPCNCs) are nanostructures based on EAPs doped with conductive nanomaterials to enhance electromechanical performance [13]. Due to their: (i) large strains of up to 39%, (ii) bio-compatibility, (iii) micro- and nano-scale fabrication feasibility, and (iv) relatively low operation voltage [174, 175, 176], EAPs are suitable candidates for biomedical and biomimetic applications, such as artificial organs and micro-electro-mechanical systems (MEMS).

Preceding research works on IPMC actuators based on Pt-electroded Nafion indicate that these materials can produce large bending deformation under relatively low actuation voltages [124, 177, 178]. Several research studies have been carried out to investigate the key parameters which affect the electromechanical performance of IPMC actuators in terms of strain level, actuation speed, lifetime and efficiency [177, 178, 12, 36, 76, 31, 136]. Experimental results indicate that high charge density at the electrodes significantly improves the electromechanical actuation of IPCNC actuators [177, 31, 136]. As it has been shown in our previous works [39, 4, 37], integration of conductor network composite (CNC) fabricated by the layer-by-layer (LbL) self-assembly method with IPCNC bimorph actuators will considerably increase strain level and response time of the IPCNC actuators. Considering such an important effect, the current work is devoted to investigate the nonlinear large bending deformation of these actuators.

There are many reports in the literature about the potential applications of electroactive polymers in different robotic systems. Bar-Cohen et al. [171] presented several EAP driven mechanisms that emulate human hand including a gripper, a manipulator arm, and a surface wiper. Chen et al. [150] reported the modeling of a robotic fish propelled by an ionic polymer-metal composite actuator. Jain et al. [179] used IPCNC actuators as a micro gripper in the SCARA robot. We have proposed modeling and design of soft robots based on EAPs [180, 181]. However, a practical dynamic model of these actuators is required for design of advanced control systems [182, 183] and fabrication of functional devices made of IPCNC actuators.

There are several models in the literature for predicting the behavior and performance of IPCNC actuators. These models range from simple black-box models to complex white-box models [184, 185]. The complexity and accuracy are two main factors which should be

considered in development of a practical model of IPCNC actuators. The modeling complexity issue becomes even more important when IPCNC actuators are integrated into micro devices such as micro robotic systems which include several electrical and mechanical components. In this case, the complexity of the actuator model increases the overall complexity of the device model which is not desirable.

The current work aims to come up with an effective modeling strategy based on a tradeoff between the complexity and accuracy of the actuator model. Following key factors which significantly influence the development of dynamic models are defined: (i) the use of a physics-based modeling method, (ii) the consideration of electrical as well as mechanical dynamics, and (iii) the consideration of large deformation. These factors play a significant role in development of dynamic models of IPCNC actuators and thus, a model which incorporates all of these factors can more realistically predict the performance of IPCNC actuators. Several research studies have been devoted to address some of these factors in dynamic modeling of IPCNC actuators. Bar-Cohen et al. [171] proposed the use of black-box modeling approach for calculation of actuator curvature as a function of applied voltage. Although black-box models are relatively simple, they are merely based on data mapping and therefore, have a limited application. More advanced models, mainly based on a gray-box modeling approach, have been developed which use electrical circuit models to correlate the voltage and bending displacement of the IPCNC actuators. These models range from lumped RC models [37, 186, 187, 188], to distributed transmission line models [185, 189]. Finally, the most complex models are white-box models [69, 66, 70, 190]. These models try to explain the complicated electro-chemo-mechanical dynamics of IPCNC actuators based on physical principals. Although these models provide valuable insight into the underlying physics of actuation process, they are very complex and are not suitable for real time control of the actuators [184].

Despite the fact that the use of IPCNC actuators in functional devices requires nonlinear large deformation dynamic analysis of the system, the common characteristic of the described modeling strategies is that they cannot take into account the large bending deformation (geometric nonlinearity) of actuators. Addressing the large deformation of IPCNC actuators, Yim et al. [191] proposed the use of finite element method (FEM) in modeling of IPCNC actuators.

However, this method cannot consider the rigid body rotation of each element and consequently is inaccurate in predicting large bending deformation of IPCNC actuators. In an attempt to overcome this problem, Gutta et al. [192] modified the previous finite element model by attaching local coordinate frame to each element which could take into account rigid body motion of the actuator. They have also used a lumped RC model to emulate the electrical admittance of the actuator. Although this model is comparatively effective in predicting large bending deformation of IPCNC actuators, derivation of motion equation based on FEM is complex and therefore, limits the application of the proposed method for design and control of micro devices based on IPCNC actuators. Furthermore, previous studies have shown that lumped RC models are not accurate in predicting the actuators performance [37, 185, 188, 189].

Addressing the stated deficiencies, the current work proposes a dynamic model for the large deformation dynamic analysis of IPCNC actuators employing an effective rigid finite element (RFE) method. This is achieved by establishing a mathematical relation between the input voltage and the output bending displacement of the polymer actuator, considering both electrical admittance and mechanical dynamics of the actuators, simultaneously. In contrast to the classical finite element method (FEM), the RFE method discretizes the flexible links into rigid elements, which facilitates the representation of the inertial features of the body. These elements are connected by means of spring-damping elements (SDEs) [193].

The other advantages of applying the RFE method include (i) simplicity, which is reflected in the description of flexible links as a system of rigid links connected by SDEs, (ii) employment of a uniform approach to model rigid and flexible links, (iii) numerical efficiency, and (iv) applicability for the analysis of both small and large deformations. Based on these advantages, we extend the RFE method to emulate the dynamics of polymer actuators. To realize this goal, in the first step, an electrical model based on the transmission line theory is utilized to define the induced electrochemical moment which acts on the actuator, and in the next step, the actuator is replaced with a set of rigid elements which are connected by means of SDEs and controlled by the electrochemical moment. All modeling results are based on these two aforementioned steps. Despite the lack any complication in the model, experimental results indicate the model can accurately predict the behavior of the actuator.

The paper is organized as follows. In Section 6.2, trilayer IPCNC actuators are introduced, and the synthesis of a polymer actuator is described. Section 6.3 presents a dynamic analysis of polymer actuators based on the proposed RFE method. Finally, in Section 6.4, the model is validated by using simulation, and the corresponding experimental results are presented.

6.2 Ionic Polymer Conductive Network Composite (IPCNC) Actuators

IPCNC actuators were fabricated by the direct assembly method in which the CNC electrodes were developed by means of layer-by-layer (LbL) ionic self-assembly technique [89]. The constitution and geometry of these actuators is depicted in Figure 6.1(a). The actuators consist of five layers. According to Figure 6.1(a), the middle layer is the ionomer which is sandwiched between CNCs and on both side of CNCs there are gold leaves as external electrodes [39, 4, 37]. Figure 6.1(b) demonstrates the bending mechanism in IPCNC actuators. Under electrical stimuli, diffusion and drift of ions through the ionomeric membrane and CNC layers, and their accumulation at the oppositely-charged electrodes, creates a volume imbalance in the system which in turn causes the bending motion of IPCNC actuators; the motion can be reversed by reversing the polarity of the electric voltage [13, 4, 37].

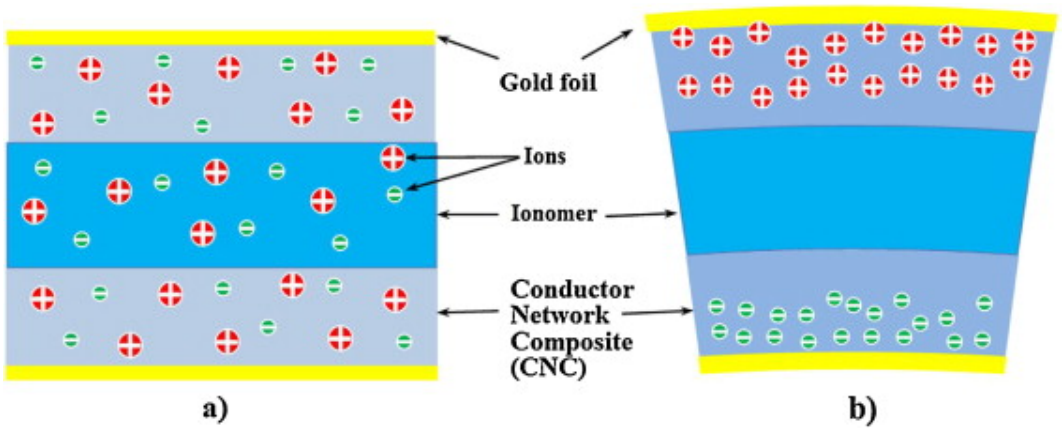

Figure 6.1: (a) Structure of a goldCNCionomerCNCgold five-layer actuator. (b) Bending mechanism in the IPCNC actuator based on accumulation of ions at oppositely-charged electrodes (not to scale).

6.2.1 Synthesis of the actuator

In this study, the commercial Nafion membrane (NR-211, Ion Powers) with the thickness of 25 μm was used as the ionomeric membrane. Subsequently, to fabricate CNCs, Nafion membrane was immersed into two oppositely charged solutions which contain anionic gold nanoparticles (AuNPs) and the polycation poly(allylamine hydrochloride) (PAH) [4]. The composites grew via the electrostatic force between polyelectrolyte and nanoparticles. Each CNC layer consists of 20 bilayers of AuNP/PAH, with an approximate thickness of 40 nm [40]. Next, the sample was soaked with 40 wt% 1-ethyl-3-methylimidazolium trifluoromethanesulfonate (EMI-Tf) ionic liquid, and 50 nm thick gold leaves were hot-pressed on both side of sample as external electrodes [4].

6.3 Electromechanical Modeling

The electromechanical model used in this paper, as its name implies, is comprised of both electrical and mechanical models. Each of these two components is discussed in a separate sub-section.

6.3.1 Electrical modeling

An electrical circuit is used to model the electrochemical process within the IPCNC actuators. The electrical charge can be stored within the actuator which is analogous to a capacitance element in an electrical circuit. Moreover, the energy loss in the actuator can be modeled as an electrical resistance. Thus, the simplest electrical admittance model for IPCNC actuators can be a lumped electrical circuit model [4, 188]. It has been shown that a lumped C-R-C circuit model can be used to approximate the complex electrical impedance model of the IPCNC actuators [4, 37, 188]. In this model, two capacitor elements refer to the formation of double-layer capacitors at the interfaces of two electrodes and the electrolyte, and the resistor element represents the internal resistance of the electrolyte. Moreover, possible leakage in the system can be represented by a shunt resistor (Figure 6.2(a)). Considering the electrical circuit in Figure 6.2(a), the transfer function of the electrical admittance between input voltage and

output current is:

$$\frac{I_t}{V_{in}} = \frac{(R_1 + R_2)Cs/2 + 1}{R_1(R_2Cs/2 + 1)} \tag{6.1}$$

where, s is Laplace variable.

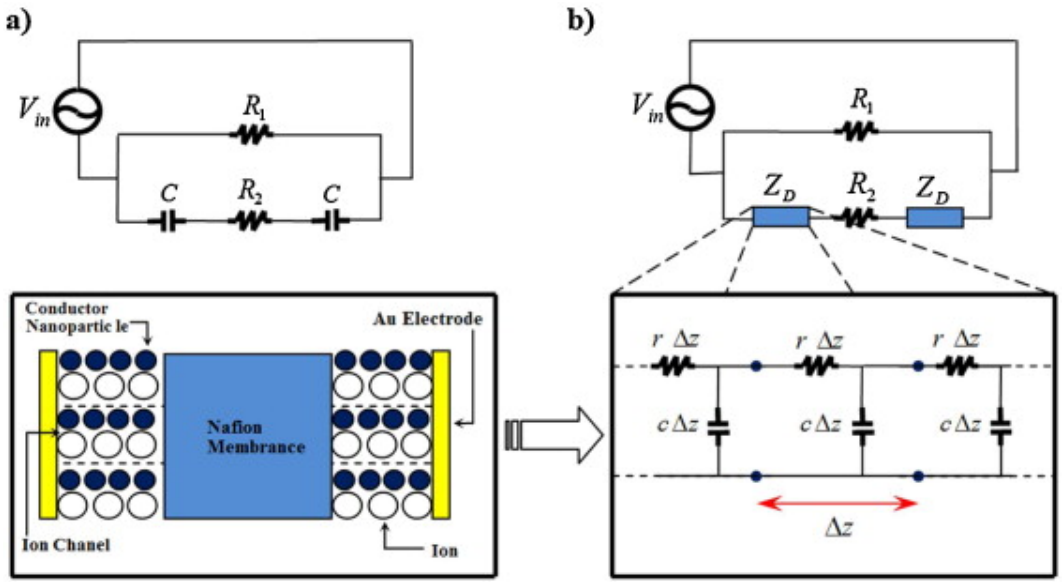

Figure 6.2: (a) Equivalent lumped electrical circuit model IPCNC actuators. (b) Transmission line model of IPCNC actuators.

Although this simple relation provides initial insight into the electrical dynamics of the actuator, it cannot accurately predict the performance of the actuator; in effect, experimental observation not only in the current work but in previous studies [4, 37, 188] suggests that a capacitor element with constant value cannot accurately model the output current of the actuator. To address this issue, Bao et al. [188] proposed that the ion diffusion at the electrode/electrolyte interfaces can be modeled with a RC transmission line model. Since then, several authors have employed transmission line models for modeling the electrical admittance of IPCNC actuators [185, 189]. In these models, electrical parameters of the actuators such as electrolyte resistance, shunt resistance and double-layer capacitors are defined as distributed parameters along the thickness of the actuator. Apparently, incorporation of several distributed parameters into the transmission line model not only makes the derivation of admittance model complicated, but complicates the identification of the actuator electrical parameters as well. To address this issue in the current work, the electrical model is defined as the integration of lumped resis-

tor elements and RC transmission line model where both electrolyte and shunt resistances are lumped parameter elements. Moreover dynamic of ion diffusion at electrode/electrolyte interfaces is replaced with an RC transmission line model (Figure 6.2(b)). This modeling approach significantly simplifies the derivation of the admittance model as well as the identification of its parameters.

The first step in derivation of the distributed admittance model of the actuator, shown in Figure 6.2(b), is to calculate the impedance of ion diffusion at the electrode/electrolyte interfaces. This will be done based on the equivalent single unit circuit in Figure 6.3.

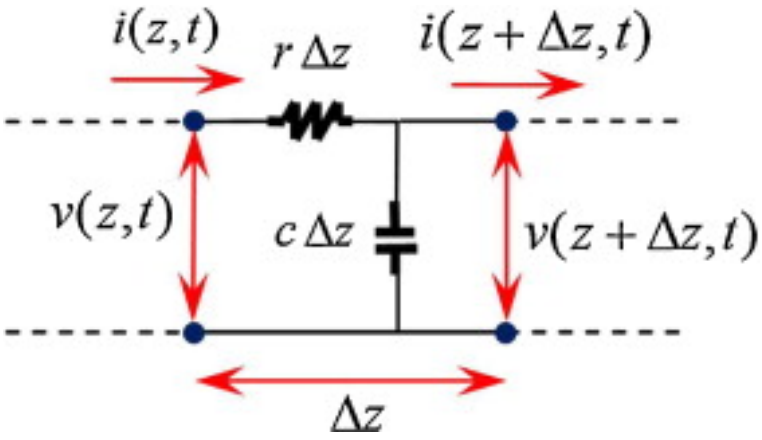

Figure 6.3: The equivalent single unit circuit for ion diffusion at the electrode/electro-lyte interface.

Considering Kirchhoff's and Ohm's laws, the relation between current and voltage for ion diffusion in Figure 6.3 can be derived as:

$$\frac{\partial V(z,t)}{\partial z} = -ri(z,t) \tag{6.2a}$$

$$\frac{\partial i(z,t)}{\partial z} = -c\frac{\partial V(z,t)}{\partial t} \tag{6.2b}$$

where r and c are the resistance, and capacitance per unit thickness of the CNCs, respectively. Next, by substituting partial derivative of Equation 6.2a with respect to z into Equation 6.2b, the governing equation of the RC line can be simplified as:

$$\frac{\partial^2 V(z,t)}{\partial z^2} = rc\frac{\partial V(z,t)}{\partial t}, \qquad 0 \le z \le h \tag{6.3}$$

The general solution of Equation 6.3 can be derived as:

$$V(z,s) = Asinh(z\sqrt{\frac{s}{\beta}}) + Bcosh(z\sqrt{\frac{s}{\beta}}) \tag{6.4}$$

where $\beta = 1/rc$.

Also, the suitable boundary conditions can be defined as:

$$V(0,s) = V_{in}, \quad I(h,s) = 0 \tag{6.5a}$$

$$\frac{V(z,s)}{V_{in}} = cosh(z\sqrt{\frac{s}{\beta}}) - tanh(h\sqrt{\frac{s}{\beta}})sinh(z\sqrt{\frac{s}{\beta}}) \tag{6.5b}$$

Thus, the current in the RC line is:

$$\frac{I(z,s)}{V_{in}} = \frac{1}{r}\sqrt{\frac{s}{\beta}}[tanh(h\sqrt{\frac{s}{\beta}})cosh(z\sqrt{\frac{s}{\beta}}) - sinh(z\sqrt{\frac{s}{\beta}})] \tag{6.6}$$

Moreover, the impedance of the RC line is:

$$Z_D = \frac{rcoth(h\sqrt{s/\beta})}{\sqrt{s/\beta}} \tag{6.7}$$

Therefore, the charging current can be defined as:

$$\frac{I_{ch}}{V_{in}} = \frac{1}{2Z_D + R_2} \tag{6.8}$$

And finally according to Figure 6.2(b), the total current in the circuit can be obtained as:

$$\frac{I_t}{V_{in}} = \frac{(R_1+R_2)/2Z_D + 1}{R_1(R_2/2Z_D + 1)} = \frac{(R_1+R_2)c\sqrt{\beta s}tanh(h\sqrt{s/\beta})/2 + 1}{R_1(R_2c\sqrt{\beta s}tanh(h\sqrt{s/\beta})//2 + 1)} \tag{6.9}$$

To study the infinite-dimensional system in Equation 6.9, one can utilize the Mittag-Leffler's expansion of $tanh(s)$:

$$tanh(s) = 2s\sum_{n=0}^{\infty}\frac{1}{s^2 + (n+1/2)^2\pi^2} \tag{6.10}$$

Thus after some manipulations, the electrical admittance model of the actuator can be obtained as:

$$\frac{I_t}{V_{in}} = \frac{(R_1+R_2)((c\beta s/h)\sum_{n=0}^{\infty}(1/s + (2n+1)^2(\pi/2h)^2\beta)) + 1}{R_1(R_2(c\beta s/h)\sum_{n=0}^{\infty}(1/s + (2n+1)^2(\pi/2h)^2\beta) + 1)} \tag{6.11}$$

where h is the thickness of the CNC layer.

6.3.2 Electrical parameter identification

The parameters R_1 and R_2 can be directly obtained from experimental current response under a step input voltage:

$$R_1 = \frac{V_{in}}{I_t}|_{\text{steady state}}, \qquad R_2 = \frac{V_{in}}{(I_t|_{\text{initial}} - I_t|_{\text{steady state}})} \tag{6.12}$$

where $I_t|_{\text{initial}}$ and $I_t|_{\text{steady state}}$ are the initial and steady state experimental current response of the actuator, respectively. Moreover, parameters r and c can be identified by means of system identification methods. In this work, system identification is performed by means of simulated annealing method which is one of the most efficient optimization algorithms [194, 195]. The error signal is defined as the difference between the experimental and simulated current output of the actuator, and consequently, the objective function is defined as the integral of squared relative error. Moreover, the vector of unknown parameters γ is defined as:

$$\gamma = [r, c]^T \tag{6.13}$$

According to Figure 6.4, it can be observed that the objective function converges after approximately 80 iterations. The values of the electrical model parameters are presented in Table 6.1.

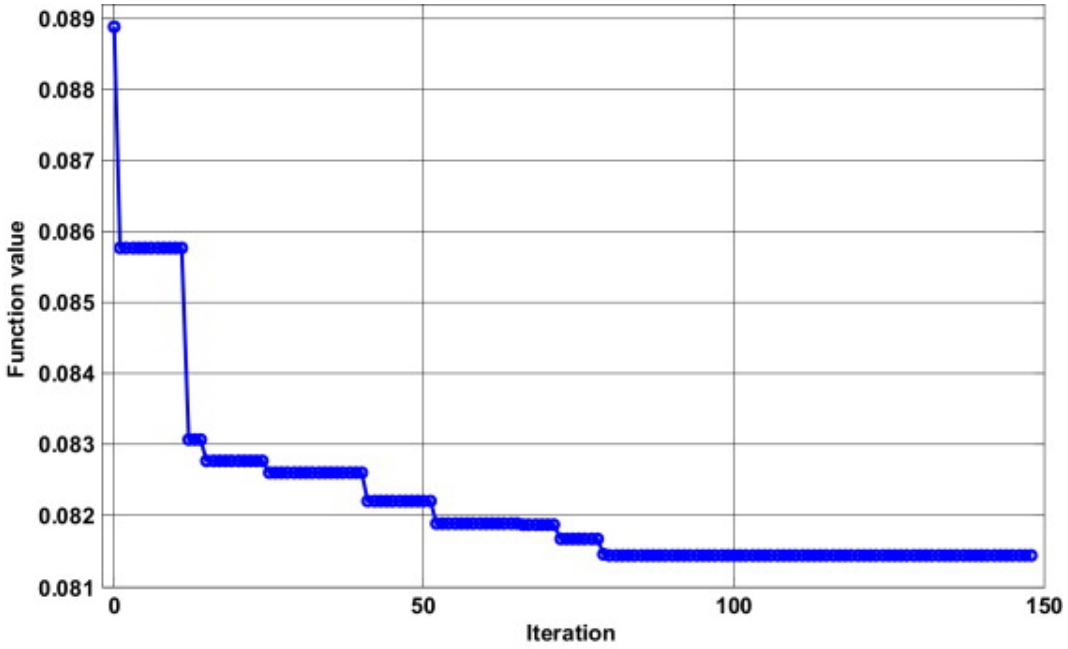

Figure 6.4: Convergence of the objective function based on the simulated annealing algorithm.

Table 6.1: Values of physical parameters for electrical admittance model.

$R_1(\Omega)$	$R_2(\Omega)$	$c(F/m)$	$r(\Omega/m)$
1158.9	115.45	14100	2.7278×10^8

6.3.3 Validation of electrical model

The convergence of the electrical model can be studied based on the number of terms (n) used in Equation 6.11. Table 6.2 shows the poles of the electrical admittance model based on using different values for (n). It can be seen that using more terms in Equation 6.11 generates poles which are located far to the left of the imaginary axis in comparison with other poles of the system. This suggests that the electrical admittance model will converge to the infinite-dimensional by using finite number of terms in Equation 6.11.

Table 6.2: Poles of the electrical admittance based on number of terms.

n	Poles
1	$(s + 1.854)$
3	$(s + 69.69)(s + 20.97)(s + 1.789)$
5	$(s + 250.6)(s + 142.3)(s + 66.12)(s + 20.27)(s + 1.776)$
7	$(s + 544.6)(s + 377.3)(s + 242.8)(s + 138.9)(s + 64.83)(s + 19.89)(s + 1.77)$

Typically IPCNC actuators produce very little bending displacement at relatively high frequencies and consequently have a low bandwidth (under 10 Hz) [184, 185, 110]. With this in mind the convergence of the electrical admittance model can be studied within the bandwidth of the actuator. According to Figure 6.5, it can be seen that the admittance model with $n = 5$ closely matches the infinite-dimensional model for the frequency range less than 20 Hz. Therefore, this model is chosen for simulation of electrical admittance model. Moreover, the step response could be utilized to study the convergance of the electrical addmitance model in terms of time constant and steady state response of the systesm. According to Figure 6.6, it can be see that the models with 5 and 7 terms almost have the same time constant, and setteling time.

Figure 6.7 compares the experimental current output of the polymer actuator with the lumped RC model and the transmission line model in response to a step voltage input. It can

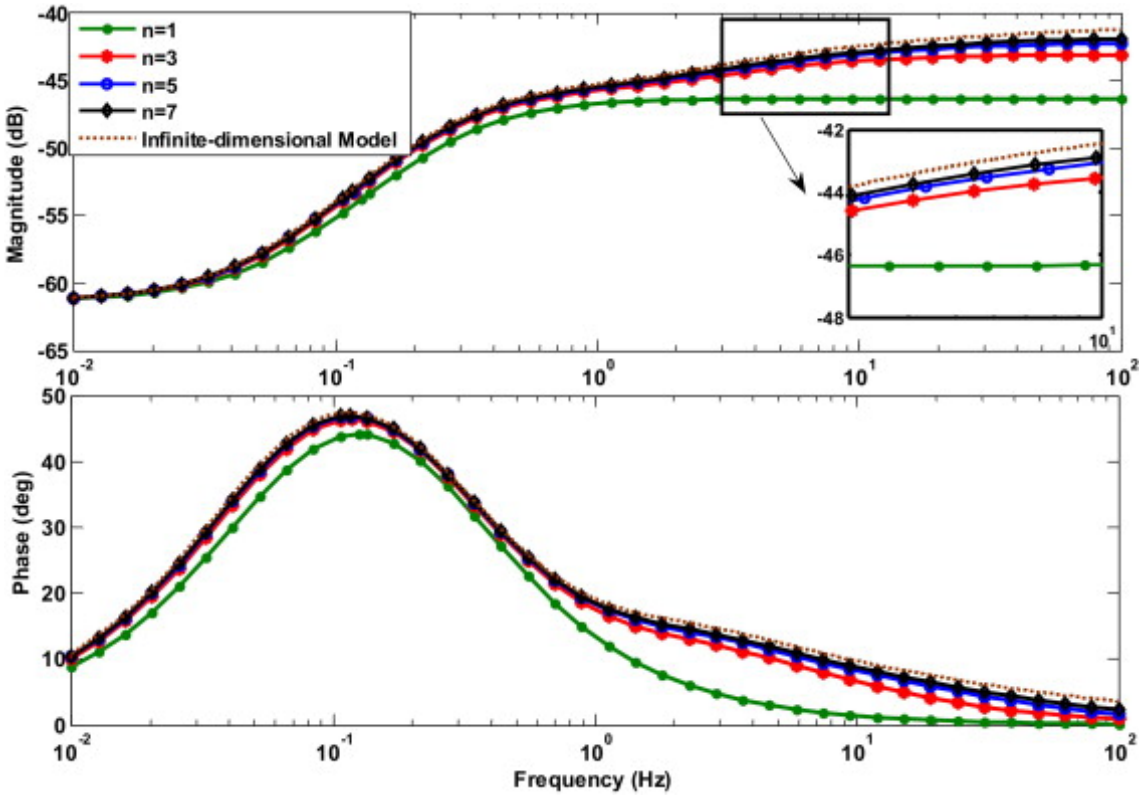

Figure 6.5: Convergence of the transmission line model in frequency domain.

be seen from this figure that the distributed model is more accurate compared to the lumped RC model in predicting the actuator current response.

Integral of square error (ISE) can be used to compare the accuracy of the lumped and distributed electrical models:

$$ISE = \int_0^t e^2(t)dt \tag{6.14}$$

Table 6.3 compares the ISE of distributed model with the lumped model. It can be seen that the ISE of distributed model is about 4 times less than the lumped model which indicates the effectiveness of the proposed transmission line approach in modeling of the actuator electrical admittance.

Table 6.3: Comparison of ISE for lumped and distributed electrical models.

	Transmission line model	**Lumped circuit model**
ISE	2.8434×10^{-6}	1.0999×10^{-5}

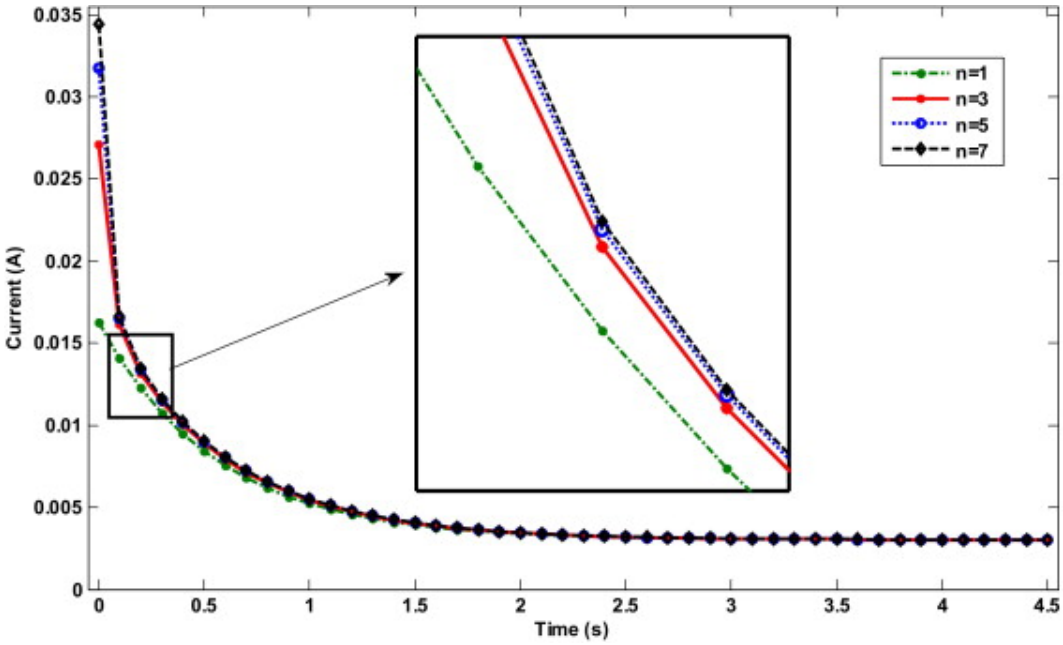

Figure 6.6: Convergence of the transmission line model in predicting the actuator current response.

Comparison of experimental current data with the lumped electrical model shows that at the beginning of the process, the experimental current drops relatively faster than the prediction of the lumped model. However, as the actuator charges up, the lumped model shows a faster charging rate. This indicates that a constant capacitor element in the lumped model is not suitable for prediction of the actuator performance. To capture the gross dynamic of ion diffusion at the electrode/electrolyte interfaces, we have used an effective RC transmission line model. By definition a control oriented model is the least complex model which captures the gross dynamic of the system. Hence, a key factor in the development of a proper control oriented model is a proper tradeoff between the complexity and the accuracy of the corresponding model. In order to further evaluate the proposed model, it has been compared with more complex models [184, 185] in prediction of the electrical impedance of a different IPCNC sample ($37 \times 5.5 \times 0.360$ mm^3). As is seen in Figure 6.8, the proposed model is in close agreement with the experimental data, indicating that the model is significantly effective in capturing the dynamic of ion diffusion.

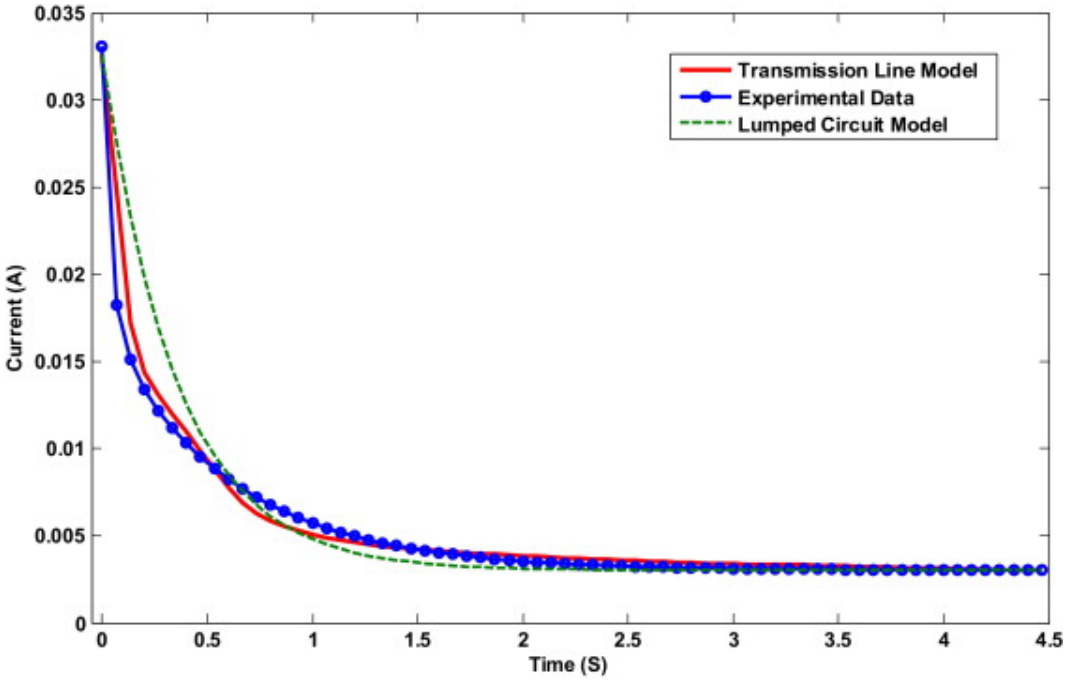

Figure 6.7: Convergence of the transmission line model in predicting the actuator current response.

6.3.4 Mechanical modeling

In contrary to the aforementioned electrical model, which relates the current to the stored charges, the mechanical model relates the stored charges to the bending displacement of the IPCNC actuators. The basic idea in the mechanical modeling part is to consider the polymer actuator as a discretized system which consists of rigid finite elements (RFEs) connected by springdamping elements (SDEs). In this model, each rigid finite element moves based on the induced electrochemical moment, denoted by $M^{(i)}$ acting at RFE$^{(i)}$. As is shown in Figure 6.9, the actuator is divided into $(n+1)$ RFEs and (n) SDEs. The components RFE$^{(i)}$ and RFE$^{(i-1)}$ are considered to be connected by means of revolute joint at SDE$^{(i)}$. Moreover, SDEs comprise of rotational stiffness ($k^{(i)}$) and damping elements ($c^{(i)}$). These parameters will be introduced later in this section.

It was experimentally shown that the induced electrochemical stress is proportional to the charge density (ρ_{ch}) [70].

$$\sigma_{ch} = \alpha \rho_{ch} \tag{6.15}$$

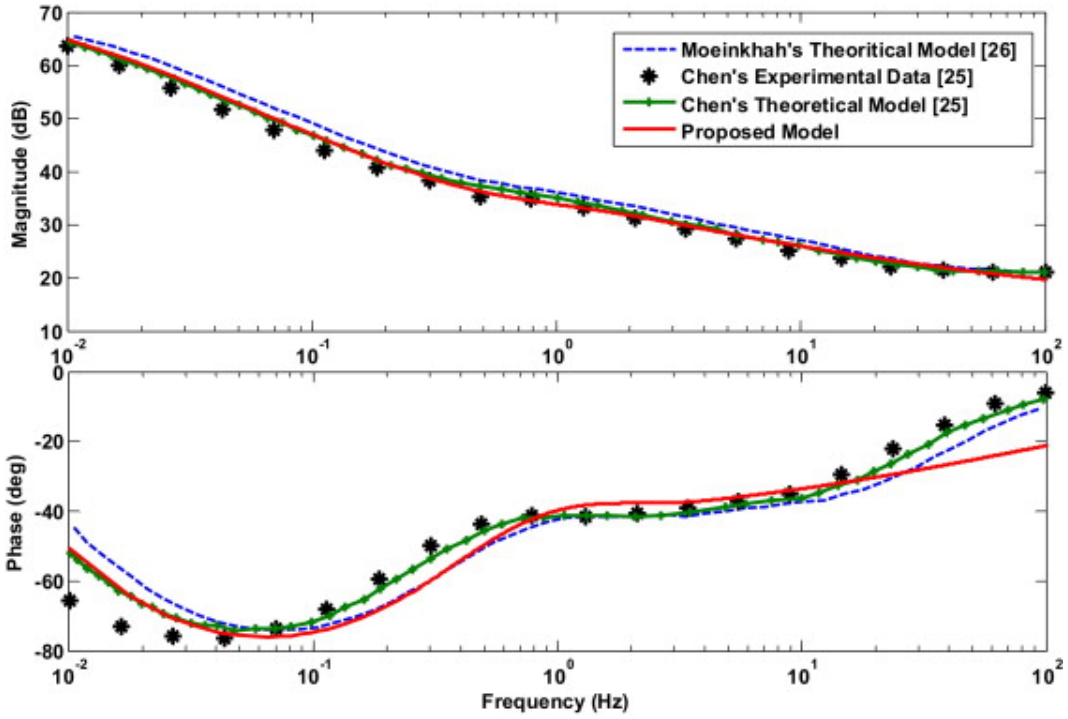

Figure 6.8: Comparison of the proposed electrical model with the other models.

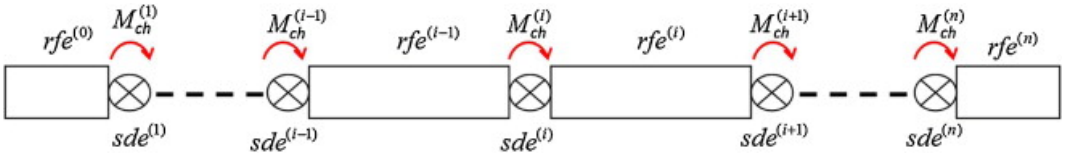

Figure 6.9: Discretization of a three-layer IPCNC actuator into RFEs and SDEs.

where α is the tress-to-charge ratio, and ρ_{ch} can be achieved in the time domain as follows:

$$\rho_{ch} = \frac{1}{bLh}\int_0^t I_{ch}(t)dt \tag{6.16}$$

where b, h and L are the width, thickness and length of CNC layer respectively. Recalling that the CNC layer is responsible for actuation in IPCNC actuators [4], the induced electrochemical moment in the ith element can be defined as (Figure 6.10):

$$M_{ch}^{(i)}(t) = \int_A \sigma_{ch} z dA = 2b\alpha\rho_{ch}\int_{h_1}^{h_2} z dz = \frac{\alpha(h_2+h_1)}{L}\int_0^t I_{ch}(t)dt \tag{6.17}$$

Now, the motion of components (RFEs) can be studied by assigning suitable generalized coordinates to them. According to Figure 6.11, the coordinate system $\{X(i)\}$ and $\{Y(i)\}$ are attached to RFE$^{(i)}$ and SDE$^{(i)}$. It must be noted that the orientation of the coordinate system

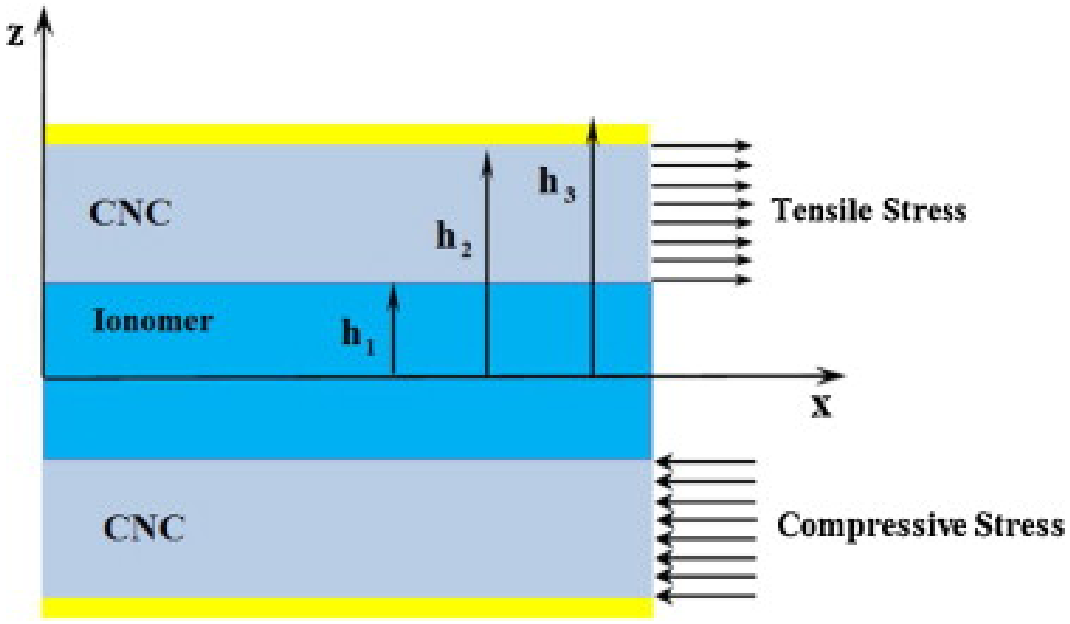

Figure 6.10: Distribution of induced electrochemical stress across the thickness of IPCNC actuators.

$\{Y(i)\}$ coincides with the coordinate system $\{X(i-1)\}$. Thus, the transformation matrix which defines the frame $\{X(i)\}$ relative to the frame $\{X(i-1)\}$ is expressed as:

$$\widetilde{B}^{(i)} = \begin{bmatrix} cos(\varphi^{(i)}) & -sin(\varphi^{(i)}) & d^{(i)} \\ sin(\varphi^{(i)}) & cos(\varphi^{(i)}) & 0 \\ 0 & 0 & 1 \end{bmatrix} \tag{6.18}$$

where, $\varphi^{(i)}$ is the angle between these two frames. Considering that the actuator has a length of L, and is divided into $(n+1)$ RFEs, the value of $d^{(i)}$ can be calculated through the following relation:

$$d^{(1)} = \frac{L}{2n}, \qquad d^{(i)} = \frac{L}{n} \qquad i = 2, 3, \cdots, n \tag{6.19}$$

Then the transformation matrix which defines the frame $\{X(i)\}$ relative to the frame $\{X(0)\}$ is calculated as:

$$B^{(i)} = \widetilde{B}^{(1)}\widetilde{B}^{(2)} \cdots \widetilde{B}^{(i)} \qquad i = 1, 2, \cdots, n \tag{6.20}$$

Consequently, the position of any particle dm in RFE$^{(i)}$ with respect to the frame $\{X(0)\}$ is defined as:

$$r^{(i)} = B^{(i)}\widetilde{r}^{(i)} \qquad i = 1, 2, \cdots, n \tag{6.21}$$

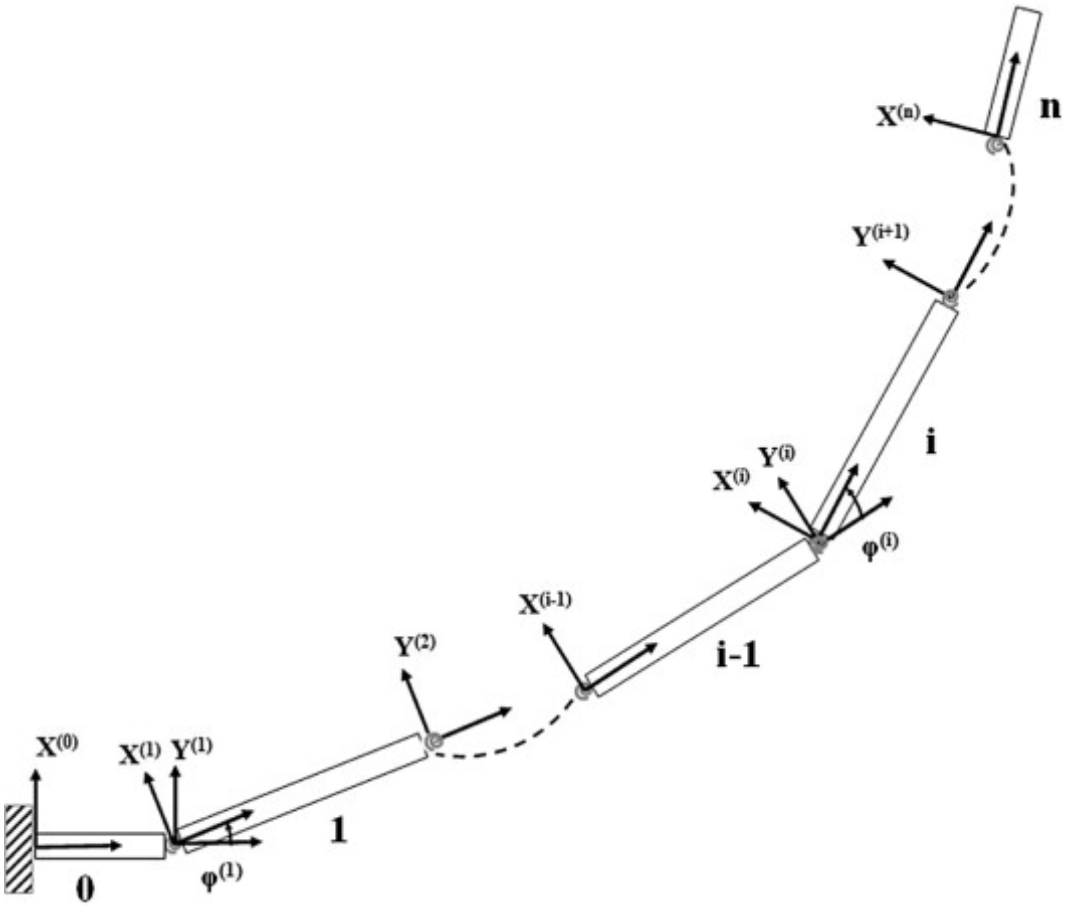

Figure 6.11: Frame assignment for RFEs and SDEs.

where $\widetilde{r}^{(i)} = [\widetilde{x}_1^{(i)} \widetilde{x}_2^{(i)} 1]^T$ and $r^{(i)} = [x_1^{(i)} x_2^{(i)} 1]^T$ are the position vector of the particle dm relative to frame $\{X(i)\}$ and $\{X(0)\}$, respectively. Therefore, the kinetic energy of the particle dm is represented as:

$$dT^{(i)} = \frac{1}{2} tr\{\dot{r}^{(i)} \dot{r}^{(i)^T}\} dm^{(i)} \qquad i = 1, 2, \cdots, n. \tag{6.22}$$

It follows that the kinetic energy of the RFE$^{(i)}$ is obtained as:

$$\begin{aligned} T^{(i)} &= \frac{1}{2} \int_{m^{(i)}} tr\{\dot{r}^{(i)} \dot{r}^{(i)^T}\} dm^{(i)} \\ &= \frac{1}{2} \int_{m^{(i)}} tr\{\dot{B}^{(i)} \widetilde{r}^{(i)} \widetilde{r}^{(i)^T} \dot{B}^{(i)T}\} dm^{(i)} \\ &= \frac{1}{2} tr\{\dot{B}^{(i)} [\int_{m^{(i)}} \widetilde{r}^{(i)} \widetilde{r}^{(i)^T} dm^{(i)}] \dot{B}^{(i)T}\} \\ &= \frac{1}{2} tr\{\dot{B}^{(i)} H^{(i)} \dot{B}^{(i)T}\} \qquad i = 1, 2, \cdots, n \end{aligned} \tag{6.23}$$

where $H^{(i)}$ is the pseudo-inertia matrix, which is defined as:

$$H^{(i)} = \int_{m^{(i)}} \widetilde{r}^{(i)} \widetilde{r}^{(i)^T} dm^{(i)} \qquad i = 1, 2, \cdots, n \tag{6.24}$$

Thus, the kinetic energy can be rewritten as:

$$T^{(i)} = \frac{1}{2} tr\{\dot{B}^{(i)} H^{(i)} \dot{B}^{(i)^T}\} \qquad i = 1, 2, \cdots, n \tag{6.25}$$

Finally, the kinetic energy of the actuator is determined by summing over all RFEs:

$$T = \sum_{i=1}^{n} T^{(i)} \tag{6.26}$$

The potential energy of the rotational springs at SDEs is expressed as:

$$V = \sum_{i=1}^{n} \frac{1}{2} k^{(i)} [\varphi^{(i)}]^2 \tag{6.27}$$

where $k^{(i)}$ is the coefficient of rotational stiffness which can be defined as [193]:

$$k^{(i)} = \frac{nEI}{L} \tag{6.28}$$

where E is the Young's modulus and I is the area moment of inertia of the actuator. Moreover, the function of energy dissipation is

$$D = \sum_{i=1}^{n} \frac{1}{2} c^{(i)} [\dot{\varphi}^{(i)}]^2 \tag{6.29}$$

where $c^{(i)}$ is the coefficient of rotational damping which can be defined as [193]]:

$$c^{(i)} = \frac{n\eta I}{L} \tag{6.30}$$

In the above relation η is the normal damping material constant. The virtual work which is done by induced electro chemical moment is defined as:

$$\delta W = \delta[\sum_{i=1}^{n} M(t)_{ch}^{(i)} \varphi^{(i)}] \tag{6.31}$$

Thus, the generalized forces ($Q^{(i)}$) is obtained as:

$$Q^{(i)} = M(t)_{ch}^{(i)} \qquad i = 1, 2, \cdots, n \tag{6.32}$$

Next, based on Lagrange's equations, the discrete set of equations that describe the dynamic of the actuator is derived as follows:

$$\frac{d}{dt}(\frac{\partial T}{\partial \dot{q}_i}) - \frac{\partial T}{\partial q_i} + \frac{\partial V}{\partial q_i} + \frac{\partial D}{\partial \dot{q}_i} = Q^{(i)} \qquad i = 1, 2, \cdots, n \tag{6.33}$$

where the vector of generalized coordinates, q, is defined as:

$$q = [\varphi^{(1)}, \varphi^{(2)}, \cdots, \varphi^{(n)}]^T \tag{6.34}$$

Finally, the equations of motion can be rewritten in the compact matrix form as:

$$A(t)\ddot{q} + e(q, \dot{q}, t) + C\dot{q} + Kq = Q(t) \tag{6.35}$$

where:

$$A(t) = [a_{ij}], \quad a_{ij} = \sum_{k=max\{i,j\}}^{n} tr\{\frac{\partial B^{(k)}}{\partial q_i} H^{(k)} (\frac{\partial B^{(k)}}{\partial q_j})^T\} \tag{6.36}$$

$$e(q, \dot{q}, t) = \{e_i\}, \quad e_i = \sum_{k=i}^{n} tr\{\frac{\partial B^{(k)}}{\partial q_i} H^{(k)} (\sum_{h=1}^{k}\sum_{j=1}^{k} \frac{\partial^2 B^{(k)}}{\partial q_h \partial q_j} \dot{q}_h \dot{q}_j)^T\} \tag{6.37}$$

$$C = diag\{c^{(1)}, c^{(2)}, \cdots, c^{(n)}\} \tag{6.38}$$

$$K = diag\{k^{(1)}, k^{(2)}, \cdots, k^{(n)}\} \tag{6.39}$$

To simulate the motion of the actuator, in the first step the induced electrochemical moment is obtained based on Equation 6.8 and 6.17. Next, the nonlinear dynamics of the actuator (Equation 6.35) is solved for the angular acceleration ($\ddot{q}$)

$$\ddot{q} = A^{-1}(t)[Q(t) - e(q, \dot{q}, t) - C\dot{q} - Kq] \tag{6.40}$$

Given the initial condition of the actuator motion as

$$q(0) = q_0, \dot{q}(0) = \dot{q}_0 \tag{6.41}$$

The angular position and velocity $(q, \dot{q})$ can be obtained by means of Euler integration method as follows

$$\dot{q}(t + \Delta t) = \dot{q}(t) + \ddot{q}\Delta t \tag{6.42a}$$

$$q(t + \Delta t) = q(t) + \dot{q}(t)\Delta t + \frac{1}{2}\ddot{q}(t)\Delta t^2 \tag{6.42b}$$

Finally, bending displacement of the actuator is obtained by using kinematics model (Equation 6.21).

6.4 Comparison of Simulation and Experimental Results

In order to validate the theoretical model, the anticipated behavior of the actuators was compared to experimental data. For this purpose, as shown in Figure 6.12, a $0.0268mm \times 1mm \times 10.9mm$ IPCNC actuator was employed, and a known voltage of 3.5 V was supplied to the actuator by means of a potentiostat. A Keithley 2400 source meter was used to measure and store the current passing through the actuator, and the actuator motion was recorded by a Canon 5D Mark III full frame camera fitted with a 100 mm/f2.8 IS Macro lens. The experimental setup is shown in Figure 6.13. In addition, numerical simulations of the actuation were performed using MATLAB software. Experimental observation shows that the voltages more than 4 V damage our IPCNC actuators. Thus, to avoid any damage to the actuator, the maximum voltage of 3.5 V is chosen for experiments. A point worth mentioning is that for lower input voltages, the actuator dynamic performance shows more linearity, and as a result the experimental data matches better to the simulation results.

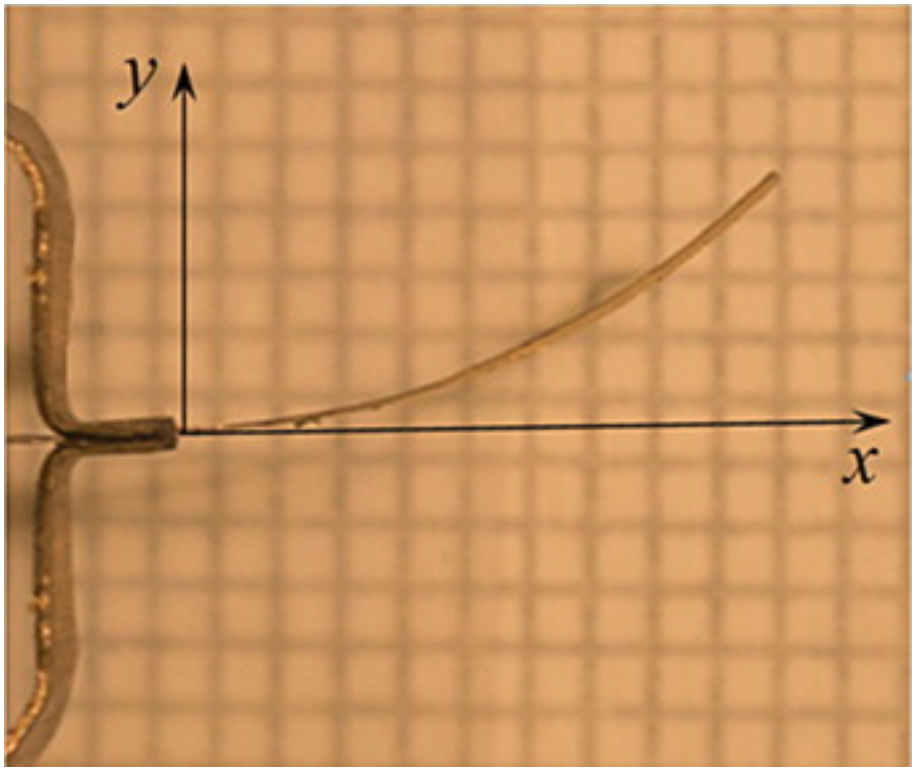

Figure 6.12: Frame assignment and bending deformation of IPCNC actuator.

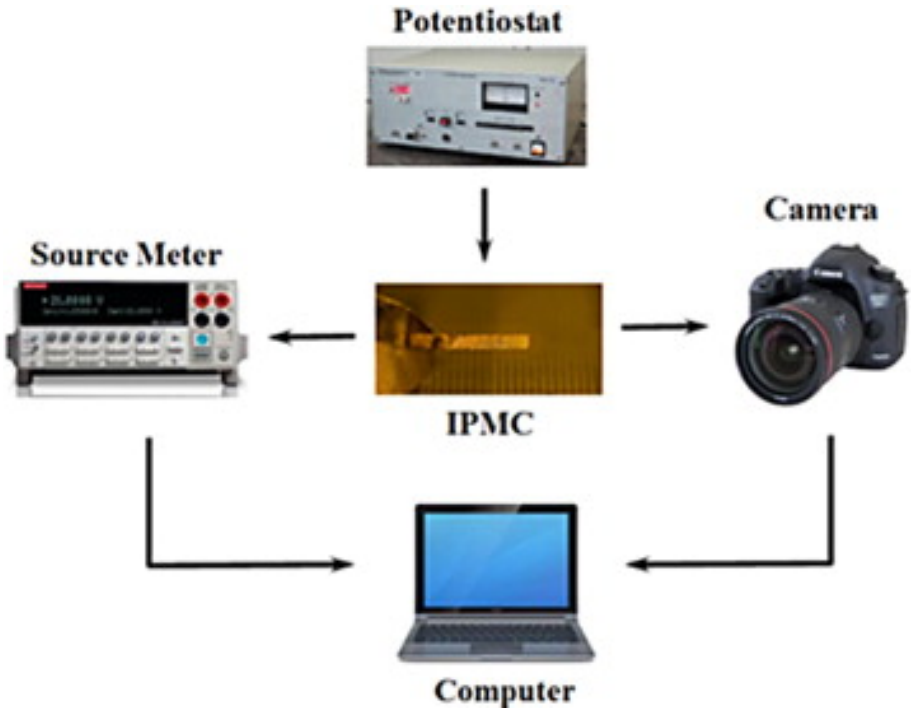

Figure 6.13: Experimental set-up for measuring the current and bending displacement of IPCNC actuator.

6.4.1 Mechanical parameter identification

There are four parameters in the mechanical model of the actuator: actuator's equivalent elastic modulus, density, damping and charge to stress ratio. To obtain the actuator's equivalent elastic modulus, the elastic modulus of each layer can be measured experimentally, using a setup specifically designed to measure the elastic modulus of soft materials. Details of the setup and procedures are presented in our previous work [39]. The equivalent flexural rigidity (El) of the actuator can be defined based on the elastic modulus and thickness of each layer [172].

$$EI = \frac{2b}{3}[E_1 h_1^3 + E_2(h_2^3 - h_1^3) + E_3(h_3^3 - h_2^3)] \tag{6.43}$$

where E_1, E_2, and E_3 are the elastic modulus of the Nafion film, the CNC layer, and the gold electrode respectively. The fundamental natural frequency of the actuator can be used to estimate the equivalent density of the actuator. Linear RFE model can be employed to obtain the natural frequency of the actuator. Recalling the fact that the linear RFE model converge to the linear EulerBernoulli beam model [193], the equivalent density of the actuator is defined

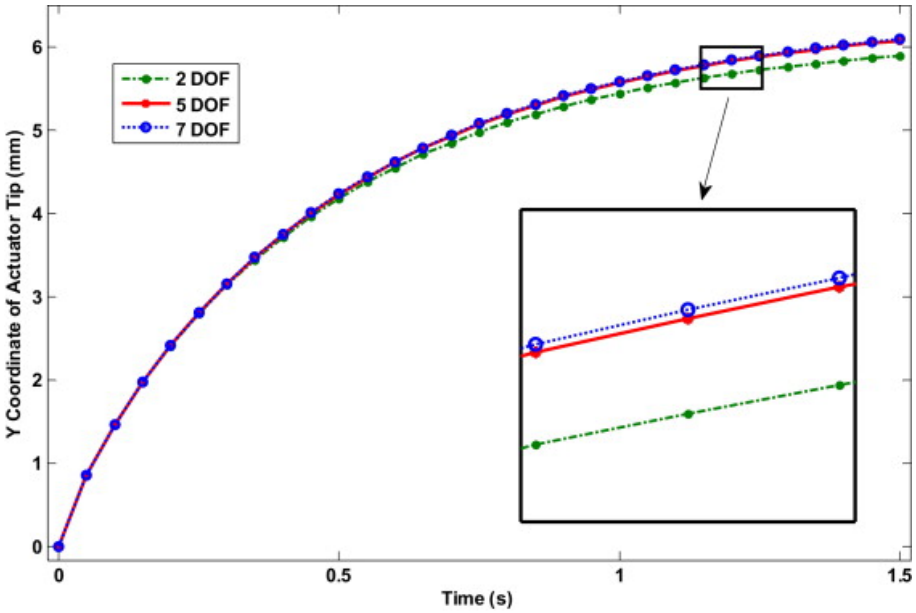

Figure 6.14: Convergence of the theoretical model for Y coordinate of the actuator tip.

as:

$$\rho = 1.875^4 \frac{EI}{2bh_3L^4(2\pi f)^2} \tag{6.44}$$

where f is the fundamental natural frequency of the actuator. Table 6.4 shows the convergence of the RFE model to the linear EulerBernoulli beam model in prediction of the fundamental natural frequency of the actuator.

Table 6.4: Convergence of the RFM to linear EulerBernoulli beam model.

	Linear RFM model (3 DOF)	Linear RFM model (5 DOF)	Linear RFM model (7 DOF)	Linear Euler-Bernoulli beam model
Fundamental natural frequency (Hz)	18.98	18.67	18.58	18.50

Free vibration test was performed to estimate the equivalent damping constant of the actuator. The logarithmic decrement (δ) and the damping ratio (ξ) can be define as [196]

$$\delta = \frac{1}{n} ln(\frac{a_i}{a_{i+1}}), \quad \xi = \sqrt{\frac{\delta^2}{4\pi^2 + \delta^2}} \tag{6.45}$$

where, (n) is the number of cycles, and (a_i) is the amplitude of the actuator bending displace-

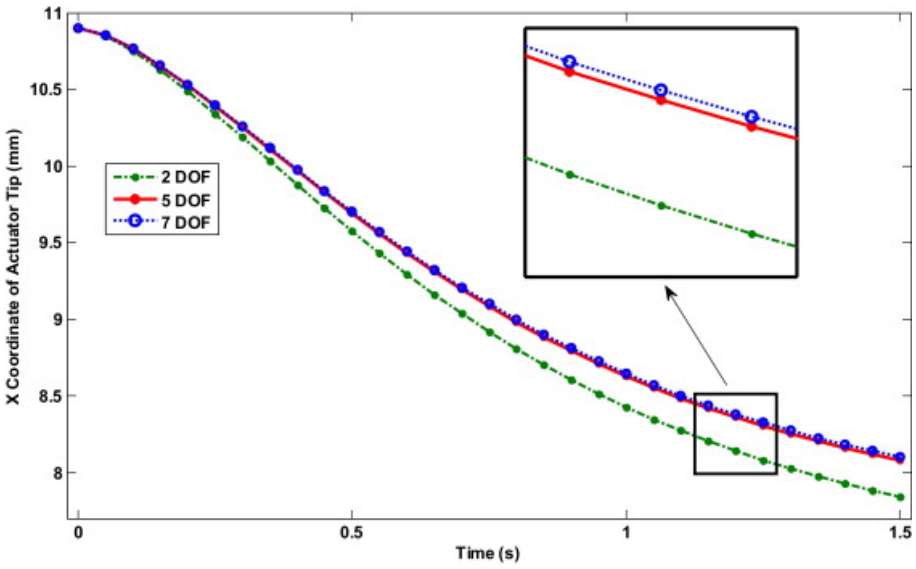

Figure 6.15: Convergence of the theoretical model for X coordinate of the actuator tip.

Table 6.5: Values of physical parameters for mechanical model.

$E_1(MPa)$	50
$E_1(MPa)$	739
$E_3(GPa)$	20
$E(MPa)$	538.4857
$f(Hz)$	18.5
$\rho(kg/m^3)$	2088.6
ξ	0.0228
$\eta(Pa \cdot s)$	2.11×10^5
$a(J/C)$	0.0053

ment in the ith cycle. Moreover, the equivalent damping constant is defined as

$$\eta = \frac{E\xi}{\pi f} \tag{6.46}$$

Finally, as the last parameter of the mechanical model, stress to charge ratio (α) was estimated from the experimental bending displacement of the actuator. Table 6.5 shows the values of the physical parameter for the mechanical model.

6.4.2 Model sensitivity analysis

The sensitivity of the model can be studied based on the number of elements that are used in the RFE model. For this purpose three different cases with 2, 5 and 7 DOF are

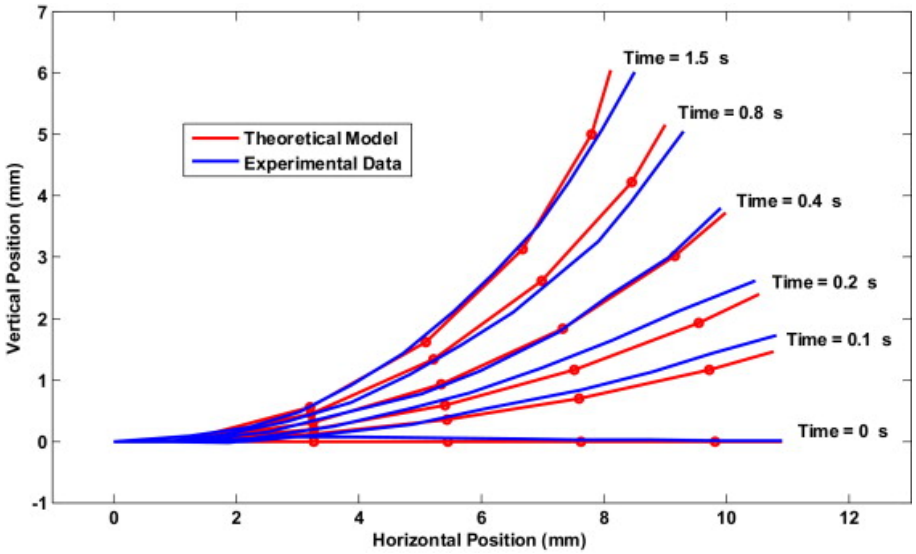

Figure 6.16: Comparison of the results produced by the theoretical model against the experimental bending displacement of the actuator in response to the step input voltage.

considered. Figure 6.14 and 6.15 show the convergence of X, and Y coordinates of the actuator tip in response to the step input voltage. From the data presented in these figures, it was deduced that the theoretical model converges as the number of elements increases. However, the increase of elements amplifies the computational load. Thus, a model with 5 DOF which shows an approximate convergence was utilized for numerical simulations.

6.4.3 Validation of the RFE model

Figure 6.16 shows a comparison of the simulated model with five degrees of freedom and experimental bending displacements of the IPCNC actuator under a 3.5 V step input voltage. It can be seen that the presented theoretical model is significantly accurate in predicting large bending deformation of the actuator. Moreover, the simulated and experimental data corresponding to the actuators tip displacement were employed to further validate the model.

Figure 6.17 and 6.18 compare X, and Y coordinate of the actuator tip in response to the step input voltage. It can be observed that the experimental data significantly confirm the simulation results. Since the proposed model predicts uniform curvature along the actuator length, the deviation in the X coordinate of the actuator tip suggests that both the actuation force and the curvature decrease along the length of the actuator. Having said that, the experimental data

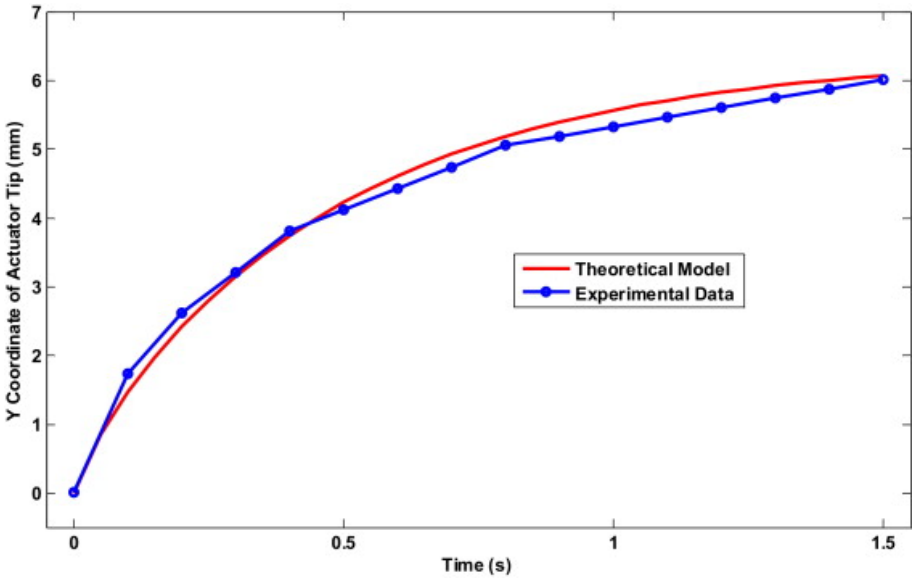

Figure 6.17: Comparison of the results produced by the theoretical model with the experimental Y coordinate of the actuator tip in response to the step input voltage.

in our previous works [39] and [4], shows that the IPCNC actuators bend with almost uniform curvature along their length (circular curve). Thus, the deviation in the X coordinate of the actuator tip may be due to the imperfections in gold coating of the investigated sample.

6.5 Discussions

As described in Section 6.1, the development of practical and accurate models for IPCNC actuators has a key role in the design and fabrication of functional devices employing these actuators. The proposed model in the current work is distinguished from the existing models reported in the literature in the sense that not only it has a simple structure, but also it can effectively predict the electrical admittance, mechanical dynamics and large deformation of the IPCNC actuators. The effectiveness of the electrical model is due to the proper combination of lumped resistor elements with the RC transmission model which significantly simplifies the derivation of the admittance model and identification of its parameters.

Whilst most of the existing works on modeling of IPCNC actuators are based on the linear EulerBernoulli beam model [184, 185, 186] and [187] due to its simplicity, this model cannot take into account large deformation of the actuators. To demonstrate the inability of this model in

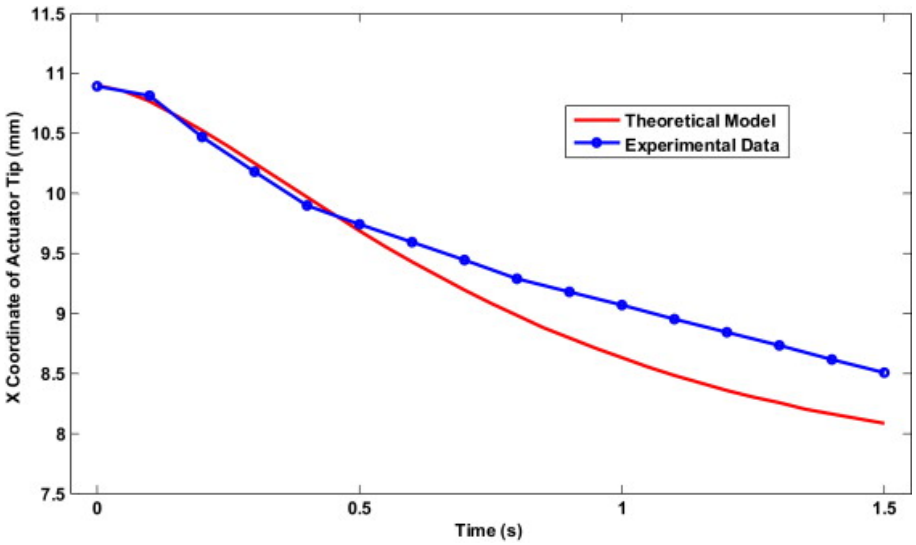

Figure 6.18: Comparison of the results produced by the theoretical model with the experimental X coordinate of the actuator tip in response to the step input voltage.

prediction of large deformation of the actuators, we have modeled the bending displacement of an actuator by using both the linear Euler-Bernoulli beam model and the proposed RFE model. Figure 6.19 shows the comparison of these two models for a 3.5 V step input voltage. It can be seen that the linear Euler-Bernoulli beam fails to predict the large bending deformation of the beam, whereas the RFE model with only 5 elements can effectively predict the large bending deformation. Moreover, the actuator's tip displacement data can be employed to compare these models. As the linear Euler-Bernoulli beam model cannot produce the displacement in X direction, only Y coordinate of the actuator tip was used in the simulation.

Figure 6.20 compares Y coordinate of the actuator tip in response to the step input voltage. It can be observed that while for the case of relatively small bending deformation both models produce the same bending displacement, for the case of large bending deformation the prediction of the linear Euler-Bernoulli beam model deviates from that of the RFE model where the linear Euler-Bernoulli beam model incorrectly produces a greater bending displacement.

6.6 Conclusion

In this paper, an effective nonlinear dynamic model for an analysis of the large bending deformation of IPCNC actuators has been proposed. The model consists of two separate electrical

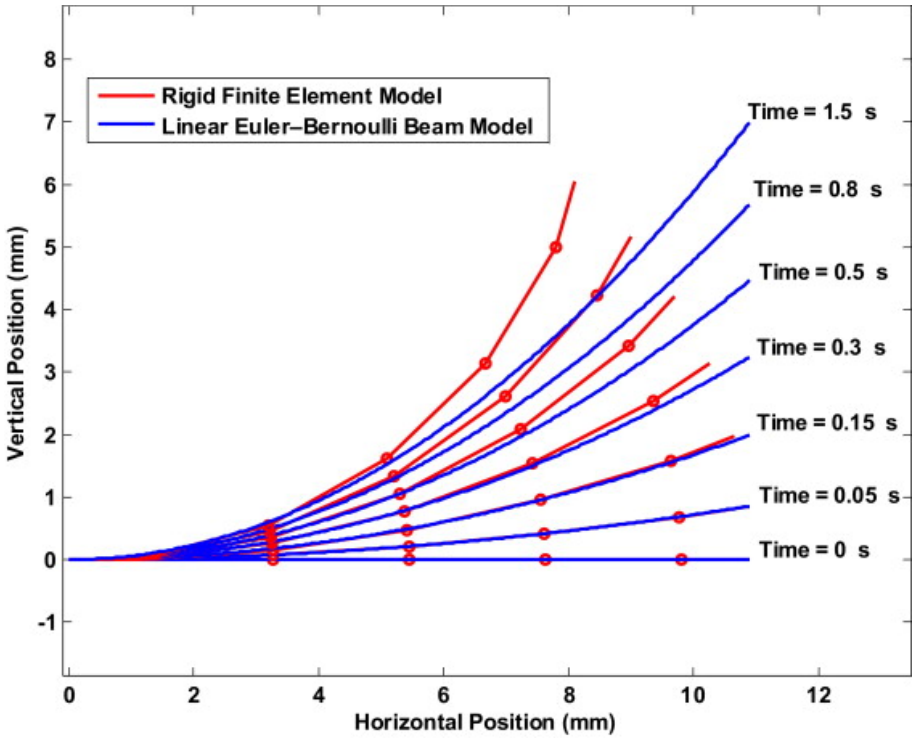

Figure 6.19: Comparison of the linear Euler-Bernoulli beam model and the RFE model in prediction of bending displacement of the actuator in response to the step input voltage.

and mechanical components and establishes a mathematical relation between the input voltage and the output bending displacement of the actuators. The core in the electrical component is the integration of lumped resistor elements and RC transmission line model, with both electrolyte and shunt resistances being assumed as lumped parameter elements. The mechanical component, however, relates the stored charges to the bending displacement through considering the polymer actuator as a discretized system connected by springdamping elements (SDEs). The employed RFE method has simplified the modeling of the large bending deformation of the actuator. The modeling technique based on RFE provides a unified approach to analyze micro robotic systems which consist of both flexible polymer links and rigid links. This important feature, will enhance the design and modeling of functional devices based on conductive polymer actuators. The proposed model can be considered as a step forward toward understanding the large deformation dynamic behavior of IPCNC actuators based on their physical parameters. It should be noted that the proposed modeling strategy can be simply extended to

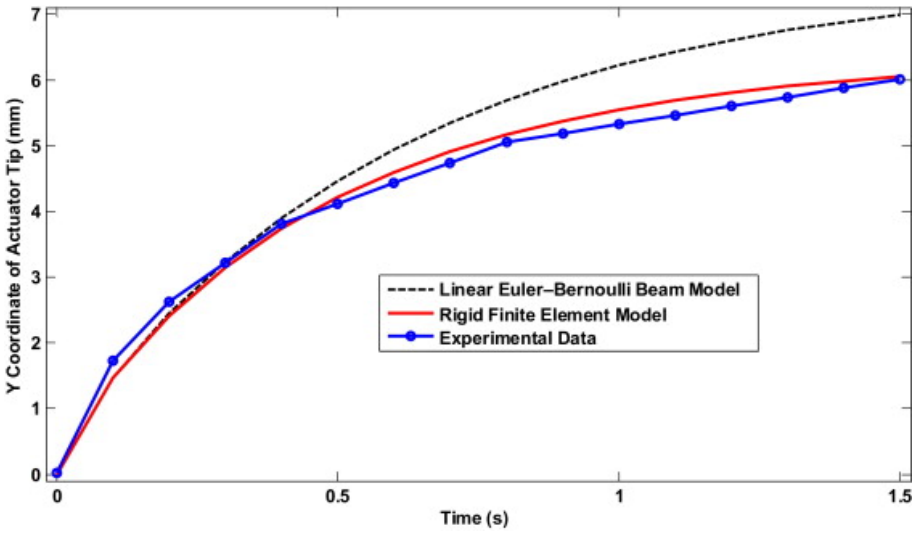

Figure 6.20: Comparison of the linear Euler-Bernoulli beam model and the RFE model in prediction of Y coordinate of the actuator tip.

other polymer actuators such as conjugated polymer actuators with some modifications in the electrical dynamic model. A comparison of the simulation results and experimental results of the IPCNC actuator strongly indicates that the model has been successful in predicting large bending deformation of the actuator.

CHAPTER 7. GENERAL CONCLUSIONS

This dissertation has focused on design, fabrication, characterization and simulation of IEAP actuators and sensors (mostly on actuators). It is focused on each main component of IEAP actuators and sensors and its contribution to the functionality, with the goal to study the mechanism of IEAP devices and improve the final performance. I will discuss more specifically about how each component contributes to the functionality of the final device in the following sections. In the last section some ideas and suggestions for future studies are presented.

7.1 Contribution of CNC Nanocomposites on IEAP Sensor

IEAP sensor, also known as IPMC sensor, demonstrates a strong dependence on the nanostructure and morphology of its CNC nanocomposites. In this work LbL self-assembly technique was adopted to build up the CNC layers. Control over the CNC fabrication process by adjusting the ionic strength of polycation PAH and the number of deposited bilayers provides an effective means to enhance and optimize the sensitivity of IPMC mechanoelectric sensors.

Ionic strength of the ionic species is the key to control the nanostucture achieved by LbL deposition process. With the addition of small molecular salts such as NaCl, some fraction of the ionic charge distributed among the polymer chains will be neutralized. As a result, the polymer backbone will change its morphology from long chains to a more curl and globular conformation due to the reduced electrostatic repulsion. Layers deposited from ionic species with higher ionic strength tend to be thicker and more porous due to the globular conformation of polymer chains. It was observed that with the addition of NaCl in PAH solution, the achieved IPMC sensor demonstrated an enhanced sensitivity by at least 3 to 4 folds. However, a decline of the generated electric signal was observed over the first hundreds of cycles before

the stabilization, indicating an unstable functionality of the set of specimens, most probably due to the inner mechanical failure of the sensors. Exploration of effective techniques to reduce the stabilization time will be involved in the future work.

7.2 Contribution of CNC Patterns on IEAP Actuator

Besides control over the generated strain, CNC layers existing in IEAP actuators also enable different actuation patterns. Instead of a circular bending from an IEAP actuator consisting of a homogeneous CNC nanocomposites, an angular deformation is generated by the modified IEAP actuator, whose CNC nanocomposites are designed and fabricated with specific patterns.

Experimental observation indicates that the incorporation of conjugated polymer, PEDOT:PSS patterns allows control over ion permeability through the thickness of the actuators as a whole. With the desired PEDOT:PSS patterns casted on the surface of Nafion, IEAP actuator demonstrates an angular deformation with sharp angles.

FEM was used to simulate this angular deformation and further explore the interactions between the ions and PEDOT:PSS layers. It is proved that the contribution to the ion permeability through the PEDOT:PSS layer is highly dependent on the number of deposited layers. If PEDOT:PSS layer is casted on either side of Nafion ionomeric membrane, ions from ILs are more likely to penetrate the layer and accumulated at the surface of the external electrodes. If PEDOT:PSS layer is casted on each side of Nafion, however, ions from ILs will stay in their initial area, that is, most of them won't drift to the electrode's surface. FEM results also indicate that around half amount of the ions from ILs contribute to the actuation.

This intrinsic angular bending makes it possible for IEAP actuators to be implemented in soft robotic applications due to their biomimetic angular limb-like deformation. A systematic study based on the interaction mechanism, dynamic modeling and more explorations on its practical applications would be the next stage of this work.

7.3 Contribution of IL Concentration on IEAP Actuator

The influence of IL concentration on the electromechanical response of IEAP actuators has been investigated. Electrical impedance results suggest that the addition of IL results in the reduction of solution resistance, which is in agreement with expected effect of any ion-rich electrolyte.

Equivalent circuit with Warburg element representing the ion diffusion contributions was used in this work to model the electrochemical behavior of the system. A more capacitor-like behavior is observed with the addition of ILs in the system.

Electromechanical results indicate that the optimum concentration in which the actuation response is maximized, however, does not occur at the highest ion concentration. With the addition of ILs, the generated strain keeps increasing until the ILs uptake reaches around 22 wt%; after that the strain drops. The optimum concentration ($\sim$ 22 wt%) implies a formation of a saturated ion layer at outer electrode interfaces. As the ILs concentration, extra layers are formed at the edge and grow inward toward the center of the system, which, in turn, will reduce the strain generated. This observation provides an effective approach in fabrication of IEAP actuators to achieve the best functionality.

7.4 Contribution of Ionomeric Membrane on IEAP Actuator

In IEAP actuator, not just the charged ions provided by the dopant (ILs or aqueous electrolyte), but also the counterions of the ionomeric membranes are mobilized under electric stimulation. When under a fixed electric stimulation, different electromechanical responses were observed of IEAP actuators consisting of Nafion ionomeric membranes with different counterions.

Before soaked in the desired IL to uptake $\sim$ 40 wt% of their dry weight, ion-exchange process was performed to exchange proton counterions of Nafion with larger cations (Zn^+, Na^+ and EMI^+). IEAP actuators consisting of Nafion with exchanged counterions were fabricated and tested. The magnitude of the maximum cationic strain generated by the corresponding IEAP actuator increases with the van der Waals volume of the exchanged counterions. That is,

the actuator consisting of Nafion with H^+ counterion shows the smallest cationic strain, while the actuator consisting of Nafion with EMI^+ counterion generates the largest cationic strain.

The full electromechanical response of two actuators consisting of Nafion with counterions H^+ and EMI^+ (the two extreme cases) were also investigated and compared. Three different ILs, EMI-Tf, TES-TFSI, and BMP-TFSI were adopted. In all cases, after exchanging H^+ with EMI^+ ions, the overall response was shifted toward cationic strain, suggesting the contribution of the counterions to the net strain.

As suggested by the experimental results, when under an applied electric voltage, the counterions of Nafion also diffuse and drift through the interconnected channels of the polymeric backbone structure. The larger van der Waals volume the counterions have, the larger contribution to the cationic strain they have.

This work helps to draw a clear conclusion on the ion mobility through Nafion ionomeric membrane in the presence of an electric stimulus. The contribution of the generated strain is not only from the ions provided by the dopant, but also from the counterions of Nafion ionomeric membrane.

7.5 Nonlinear Dynamic Modeling of IEAP Actuator

A nonlinear dynamic modeling is presented to effectively predict the IEAP actuators' dynamic behavior by using rigid finite element method. This work was in collaboration with Professor Kouzani and his research group at the Deakin University in Australia. The model provides a thorough understanding and a theoretical support to the IEAP actuators fabricated and studied in this dissertation.

7.6 Future Studies

One recommendation for future work is to further study the mechanism of IEAP stress sensor. While quit a few publications from us and others have studied IEAP actuators, the papers considering IEAP sensors are quite fewer, especially IEAP sensors doped with IL. The work presented in Chapter 2 is still in its infancy, and further studies need to be conducted.

For example, explore the ions mobility and chemical/electrostatic interactions of ions under a mechanical stimulus, the reason of the declining electric signal, and the effective ways to reduce the stabilization time for these sensors.

Another interesting topic to consider for future studies is to conduct a systematic study based on the patterned IEAP actuators discussed in Chapter 5. These soft actuators with their unique behavior are most suitable for microrobotic applications. The angular deformation generated in these actuators is intrinsic, hence the actuators can be made in very small dimensions. More comprehensive works are necessary based on a large variety of conductive materials (not just limited to polymers), ILs, and the designed patterns. These proposed set of works, plus the work presented in this dissertation, would provide a clear picture for the potentially wide applications of these unique actuators.

The last recommendation is to establish a proper mathematical model to predict the dynamic behavior of the patterned IEAP actuators developed in Chapter 5. So far we have developed a static model to verify the proposed hypothesis and further explore the interactions between the ions and incorporated conjugated polymer. However, this static model lacks the ability to predict the actuator's dynamic behavior. Due to its unique structures and inhomogeneous deformation, previously proposed models on circular IEAP actuators are hardly applicable. Therefore, developing a proper model that could effectively predict the dynamic behavior of this angular actuator would be a challenging but meaningful study.

APPENDIX A. PROCEDURES OF FINITE ELEMENT MODELING

Detailed finite element modeling (FEM) procedures are presented in this chapter.

Morphological and mechanical properties

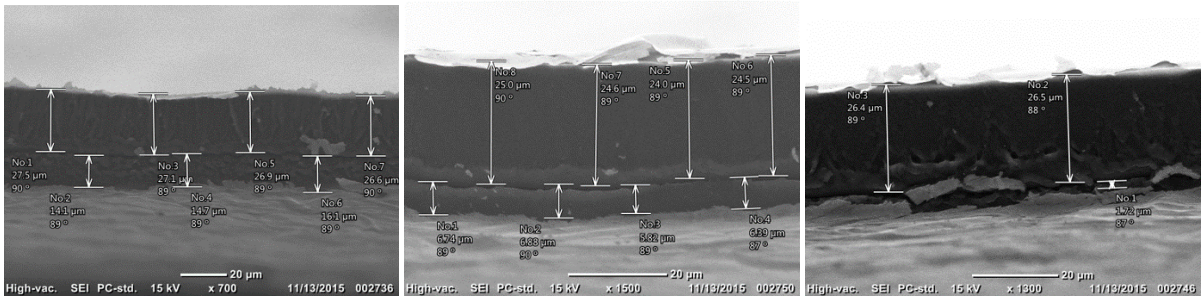

(a) (b) (c)

Figure A.1: SEM images of specimen Nafion/1s-PEDOT:PSS/Au, from middle point to edge ((a) - (c)) of PEDOT:PSS layer.

Figure A.1a – A.1c show a wedge-shaped thickness profile of the casted PEDOT:PSS layer. Similar to a trapezoid, the highest concentration is in the center, and gradually tapers off along the edge, due to the imperfect fabrication process of the simple drop-casting technique.

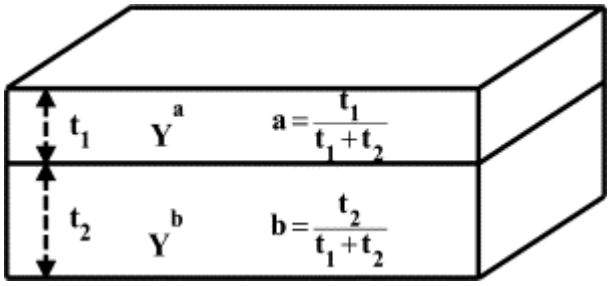

Figure A.2: Schematic of a bilayer laminate for the characterization of the elastic modulus of individual layer[4].

For the bilayer laminate with much larger length respect to its width and thickness, the elastic modulus of each layer can be deducted as described by Liu *et al.* previously[4]. Figure A.2 illustrates a bilayer laminate with the length much larger than the other dimensions. The elastic modulus of the entire structure Y^e is dependent on the elastic modulus of each layer Y^a and Y^b as

$$Y^e = aY^a + bY^b \tag{A.1}$$

where a and b are the volume fractions of the corresponding layer in the laminate structure[4].

The thickness of the each layer is read from the SEM images; average value from the middle point to the edge of the PEDOT:PSS layer was taken for the average thickness. Three tensile tests were conducted to take the average value. The elastic modulus of each component measured, deduced or read from other literatures is listed in Table A.1, with the corresponding Poisson's ratio listed in the next column.

Table A.1: The thickness of each layer in IEAP actuator and its physical properties.

Sample	Layer	Thickness (μm)	Elastic Modulus (MPa)	Poisson's Ratio
Nafion/1s-PEDOT:PSS	overall	40.2	20.7	
	Nafion	28.6	27.3	0.487[197, 198]
	PEDOT:PSS	11.6	4.3	0.33[199]
Nafion/1s-PEDOT:PSS/Au	gold leaf	0.05	20,000[4]	0.42[200]

Simulation of electromechanical response by FEM

FEM is performed to model the electromechanical response of IEAP actuators with different patterns. The mechanical deformation is modeled by ABAQUS finite element code. Due to the pretty small width of the IEAP actuator (1 mm), the normal stress and the shear stresses directed perpendicular to the plane in which the bending occurs are assumed to be zero. As a result, the 3–D configuration of IEAP actuator can be reasonably approximated as a 2–D plane stress configuration in the preprocessing module, with a 4–node bilinear plane stress quadrilateral (CPS4R) element for the analysis. Moreover, SEM images reveal a non-uniform distribution of PEDOT:PSS layer, whose highest concentration is in the center, and gradually

tapers off along the edge. A trapezoid–like geometry is used to represent the PEDOT:PSS pattern. Materials' properties and geometric information are from Table A.1. Tie constraint is employed to model the surface contact with gold electrode as master surface and Nafion with PEDOT:PSS pattern as slave surface, with the assumption that no relative displacement happened due to the hot-pressed bonding. The boundary condition of ENCASTRE ($U_1 = U_2 = U_3 = UR_1 = UR_2 = UR_3 = 0$) is adopted at one end of the model to represent the mechanically fixed end of the actuator.

The actuation response of IEAP actuators with ions from EMI-Tf is caused by the accumulation and depletion of excess charges at the electrodes under an applied voltage, which is equivalent to a thermal bimorph in mechanism. Nafion membrane is divided into four layers along the thickness evenly. The layer connected to cathode and anode are referred to as Nafion/cat and Nafion/ani, respectively. These two layers are used to simulate the expansion and contraction due to ions accumulation and depletion at different electrodes. The other two layers located in the middle are named by Nafion/neu, to simulate the ions depletion during the actuation process. A consistent isotropic thermal coefficient α_L is applied to each main component, and temperature field is used to control the deformation of each layer. In ABAQUS the definition of the isotropic thermal coefficient α_L is the ratio of change in length (ΔL) to the total starting length (L) and change in temperature (ΔT), with the expression as $\Delta L/L = \alpha_L \times \Delta T$. The change in area of the 2–D plane cross-section due to thermal expansion is $\Delta A = hl \times (1 + \alpha_L \Delta T)^2 - hl \approx 2hl \cdot \alpha_L \Delta T$ if we exclude the higher orders due to the pretty small value of α_L. As a result, the change in area (ΔA) caused by thermal expansion/contraction is linear to the change in temperature (ΔT). Same approximation is also applicable to the change in volume (ΔV).

Define N as the total amount of cations drifted in the cationic response of actuation. Following paragraphs introduce the detailed procedures and their theoretical support.

1. Actuator 1S

   (a) Cationic response: N cations are drifted from Nafion/neu and Nafion/ani layers homogeneously, and accumulated in PEDOT:PSS layer (attached to cathode) and

Nafion/cat layer with volume ratio of 2:1.

(b) Anionic response: N anions/anionic clusters are drifted and stored in Nafion/ani layer from Nafion/cat and Nafion/neu layers homogeneously. The cations stored in PEDOT:PSS layer (attached to cathode) in previous cationic response won't move out during the anionic response.

The procedures adopted in actuator 1S are based on the observation of a non-ignorable expansion from PEDOT:PSS layer when it only exists on the convex side of Nafion. Meanwhile, IEAP actuator with bare Nafion also displays a noticeable bending, indicating ions accumulation at the outer layers of Nafion and depletion at the inner layers at the same time[40, 4]. In addition, PEDOT:PSS layer does not contain any ions at the very beginning, thus it won't show any contraction during the simulation.

2. Actuator 2SA

- Cationic response: N cations are drifted from Nafion/neu and Nafion/ani layers homogeneously, and accumulated in PEDOT:PSS layer (attached to cathode) and Nafion/cat layer with volume ratio of 2:1.
- Anionic response: N anions/anionic clusters are drifted from Nafion/neu and Nafion/cat homogeneously. Then, (i) part of the anions/anionic clusters are stored in PEDOT:PSS layer (attached to anode) with the same volume density of the cations in PEDOT:PSS layer (attached to cathode) in the previous cationic response, and (ii) remaining anions/anionic clusters are accumulated in Nafion/ani layer.

The procedures adopted in the simulation of actuator 2SA are based on the same reason with part 1.

3. Actuator 2SS

Actuator 2SS differs remarkably from actuator 1S and 2SA. There are five segments along the length, with 3 segments made of Nafion/2s-PEDOT:PSS and 2 segments made of BNafion. Due to their significant difference in electrochemical and electromechanical responses, a segment-wise procedure is employed as below:

- Cationic response: in each segment made of BNafion, $n(= N/5)$ cations are drifted from Nafion/neu and Nafion/ani layers homogeneously, and accumulated in Nafion/cat layer. In each segment made of Nafion/2s-PEDOT:PSS, $n/8$ cations are drifted from Nafion/neu and Nafion/ani layers homogeneously, then accumulated in PEDOT:PSS layer and Nafion/cat layer with volume ratio of 2:1.
- Anionic response: in each segment of BNafion, n anions/anionic clusters are drifted and stored in Nafion/ani layer from Nafion/cat and Nafion/neu layers homogeneously. In each segment made of Nafion/2s-PEDOT:PSS, $n/8$ anions/anionic clusters are drifted from Nafion/neu and Nafion/cat homogeneously. Then, (i) part of the anions/anionic clusters are drifted and stored in PEDOT:PSS layer (attached to to anode) with the same volume density of the cations stored in PEDOT:PSS layer (attached to cathode) in the previous cationic response, and (ii) remaining anions/anionic clusters are accumulated in Nafion/ani layer.

The procedures adopted in actuator 2SS are based on the observation from the equivalent circuit modeling. Specimen Nafion/2s-PEDOT:PSS reveals a much smaller EDL capacitance (0.12 μF) at the electrode surface when compared to the specimen BNafion (2.86 μF). As a result, BNafion and Nafion/2s-PEDOT:PSS are treated differently for a best match of the experimental results.

From the equivalent circuit modeling, the ratio of EDL capacitance of specimen Nafion/2s-PEDOT:PSS and specimen BNafion is $0.12/2.86 = 0.04$, while from the simulation procedures above, this ratio becomes $1/8 = 0.125$, in order to fully match the experimental results. It suggests the complexity to quantify the ions/ion clusters motion during the actuation. However, all the procedures made above is consistent with our previous electrochemical and electromechanical responses, and fully respect to the conclusions in earlier works[40, 38, 4, 37].

BIBLIOGRAPHY

[1] R. Montazami, *Smart Polymer Electromechanical Actuators for Soft Microrobotic Applications*. PhD thesis, Virginia Polytechnic Institute and State University, 2011.

[2] P. Millet, R. Durand, E. Dartyge, G. Tourillon, and A. Fontaine, "Precipitation of metallic platinum into nafion ionomer membranes i. experimental results," *Journal of the Electrochemical Society*, vol. 140, no. 5, pp. 1373–1380, 1993.

[3] B. J. Akle, M. D. Bennett, D. J. Leo, K. B. Wiles, and J. E. McGrath, "Direct assembly process: a novel fabrication technique for large strain ionic polymer transducers," *Journal of Materials Science*, vol. 42, no. 16, pp. 7031–7041, 2007.

[4] S. Liu, R. Montazami, Y. Liu, V. Jain, M. Lin, X. Zhou, J. R. Heflin, and Q. Zhang, "Influence of the conductor network composites on the electromechanical performance of ionic polymer conductor network composite actuators," *Sensors and Actuators A: Physical*, vol. 157, no. 2, pp. 267–275, 2010.

[5] M. Shahinpoor and K. J. Kim, "Ionic polymer-metal composites: I. fundamentals," *Smart materials and structures*, vol. 10, no. 4, p. 819, 2001.

[6] K. J. Kim and M. Shahinpoor, "Ionic polymer–metal composites: Ii. manufacturing techniques," *Smart materials and structures*, vol. 12, no. 1, p. 65, 2003.

[7] M. Shahinpoor and K. J. Kim, "Ionic polymer–metal composites: Iii. modeling and simulation as biomimetic sensors, actuators, transducers, and artificial muscles," *Smart materials and structures*, vol. 13, no. 6, p. 1362, 2004.

[8] M. Shahinpoor and K. J. Kim, "Ionic polymer–metal composites: Iv. industrial and medical applications," *Smart materials and structures*, vol. 14, no. 1, p. 197, 2004.

[9] C. Bonomo, P. Brunetto, L. Fortuna, P. Giannone, S. Graziani, and S. Strazzeri, "A tactile sensor for biomedical applications based on ipmcs," *Sensors Journal, IEEE*, vol. 8, no. 8, pp. 1486–1493, 2008.

[10] E. Mbemmo, Z. Chen, S. Shatara, and X. Tan, "Modeling of biomimetic robotic fish propelled by an ionic polymer-metal composite actuator," in *Robotics and Automation, 2008. ICRA 2008. IEEE International Conference on*, pp. 689–694, IEEE, 2008.

[11] B. Kim, D.-H. Kim, J. Jung, and J.-O. Park, "A biomimetic undulatory tadpole robot using ionic polymer–metal composite actuators," *Smart materials and structures*, vol. 14, no. 6, p. 1579, 2005.

[12] B. J. Akle, M. D. Bennett, and D. J. Leo, "High-strain ionomeric–ionic liquid electroactive actuators," *Sensors and Actuators A: Physical*, vol. 126, no. 1, pp. 173–181, 2006.

[13] R. Montazami, D. Wang, and J. R. Heflin, "Influence of conductive network composite structure on the electromechanical performance of ionic electroactive polymer actuators," *International Journal of Smart and Nano Materials*, vol. 3, no. 3, pp. 204–213, 2012.

[14] D. Pugal, K. Jung, A. Aabloo, and K. J. Kim, "Ionic polymer–metal composite mechano-electrical transduction: review and perspectives," *Polymer international*, vol. 59, no. 3, pp. 279–289, 2010.

[15] W. Hong, A. Almomani, and R. Montazami, "Influence of ionic liquid concentration on the electromechanical performance of ionic electroactive polymer actuators," *Organic Electronics*, vol. 15, no. 11, pp. 2982–2987, 2014.

[16] W. Hong, C. Meis, J. R. Heflin, and R. Montazami, "Evidence of counterion migration in ionic polymer actuators via investigation of electromechanical performance," *Sensors and Actuators B: Chemical*, vol. 205, pp. 371–376, 2014.

[17] A. A. A. Moghadam, W. Hong, A. Kouzani, A. Kaynak, R. Zamani, and R. Montazami, "Nonlinear dynamic modeling of ionic polymer conductive network composite actuators

using rigid finite element method," *Sensors and Actuators A: Physical*, vol. 217, pp. 168–182, 2014.

[18] W. Kuhn, B. Hargitay, A. Katchalsky, and H. Eisenberg, "Reversible dilation and contraction by changing the state of ionization of high-polymer acid networks," 1950.

[19] R. Hamlen, C. Kent, and S. Shafer, "Electrolytically activated contractile polymer," 1965.

[20] A. J. Grodzinsky, *Electromechanics of deformable polyelectrolyte membranes.* PhD thesis, Massachusetts Institute of Technology, 1974.

[21] A. J. Grodzinsky and J. R. Melcher, "Electromechanical transduction with charged polyelectrolyte membranes," *IEEE Transactions on Biomedical Engineering*, no. 6, pp. 421–433, 1976.

[22] M. Shahinpoor, "Conceptual design, kinematics and dynamics of swimming robotic structures using ionic polymeric gel muscles," *Smart Materials and Structures*, vol. 1, no. 1, p. 91, 1992.

[23] D. B. Adolf, M. Shahinpoor, D. J. Segalman, and W. R. Witkowski, "Electrically controlled polymeric gel actuators," Oct. 5 1993. US Patent 5,250,167.

[24] M. Shahinpoor, "Microelectro-mechanics of ionic polymeric gels as artificial muscles for robotic applications," in *Robotics and Automation, 1993. Proceedings., 1993 IEEE International Conference on*, pp. 380–385, IEEE, 1993.

[25] M. Shahinpoor, "Continuum electromechanics of ionic polymeric gels as artificial muscles for robotic applications," *Smart Materials and Structures*, vol. 3, no. 3, p. 367, 1994.

[26] M. Shahinpoor and M. S. Thompson, "The venus flytrap as a model for a biomimetic material with built-in sensors and actuators," *Materials Science and Engineering: C*, vol. 2, no. 4, pp. 229–233, 1995.

[27] M. Mojarrad and M. Shahinpoor, "Ion exchange membrane-platinum composites as electrically controllable artificial muscles," in *3rd International Conference on Intelligent Materials*, pp. 1012–1017, International Society for Optics and Photonics, 1996.

[28] M. Mojarrad and M. Shahinpoor, "Biomimetic robotic propulsion using polymeric artificial muscles," in *Robotics and Automation, 1997. Proceedings., 1997 IEEE International Conference on*, vol. 3, pp. 2152–2157, IEEE, 1997.

[29] M. Shahinpoor and M. Mojarrad, "Soft actuators and artificial muscles," Aug. 29 2000. US Patent 6,109,852.

[30] M. Shahinpoor and K. J. Kim, "The effect of surface-electrode resistance on the performance of ionic polymer-metal composite (ipmc) artificial muscles," *Smart Materials and Structures*, vol. 9, no. 4, p. 543, 2000.

[31] S. Nemat-Nasser and Y. Wu, "Comparative experimental study of ionic polymer–metal composites with different backbone ionomers and in various cation forms," *Journal of Applied Physics*, vol. 93, no. 9, pp. 5255–5267, 2003.

[32] Y. Bar-Cohen, S. P. Leary, M. Shahinpoor, J. S. Harrison, and J. G. Smith, "Flexible low-mass devices and mechanisms actuated by electroactive polymers," in *1999 Symposium on Smart Structures and Materials*, pp. 51–56, International Society for Optics and Photonics, 1999.

[33] S. Nemat-Nasser, S. Zamani, and Y. Tor, "Effect of solvents on the chemical and physical properties of ionic polymer-metal composites," *Journal of Applied Physics*, vol. 99, no. 10, p. 104902, 2006.

[34] M. Shahinpoor and K. J. Kim, "Fully dry solid state artificial muscles exhibiting giant electromechanical effect," in *SPIE's 8th Annual International Symposium on Smart Structures and Materials*, pp. 428–435, International Society for Optics and Photonics, 2001.

[35] M. Shahinpoor and K. J. Kim, "Solid-state soft actuator exhibiting large electromechanical effect," *Applied physics letters*, vol. 80, no. 18, pp. 3445–3447, 2002.

[36] M. D. Bennett and D. J. Leo, "Ionic liquids as stable solvents for ionic polymer transducers," *Sensors and Actuators A: Physical*, vol. 115, no. 1, pp. 79–90, 2004.

[37] Y. Liu, R. Zhao, M. Ghaffari, J. Lin, S. Liu, H. Cebeci, R. G. de Villoria, R. Montazami, D. Wang, and B. L. Wardle, "Equivalent circuit modeling of ionomer and ionic polymer conductive network composite actuators containing ionic liquids," *Sensors and Actuators A: Physical*, vol. 181, pp. 70–76, 2012.

[38] Y. Liu, S. Liu, J. Lin, D. Wang, V. Jain, R. Montazami, J. R. Heflin, J. Li, L. Madsen, and Q. Zhang, "Ion transport and storage of ionic liquids in ionic polymer conductor network composites," *Applied Physics Letters*, vol. 96, no. 22, p. 223503, 2010.

[39] S. Liu, R. Montazami, Y. Liu, V. Jain, M. Lin, J. R. Heflin, and Q. Zhang, "Layer-by-layer self-assembled conductor network composites in ionic polymer metal composite actuators with high strain response," *Applied Physics Letters*, vol. 95, no. 2, p. 023505, 2009.

[40] R. Montazami, S. Liu, Y. Liu, D. Wang, Q. Zhang, and J. R. Heflin, "Thickness dependence of curvature, strain, and response time in ionic electroactive polymer actuators fabricated via layer-by-layer assembly," *Journal of Applied Physics*, vol. 109, no. 10, p. 104301, 2011.

[41] C. Meis, N. Hashemi, and R. Montazami, "Investigation of spray-coated silver-microparticle electrodes for ionic electroactive polymer actuators," *Journal of Applied Physics*, vol. 115, no. 13, p. 134302, 2014.

[42] J. Li, K. G. Wilmsmeyer, J. Hou, and L. A. Madsen, "The role of water in transport of ionic liquids in polymeric artificial muscle actuators," *Soft Matter*, vol. 5, no. 13, pp. 2596–2602, 2009.

[43] K. Sadeghipour, R. Salomon, and S. Neogi, "Development of a novel electrochemically active membrane and'smart'material based vibration sensor/damper," *Smart Materials and Structures*, vol. 1, no. 2, p. 172, 1992.

[44] M. Shahinpoor, "New effect in ionic polymeric gels: the ionic flexogelectric effect," in *Smart Structures & Materials' 95*, pp. 42–53, International Society for Optics and Photonics, 1995.

[45] C. Bonomo, L. Fortuna, P. Giannone, and S. Graziani, "A sensor-actuator integrated system based on ipmcs [ionic polymer metal composites]," in *Sensors, 2004. Proceedings of IEEE*, pp. 489–492, IEEE, 2004.

[46] C. Bonomo, L. Fortuna, P. Giannone, S. Graziani, and S. Strazzeri, "A resonant force sensor based on ionic polymer metal composites," *Smart Materials and Structures*, vol. 17, no. 1, p. 015014, 2007.

[47] C. Bonomo, L. Fortuna, P. Giannone, and S. Graziani, "A method to characterize the deformation of an ipmc sensing membrane," *Sensors and Actuators A: Physical*, vol. 123, pp. 146–154, 2005.

[48] C. Bonomo, L. Fortuna, P. Giannone, S. Graziani, and S. Strazzeri, "A model for ionic polymer metal composites as sensors," *Smart materials and structures*, vol. 15, no. 3, p. 749, 2006.

[49] K. M. Newbury, "Characterization, modeling, and control of ionic polymer transducers," 2002.

[50] K. M. Newbury and D. J. Leo, "Electromechanical modeling and characterization of ionic polymer benders," *Journal of Intelligent Material Systems and Structures*, vol. 13, no. 1, pp. 51–60, 2002.

[51] H. Lei, C. Lim, and X. Tan, "Modeling and inverse compensation of dynamics of base-excited ionic polymer–metal composite sensors," *Journal of Intelligent Material Systems and Structures*, p. 1045389X13478272, 2013.

[52] C. Lim, H. Lei, and X. Tan, "A dynamic physics-based model for base-excited ipmc sensors," in *SPIE Smart Structures and Materials+ Nondestructive Evaluation and Health Monitoring*, pp. 83400H–83400H, International Society for Optics and Photonics, 2012.

[53] C. L. Marx, D. F. Caulfield, and S. L. Cooper, "Morphology of ionomers," *Macromolecules*, vol. 6, no. 3, pp. 344–353, 1973.

[54] J. Kao, R. Stein, W. MacKnight, W. Taggart, and G. Cargill III, "Structure of the cesium salt of an ethylene-methacrylic acid copolymer from its radial distribution function," *Macromolecules*, vol. 7, no. 1, pp. 95–100, 1974.

[55] T. Gierke and W. Hsu, "The clusternetwork model of ion clustering in perfluorosulfonated membranes," 1982.

[56] D. R. Morris and X. Sun, "Water-sorption and transport properties of nafion 117 h," *Journal of applied polymer science*, vol. 50, no. 8, pp. 1445–1452, 1993.

[57] T. Okada, G. Xie, O. Gorseth, S. Kjelstrup, N. Nakamura, and T. Arimura, "Ion and water transport characteristics of nafion membranes as electrolytes," *Electrochimica Acta*, vol. 43, no. 24, pp. 3741–3747, 1998.

[58] T. Okada, S. Møller-Holst, O. Gorseth, and S. Kjelstrup, "Transport and equilibrium properties of nafion® membranes with h+ and na+ ions," *Journal of Electroanalytical Chemistry*, vol. 442, no. 1, pp. 137–145, 1998.

[59] N. Miyake, J. Wainright, and R. Savinell, "Evaluation of a sol-gel derived nafion/silica hybrid membrane for polymer electrolyte membrane fuel cell applications: Ii. methanol uptake and methanol permeability," *Journal of The Electrochemical Society*, vol. 148, no. 8, pp. A905–A909, 2001.

[60] S.-H. Kwak, T.-H. Yang, C.-S. Kim, and K. H. Yoon, "Nafion/mordenite hybrid membrane for high-temperature operation of polymer electrolyte membrane fuel cell," *Solid State Ionics*, vol. 160, no. 3, pp. 309–315, 2003.

[61] S. Malhotra and R. Datta, "Membrane-supported nonvolatile acidic electrolytes allow higher temperature operation of proton-exchange membrane fuel cells," *Journal of The Electrochemical Society*, vol. 144, no. 2, pp. L23–L26, 1997.

[62] S. Tan and D. Belanger, "Characterization and transport properties of nafion/polyaniline composite membranes," *The Journal of Physical Chemistry B*, vol. 109, no. 49, pp. 23480–23490, 2005.

[63] W. Lu, A. G. Fadeev, B. Qi, E. Smela, B. R. Mattes, J. Ding, G. M. Spinks, J. Mazurkiewicz, D. Zhou, G. G. Wallace, *et al.*, "Use of ionic liquids for π-conjugated polymer electrochemical devices," *Science*, vol. 297, no. 5583, pp. 983–987, 2002.

[64] M. D. Bennett, D. J. Leo, G. L. Wilkes, F. L. Beyer, and T. W. Pechar, "A model of charge transport and electromechanical transduction in ionic liquid-swollen nafion membranes," *Polymer*, vol. 47, no. 19, pp. 6782–6796, 2006.

[65] S. Liu, W. Liu, Y. Liu, J.-H. Lin, X. Zhou, M. J. Janik, R. H. Colby, and Q. Zhang, "Influence of imidazolium-based ionic liquids on the performance of ionic polymer conductor network composite actuators," *Polymer International*, vol. 59, no. 3, pp. 321–328, 2010.

[66] P. De Gennes, K. Okumura, M. Shahinpoor, and K. J. Kim, "Mechanoelectric effects in ionic gels," *EPL (Europhysics Letters)*, vol. 50, no. 4, p. 513, 2000.

[67] K. M. Newbury and D. J. Leo, "Linear electromechanical model of ionic polymer transducers-part i: model development," *Journal of Intelligent Material Systems and Structures*, vol. 14, no. 6, pp. 333–342, 2003.

[68] K. M. Newbury and D. J. Leo, "Linear electromechanical model of ionic polymer transducers-part ii: experimental validation," *Journal of Intelligent Material Systems and Structures*, vol. 14, no. 6, pp. 343–357, 2003.

[69] S. Nemat-Nasser, "Micromechanics of actuation of ionic polymer-metal composites," *Journal of Applied Physics*, vol. 92, no. 5, pp. 2899–2915, 2002.

[70] S. Nemat-Nasser and J. Y. Li, "Electromechanical response of ionic polymer-metal composites," *Journal of Applied Physics*, vol. 87, no. 7, pp. 3321–3331, 2000.

[71] B. J. Akle, K. B. Wiles, D. J. Leo, and J. E. McGrath, "Effects of electrode morphology on the performance of bpsh and pats ionic polymer transducers," in *Smart Structures and Materials*, pp. 413–424, International Society for Optics and Photonics, 2004.

[72] M. D. Bennett and D. J. Leo, "Hybrid actuation in coupled ionic/conducting polymer devices," in *MRS Proceedings*, vol. 785, pp. D8–2, Cambridge Univ Press, 2003.

[73] P. Millet, F. Andolfatto, and R. Durand, "Preparation of solid polymer electrolyte composites: investigation of the ion-exchange process," *Journal of Applied Electrochemistry*, vol. 25, no. 3, pp. 227–232, 1995.

[74] P. Millet, F. Andolfatto, and R. Durand, "Preparation of solid polymer electrolyte composites: investigation of the precipitation process," *Journal of applied electrochemistry*, vol. 25, no. 3, pp. 233–239, 1995.

[75] T. Rashid and M. Shahinpoor, "Force optimization of ionic polymeric platinum composite artificial muscles by means of an orthogonal array manufacturing method," in *1999 Symposium on Smart Structures and Materials*, pp. 289–298, International Society for Optics and Photonics, 1999.

[76] B. J. Akle and D. J. Leo, "Single-walled carbon nanotubesionic polymer electroactive hybrid transducers," *Journal of Intelligent Material Systems and Structures*, vol. 19, no. 8, pp. 905–915, 2008.

[77] G. Decher and J.-D. Hong, "Buildup of ultrathin multilayer films by a self-assembly process, 1 consecutive adsorption of anionic and cationic bipolar amphiphiles on charged surfaces," in *Makromolekulare Chemie. Macromolecular Symposia*, vol. 46, pp. 321–327, Wiley Online Library, 1991.

[78] G. Decher and J. Hong, "Buildup of ultrathin multilayer films by a self-assembly process: Ii. consecutive adsorption of anionic and cationic bipolar amphiphiles and polyelectrolytes on charged surfaces," *Berichte der Bunsengesellschaft für physikalische Chemie*, vol. 95, no. 11, pp. 1430–1434, 1991.

[79] G. Decher, J. Hong, and J. Schmitt, "Buildup of ultrathin multilayer films by a self-assembly process: Iii. consecutively alternating adsorption of anionic and cationic polyelectrolytes on charged surfaces," *Thin solid films*, vol. 210, pp. 831–835, 1992.

[80] F. Van Ackern, L. Krasemann, and B. Tieke, "Ultrathin membranes for gas separation and pervaporation prepared upon electrostatic self-assembly of polyelectrolytes," *Thin Solid Films*, vol. 327, pp. 762–766, 1998.

[81] J.-M. Leväsalmi and T. J. McCarthy, "Poly (4-methyl-1-pentene)-supported polyelectrolyte multilayer films: Preparation and gas permeability 1," *Macromolecules*, vol. 30, no. 6, pp. 1752–1757, 1997.

[82] T. R. Farhat and J. B. Schlenoff, "Ion transport and equilibria in polyelectrolyte multilayers," *Langmuir*, vol. 17, no. 4, pp. 1184–1192, 2001.

[83] X. Liu and M. L. Bruening, "Size-selective transport of uncharged solutes through multilayer polyelectrolyte membranes," *Chemistry of materials*, vol. 16, no. 2, pp. 351–357, 2004.

[84] J. J. Harris, J. L. Stair, and M. L. Bruening, "Layered polyelectrolyte films as selective, ultrathin barriers for anion transport," *Chemistry of materials*, vol. 12, no. 7, pp. 1941–1946, 2000.

[85] J. Lukáš, H.-H. Schwarz, and K. Richau, "Polyelectrolyte complex membranes–surface and permeability properties," in *Macromolecular Symposia*, vol. 188, pp. 155–165, Wiley Online Library, 2002.

[86] D. DeLongchamp and P. T. Hammond, "Layer-by-layer assembly of pedot/polyaniline electrochromic devices," *Advanced Materials*, vol. 13, no. 19, pp. 1455–1459, 2001.

[87] D. M. DeLongchamp and P. T. Hammond, "High-contrast electrochromism and controllable dissolution of assembled prussian blue/polymer nanocomposites," *Advanced Functional Materials*, vol. 14, no. 3, pp. 224–232, 2004.

[88] D. M. DeLongchamp and P. T. Hammond, "Multiple-color electrochromism from layer-by-layer-assembled polyaniline/prussian blue nanocomposite thin films," *Chemistry of Materials*, vol. 16, no. 23, pp. 4799–4805, 2004.

[89] R. Montazami, V. Jain, and J. R. Heflin, "High contrast asymmetric solid state electrochromic devices based on layer-by-layer deposition of polyaniline and poly (aniline sulfonic acid)," *Electrochimica Acta*, vol. 56, no. 2, pp. 990–994, 2010.

[90] A. A. Mamedov, N. A. Kotov, M. Prato, D. M. Guldi, J. P. Wicksted, and A. Hirsch, "Molecular design of strong single-wall carbon nanotube/polyelectrolyte multilayer composites," *Nature materials*, vol. 1, no. 3, pp. 190–194, 2002.

[91] J. H. Rouse and P. T. Lillehei, "Electrostatic assembly of polymer/single walled carbon nanotube multilayer films," *Nano Letters*, vol. 3, no. 1, pp. 59–62, 2003.

[92] A. P. Johnston, C. Cortez, A. S. Angelatos, and F. Caruso, "Layer-by-layer engineered capsules and their applications," *Current Opinion in Colloid & Interface Science*, vol. 11, no. 4, pp. 203–209, 2006.

[93] A. L. Becker, A. P. Johnston, and F. Caruso, "Layer-by-layer-assembled capsules and films for therapeutic delivery," *Small*, vol. 6, no. 17, 2010.

[94] C. Meis, R. Montazami, and N. Hashemi, "Ionic electroactive polymer actuators as active microfluidic mixers," *Analytical Methods*, vol. 7, no. 24, pp. 10217–10223, 2015.

[95] L. T. Wagner, J. Yang, S. Ghobadian, R. Montazami, and N. Hashemi, "A microfluidic reactor for energy applications," 2012.

[96] K. Schmidt-Rohr and Q. Chen, "Parallel cylindrical water nanochannels in nafion fuel-cell membranes," *Nature materials*, vol. 7, no. 1, pp. 75–83, 2008.

[97] K. Adjemian, S. Lee, S. Srinivasan, J. Benziger, and A. Bocarsly, "Silicon oxide nafion composite membranes for proton-exchange membrane fuel cell operation at 80-140 c," *Journal of the Electrochemical Society*, vol. 149, no. 3, pp. A256–A261, 2002.

[98] D. Spry, A. Goun, K. Glusac, D. E. Moilanen, and M. Fayer, "Proton transport and the water environment in nafion fuel cell membranes and aot reverse micelles," *Journal of the American Chemical Society*, vol. 129, no. 26, pp. 8122–8130, 2007.

[99] C. Jo, D. Pugal, I.-K. Oh, K. J. Kim, and K. Asaka, "Recent advances in ionic polymer–metal composite actuators and their modeling and applications," *Progress in Polymer Science*, vol. 38, no. 7, pp. 1037–1066, 2013.

[100] S. Y. Jung, S. Y. Ko, J.-O. Park, and S. Park, "Enhanced ionic polymer metal composite actuator with porous nafion membrane using zinc oxide particulate leaching method," *Smart Materials and Structures*, vol. 24, no. 3, p. 037007, 2015.

[101] K. Surana, P. K. Singh, B. Bhattacharya, C. Verma, and R. Mehra, "Synthesis of graphene oxide coated nafion membrane for actuator application," *Ceramics International*, vol. 41, no. 3, pp. 5093–5099, 2015.

[102] R. Zhang, Y. Chen, and R. Montazami, "Ionic liquid-doped gel polymer electrolyte for flexible lithium-ion polymer batteries," *Materials*, vol. 8, no. 5, pp. 2735–2748, 2015.

[103] I. Bauer, S. Thieme, J. Brückner, H. Althues, and S. Kaskel, "Reduced polysulfide shuttle in lithium–sulfur batteries using nafion-based separators," *Journal of Power Sources*, vol. 251, pp. 417–422, 2014.

[104] X. Yu, J. Joseph, and A. Manthiram, "Polymer lithium–sulfur batteries with a nafion membrane and an advanced sulfur electrode," *Journal of Materials Chemistry A*, vol. 3, no. 30, pp. 15683–15691, 2015.

[105] B. Jiang, L. Wu, L. Yu, X. Qiu, and J. Xi, "A comparative study of nafion series membranes for vanadium redox flow batteries," *Journal of Membrane Science*, vol. 510, pp. 18–26, 2016.

[106] C. K. Landrock and B. Kaminska, "New capacative storage device," in *PowerMEMS 2009 Conference Proceedings*, pp. 360–363, 2009.

[107] B. Paola, L. Fortuna, P. Giannone, S. Graziani, and S. Strazzeri, "Ipmcs as vibration sensors," in *Instrumentation and Measurement Technology Conference Proceedings, 2008. IMTC 2008. IEEE*, pp. 2065–2069, IEEE, 2008.

[108] H. Lei, M. A. Sharif, and X. Tan, "Dynamics of omnidirectional ipmc sensor: Experimental characterization and physical modeling," *IEEE/ASME Transactions on Mechatronics*, vol. 21, no. 2, pp. 601–612, 2016.

[109] L. Ferrara, M. Shahinpoor, K. J. Kim, H. B. Schreyer, A. Keshavarzi, E. Benzel, and J. W. Lantz, "Use of ionic polymer-metal composites (ipmcs) as a pressure transducer in the human spine," in *1999 Symposium on Smart Structures and Materials*, pp. 394–401, International Society for Optics and Photonics, 1999.

[110] Z. Chen, X. Tan, A. Will, and C. Ziel, "A dynamic model for ionic polymer–metal composite sensors," *Smart Materials and Structures*, vol. 16, no. 4, p. 1477, 2007.

[111] K. J. Kim and M. Shahinpoor, "A novel method of manufacturing three-dimensional ionic polymer–metal composites (ipmcs) biomimetic sensors, actuators and artificial muscles," *Polymer*, vol. 43, no. 3, pp. 797–802, 2002.

[112] A. Keshavarzi, M. Shahinpoor, K. J. Kim, and J. W. Lantz, "Blood pressure, pulse rate, and rhythm measurement using ionic polymer-metal composite sensors," in *1999 Symposium on Smart Structures and Materials*, pp. 369–376, International Society for Optics and Photonics, 1999.

[113] M. Shahinpoor, Y. Bar-Cohen, J. Simpson, and J. Smith, "Ionic polymer-metal composites (ipmcs) as biomimetic sensors, actuators and artificial muscles-a review," *Smart materials and structures*, vol. 7, no. 6, p. R15, 1998.

[114] I. Must, U. Johanson, F. Kaasik, I. Põldsalu, A. Punning, and A. Aabloo, "Charging a supercapacitor-like laminate with ambient moisture: from a humidity sensor to an energy harvester," *Physical Chemistry Chemical Physics*, vol. 15, no. 24, pp. 9605–9614, 2013.

[115] I. Must, V. Vunder, F. Kaasik, I. Põldsalu, U. Johanson, A. Punning, and A. Aabloo, "Ionic liquid-based actuators working in air: The effect of ambient humidity," *Sensors and Actuators B: Chemical*, vol. 202, pp. 114–122, 2014.

[116] X. Hu, W. Cheng, T. Wang, Y. Wang, E. Wang, and S. Dong, "Fabrication, characterization, and application in sers of self-assembled polyelectrolyte-gold nanorod multilayered films," *The Journal of Physical Chemistry B*, vol. 109, no. 41, pp. 19385–19389, 2005.

[117] Y. Lvov, G. Decher, and H. Moehwald, "Assembly, structural characterization, and thermal behavior of layer-by-layer deposited ultrathin films of poly (vinyl sulfate) and poly (allylamine)," *Langmuir*, vol. 9, no. 2, pp. 481–486, 1993.

[118] S. L. Clark, M. F. Montague, and P. T. Hammond, "Ionic effects of sodium chloride on the templated deposition of polyelectrolytes using layer-by-layer ionic assembly," *Macromolecules*, vol. 30, no. 23, pp. 7237–7244, 1997.

[119] S. T. Dubas and J. B. Schlenoff, "Factors controlling the growth of polyelectrolyte multilayers," *Macromolecules*, vol. 32, no. 24, pp. 8153–8160, 1999.

[120] W. Chen and T. J. McCarthy, "Layer-by-layer deposition: a tool for polymer surface modification," *Macromolecules*, vol. 30, no. 1, pp. 78–86, 1997.

[121] S. Ghannoum, Y. Xin, J. Jaber, and L. I. Halaoui, "Self-assembly of polyacrylate-capped platinum nanoparticles on a polyelectrolyte surface: Kinetics of adsorption and effect of ionic strength and deposition protocol," *Langmuir*, vol. 19, no. 11, pp. 4804–4811, 2003.

[122] A. McDaid, S. Xie, and K. Aw, "A compliant surgical robotic instrument with integrated ipmc sensing and actuation," *International Journal of Smart and Nano Materials*, vol. 3, no. 3, pp. 188–203, 2012.

[123] M. Shahinpoor, K. J. Kim, and D. J. Leo, "Ionic polymer-metal composites as multifunctional materials," *Polymer Composites*, vol. 24, no. 1, pp. 24–33, 2003.

[124] K. Oguro, Y. Kawami, and H. Takenaka, "Bending of an ion-conducting polymer film-electrode composite by an electric stimulus at low voltage," *Journal of Micromachine Society*, vol. 5, no. 1, pp. 27–30, 1992.

[125] J. Hou, Z. Zhang, and L. A. Madsen, "Cation/anion associations in ionic liquids modulated by hydration and ionic medium," *The Journal of Physical Chemistry B*, vol. 115, no. 16, pp. 4576–4582, 2011.

[126] J. Hou, J. Li, D. Mountz, M. Hull, and L. A. Madsen, "Correlating morphology, proton conductivity, and water transport in polyelectrolyte-fluoropolymer blend membranes," *Journal of Membrane Science*, vol. 448, pp. 292–299, 2013.

[127] H. Acar, S. Çınar, M. Thunga, M. R. Kessler, N. Hashemi, and R. Montazami, "Study of physically transient insulating materials as a potential platform for transient electronics and bioelectronics," *Advanced Functional Materials*, vol. 24, no. 26, pp. 4135–4143, 2014.

[128] J. Lyklema, *Fundamentals of interface and colloid science: soft colloids*, vol. 5. Academic press, 2005.

[129] J. E. B. Randles, "Kinetics of rapid electrode reactions," *Discussions of the faraday society*, vol. 1, pp. 11–19, 1947.

[130] P. Delahay and D. Turner, "New instrumental methods in electrochemistry," *Journal of The Electrochemical Society*, vol. 102, no. 2, pp. 46C–47C, 1955.

[131] A. J. Bard, L. R. Faulkner, J. Leddy, and C. G. Zoski, *Electrochemical methods: fundamentals and applications*, vol. 2. Wiley New York, 1980.

[132] K.-S. Kwon and T. N. Ng, "Improving electroactive polymer actuator by tuning ionic liquid concentration," *Organic Electronics*, vol. 15, no. 1, pp. 294–298, 2014.

[133] A. Della Santa, D. De Rossi, and A. Mazzoldi, "Characterization and modelling of a conducting polymer muscle-like linear actuator," *Smart Materials and Structures*, vol. 6, no. 1, p. 23, 1997.

[134] T. Wallmersperger, B. J. Akle, D. J. Leo, and B. Kröplin, "Electrochemical response in ionic polymer transducers: an experimental and theoretical study," *Composites Science and Technology*, vol. 68, no. 5, pp. 1173–1180, 2008.

[135] P. Wang, B. Lassen, R. Jones, and B. Thomsen, "Multiscale modelling of a composite electroactive polymer structure," *Smart Materials and Structures*, vol. 19, no. 12, p. 124008, 2010.

[136] B. J. Akle, D. Leo, M. Hickner, and J. E. McGrath, "Correlation of capacitance and actuation in ionomeric polymer transducers," *Journal of Materials Science*, vol. 40, no. 14, pp. 3715–3724, 2005.

[137] G. Alici, G. M. Spinks, J. D. Madden, Y. Wu, and G. G. Wallace, "Response characterization of electroactive polymers as mechanical sensors," *Mechatronics, IEEE/ASME Transactions on*, vol. 13, no. 2, pp. 187–196, 2008.

[138] K. D. Kreuer, M. Schuster, B. Obliers, O. Diat, U. Traub, A. Fuchs, U. Klock, S. J. Paddison, and J. Maier, "Short-side-chain proton conducting perfluorosulfonic acid ionomers: Why they perform better in pem fuel cells," *Journal of Power Sources*, vol. 178, no. 2, pp. 499–509, 2008.

[139] F. Croce, M. L. Focarete, J. Hassoun, I. Meschini, and B. Scrosati, "A safe, high-rate and high-energy polymer lithium-ion battery based on gelled membranes prepared by electrospinning," *Energy & Environmental Science*, vol. 4, no. 3, pp. 921–927, 2011.

[140] A. Jablonski, P. J. Kulesza, and A. Lewera, "Oxygen permeation through nafion 117 membrane and its impact on efficiency of polymer membrane ethanol fuel cell," *Journal of Power Sources*, vol. 196, no. 10, pp. 4714–4718, 2011.

[141] J. Yang, S. Ghobadian, P. J. Goodrich, R. Montazami, and N. Hashemi, "Miniaturized biological and electrochemical fuel cells: challenges and applications," *Physical Chemistry Chemical Physics*, vol. 15, no. 34, pp. 14147–14161, 2013.

[142] T. Sugino, K. Kiyohara, I. Takeuchi, K. Mukai, and K. Asaka, "Actuator properties of the complexes composed by carbon nanotube and ionic liquid: the effects of additives," *Sensors and Actuators B: Chemical*, vol. 141, no. 1, pp. 179–186, 2009.

[143] Y. H. Zhao, M. H. Abraham, and A. M. Zissimos, "Fast calculation of van der waals volume as a sum of atomic and bond contributions and its application to drug compounds," *The Journal of organic chemistry*, vol. 68, no. 19, pp. 7368–7373, 2003.

[144] M. Raibert, K. Blankespoor, G. Nelson, R. Playter, and T. Team, "Bigdog, the rough-terrain quadruped robot," in *Proceedings of the 17th World Congress*, vol. 17, pp. 10822–10825, Proceedings Seoul, Korea, 2008.

[145] K. Asaka and H. Okuzaki, *Soft Actuators: Materials, Modeling, Applications, and Future Perspectives*. Springer, 2014.

[146] M. Shahinpoor, "Biomimetic robotic venus flytrap (dionaea muscipula ellis) made with ionic polymer metal composites," *Bioinspiration & biomimetics*, vol. 6, no. 4, p. 046004, 2011.

[147] K. Kim, "Ionic polymer-metal composite as a new actuator and transducer material," in *Electroactive Polymers for Robotic Applications*, pp. 153–164, Springer, 2007.

[148] S. Lee, H. Park, S. D. Pandita, and Y. Yoo, "Performance improvement of ipmc (ionic polymer metal composites) for a flapping actuator," *International Journal of Control Automation and Systems*, vol. 4, no. 6, p. 748, 2006.

[149] Y. Bar-Cohen, "Artificial muscles using electroactive polymers (eap): Capabilities, challenges and potential," 2005.

[150] Z. Chen, S. Shatara, and X. Tan, "Modeling of biomimetic robotic fish propelled by an ionic polymer–metal composite caudal fin," *Mechatronics, IEEE/ASME Transactions on*, vol. 15, no. 3, pp. 448–459, 2010.

[151] X. Tan, D. Kim, N. Usher, D. Laboy, J. Jackson, A. Kapetanovic, J. Rapai, B. Sabadus, and X. Zhou, "An autonomous robotic fish for mobile sensing," in *2006 IEEE/RSJ International Conference on Intelligent Robots and Systems*, pp. 5424–5429, IEEE, 2006.

[152] R. Lumia and M. Shahinpoor, "Ipmc microgripper research and development," in *Journal of Physics: Conference Series*, vol. 127, p. 012002, IOP Publishing, 2008.

[153] R. Jain, U. Patkar, and S. Majumdar, "Micro gripper for micromanipulation using ipmcs (ionic polymer metal composites)," *Journal of Scientific and Industrial Research*, vol. 68, no. 1, p. 23, 2009.

[154] D. Chatterjee, N. Hanumaiah, Y. Bahramzadeh, and M. Shahinpoor, "Actuation and sensing studies of a miniaturized five fingered robotic hand made with ion polymeric metal composite (ipmc)," in *Advanced Materials Research*, vol. 740, pp. 492–495, Trans Tech Publ, 2013.

[155] Y. Nakabo, T. Mukai, and K. Asaka, "Biomimetic soft robots with artificial muscles," in *Smart Materials, Nano-, and Micro-Smart Systems*, pp. 132–144, International Society for Optics and Photonics, 2004.

[156] Y. Nakabo, T. Mukai, and K. Asaka, "Kinematic modeling and visual sensing of multi-dof robot manipulator with patterned artificial muscle," in *Proceedings of the 2005 IEEE International Conference on Robotics and Automation*, pp. 4315–4320, IEEE, 2005.

[157] N. Kamamichi, M. Yamakita, K. Asaka, and Z.-W. Luo, "A snake-like swimming robot using ipmc actuator/sensor," in *Proceedings 2006 IEEE International Conference on Robotics and Automation, 2006. ICRA 2006.*, pp. 1812–1817, IEEE, 2006.

[158] G. Di Pasquale, L. Fortuna, S. Graziani, M. La Rosa, A. Pollicino, and E. Umana, "A study on ip2c actuators using ethylene glycol or emi-tf as solvent," *Smart Materials and Structures*, vol. 20, no. 4, p. 045014, 2011.

[159] X. Crispin, F. Jakobsson, A. Crispin, P. Grim, P. Andersson, A. Volodin, C. Van Haesendonck, M. Van der Auweraer, W. R. Salaneck, and M. Berggren, "The origin of the high conductivity of poly (3, 4-ethylenedioxythiophene)-poly (styrenesulfonate)(pedot-pss) plastic electrodes," *Chemistry of Materials*, vol. 18, no. 18, pp. 4354–4360, 2006.

[160] G. Di Pasquale, S. Graziani, and E. Umana, "From ipmc transducers to all-organic transducers," in *Sensors*, pp. 251–254, Springer, 2014.

[161] H. Okuzaki, S. Takagi, F. Hishiki, and R. Tanigawa, "Ionic liquid/polyurethane/pedot: Pss composites for electro-active polymer actuators," *Sensors and Actuators B: Chemical*, vol. 194, pp. 59–63, 2014.

[162] S. Graziani, E. Umana, M. Xibilia, and V. De Luca, "Multi-input identification of ip2c actuators," in *2013 IEEE International Instrumentation and Measurement Technology Conference (I2MTC)*, pp. 1147–1151, IEEE, 2013.

[163] S. Graziani, E. Umana, and M. Xibilia, "Identification and modeling of polymeric actuators: a comparison," in *Control & Automation (MED), 2012 20th Mediterranean Conference on*, pp. 216–221, IEEE, 2012.

[164] L. Fortuna, S. Graziani, M. La Rosa, D. Nicolosi, G. Sicurella, and E. Umana, "Modelling and design of all-organic electromechanic transducers," *The European Physical Journal Applied Physics*, vol. 46, no. 1, p. 12513, 2009.

[165] L. Cavallini and P. Di Giamberardino, "Validation of ip 2 c devices as touch sensors," in *Control & Automation (MED), 2012 20th Mediterranean Conference on*, pp. 48–53, IEEE, 2012.

[166] S. Graziani, E. Umana, G. Di Pasquale, M. La Rosa, and G. Sicurella, "Ip 2 c sensor modeling," in *Instrumentation and Measurement Technology Conference (I2MTC), 2012 IEEE International*, pp. 1299–1302, IEEE, 2012.

[167] C. Zhang, C. Lai, G. Zeng, D. Huang, L. Tang, C. Yang, Y. Zhou, L. Qin, and M. Cheng, "Nanoporous au-based chronocoulometric aptasensor for amplified detection of pb 2+ using dnazyme modified with au nanoparticles," *Biosensors and Bioelectronics*, vol. 81, pp. 61–67, 2016.

[168] M. Sima, M. N. Grecu, and I. Enculescu, "Growth and characterization of zno: Mn submicron wires via electrodeposition from nitrate-lactic acid solution," *ECS Transactions*, vol. 25, no. 27, pp. 163–171, 2010.

[169] A. Simaite, B. Tondu, F. Mathieu, P. Souéres, and C. Bergaud, "Simple casting based fabrication of pedot: Pss-pvdf-ionic liquid soft actuators," in *SPIE Smart Structures and Materials+ Nondestructive Evaluation and Health Monitoring*, pp. 94301E–94301E, International Society for Optics and Photonics, 2015.

[170] J. T. Edward, "Molecular volumes and the stokes-einstein equation," *J. chem. Educ*, vol. 47, no. 4, p. 261, 1970.

[171] Y. Bar-Cohen, "Electroactive polymers as artificial muscles-capabilities, potentials and challenges," *Handbook on biomimetics*, vol. 8, 2000.

[172] A. A. A. Moghadam, M. Moavenian, K. Torabi, and M. Tahani, "Analytical dynamic modeling of fast trilayer polypyrrole bending actuators," *Smart Materials and Structures*, vol. 20, no. 11, p. 115020, 2011.

[173] E. Smela, "Conjugated polymer actuators for biomedical applications," *Advanced materials*, vol. 15, no. 6, pp. 481–494, 2003.

[174] T. F. Otero and M. T. Cortes, "Characterization of triple layers," in *SPIE's 8th Annual International Symposium on Smart Structures and Materials*, pp. 93–100, International Society for Optics and Photonics, 2001.

[175] G. G. Wallace, P. R. Teasdale, G. M. Spinks, and L. A. Kane-Maguire, *Conductive electroactive polymers: intelligent polymer systems*. CRC press, 2008.

[176] J. D. Madden, N. A. Vandesteeg, P. A. Anquetil, P. G. Madden, A. Takshi, R. Z. Pytel, S. R. Lafontaine, P. A. Wieringa, and I. W. Hunter, "Artificial muscle technology: physical principles and naval prospects," *Oceanic Engineering, IEEE Journal of*, vol. 29, no. 3, pp. 706–728, 2004.

[177] K. Onishi, S. Sewa, K. Asaka, N. Fujiwara, and K. Oguro, "Morphology of electrodes and bending response of the polymer electrolyte actuator," *Electrochimica Acta*, vol. 46, no. 5, pp. 737–743, 2001.

[178] M. Shahinpoor, "Micro-electro-mechanics of ionic polymeric gels as electrically controllable artificial muscles," *Journal of Intelligent Material Systems and Structures*, vol. 6, no. 3, pp. 307–314, 1995.

[179] R. K. Jain, S. Majumder, and A. Dutta, "Scara based peg-in-hole assembly using compliant ipmc micro gripper," *Robotics and Autonomous Systems*, vol. 61, no. 3, pp. 297–311, 2013.

[180] A. A. Amiri Moghadam, M. Moavenian, and H. E. Toussi, "Modelling and robust control of a soft robot based on conjugated polymer actuators," *International Journal of Modelling, Identification and Control*, vol. 14, no. 3, pp. 216–226, 2011.

[181] A. A. A. Moghadam, K. Torabi, M. Moavenian, and R. Davoodi, "Dynamic modeling and robust control of an l-shaped microrobot based on fast trilayer polypyrrole-bending actuators," *Journal of Intelligent Material Systems and Structures*, vol. 24, no. 4, pp. 484–498, 2013.

[182] A.-A. Amiri-M, M. Moavenian, and K. Torabiz, "Takagi-sugeno fuzzy modelling and parallel distributed compensation control of conducting polymer actuators," *Proceedings of the Institution of Mechanical Engineers, Part I: Journal of Systems and Control Engineering*, vol. 224, no. 1, pp. 41–51, 2010.

[183] K. Torabi and A. A. A. Moghadam, "Robust control of conjugated polymer actuators considering the spatio-temporal dynamics," *Proceedings of the Institution of Mechanical Engineers, Part I: Journal of Systems and Control Engineering*, vol. 226, no. 6, pp. 806–822, 2012.

[184] Z. Chen and X. Tan, "A control-oriented and physics-based model for ionic polymer–metal composite actuators," *Mechatronics, IEEE/ASME Transactions on*, vol. 13, no. 5, pp. 519–529, 2008.

[185] H. Moeinkhah, J. Rezaeepazhand, and A. Akbarzadeh, "Analytical dynamic modeling of a cantilever ipmc actuator based on a distributed electrical circuit," *Smart Materials and Structures*, vol. 22, no. 5, p. 055033, 2013.

[186] R. Kanno, S. Tadokoro, T. Takamori, M. Hattori, and K. Oguro, "Linear approximate dynamic model of icpf (ionic conducting polymer gel film) actuator," in *Robotics and*

Automation, 1996. Proceedings., 1996 IEEE International Conference on, vol. 1, pp. 219–225, IEEE, 1996.

[187] M. Vahabi, E. Mehdizadeh, M. Kabganian, and F. Barazandeh, "Experimental identification of ipmc actuator parameters through incorporation of linear and nonlinear least squares methods," *Sensors and Actuators A: Physical*, vol. 168, no. 1, pp. 140–148, 2011.

[188] X. Bao, Y. Bar-Cohen, and S.-S. Lih, "Measurements and macro models of ionomeric polymer-metal composites (ipmc)," in *SPIE's 9th Annual International Symposium on Smart Structures and Materials*, pp. 220–227, International Society for Optics and Photonics, 2002.

[189] A. Punning, U. Johanson, M. Anton, A. Aabloo, and M. Kruusmaa, "A distributed model of ionomeric polymer metal composite," *Journal of Intelligent Material Systems and Structures*, vol. 20, no. 14, pp. 1711–1724, 2009.

[190] K. M. Farinholt, *Modeling and characterization of ionic polymer transducers for sensing and actuation*. PhD thesis, Virginia Polytechnic Institute and State University, 2005.

[191] W. Yim, M. B. Trabia, J. M. Renno, J. Lee, and K. J. Kim, "Dynamic modeling of segmented ionic polymer metal composite (ipmc) actuator," in *Intelligent Robots and Systems, 2006 IEEE/RSJ International Conference on*, pp. 5459–5464, IEEE, 2006.

[192] S. Gutta, J. S. Lee, M. B. Trabia, and W. Yim, "Modeling of ionic polymer metal composite actuator dynamics using a large deflection beam model," *Smart Materials and Structures*, vol. 18, no. 11, p. 115023, 2009.

[193] E. Wittbrodt, I. Adamiec-Wójcik, and S. Wojciech, *Dynamics of flexible multibody systems: rigid finite element method*. Springer Science & Business Media, 2007.

[194] N. Collins, R. Eglese, and B. Golden, "Simulated annealing–an annotated bibliography," *American Journal of Mathematical and Management Sciences*, vol. 8, no. 3-4, pp. 209–307, 1988.

[195] E. Aarts and J. Korst, "Simulated annealing and boltzmann machines," 1988.

[196] S. G. Kelly, *Advanced vibration analysis*. CRC Press, 2006.

[197] H.-C. Wei and G.-D. J. Su, "Design and fabrication of a large-stroke deformable mirror using a gear-shape ionic-conductive polymer metal composite," *Sensors*, vol. 12, no. 8, pp. 11100–11112, 2012.

[198] J. Y. Li and S. Nemat-Nasser, "Micromechanical analysis of ionic clustering in nafion perfluorinated membrane," *Mechanics of materials*, vol. 32, no. 5, pp. 303–314, 2000.

[199] F. Greco, A. Zucca, S. Taccola, A. Menciassi, T. Fujie, H. Haniuda, S. Takeoka, P. Dario, and V. Mattoli, "Ultra-thin conductive free-standing pedot/pss nanofilms," *Soft Matter*, vol. 7, no. 22, pp. 10642–10650, 2011.

[200] http://www.engineeringtoolbox.com/metals-poissons-ratio-d_1268.html.